

SELECTIVE LASER MELTING OF POROSITY GRADED
GYROIDS FOR BONE IMPLANT APPLICATIONS

SELECTIVE LASER MELTING OF POROSITY GRADED GYROIDS FOR BONE
IMPLANT APPLICATIONS

By

DALIA MAHMOUD, BSc., MSc.

A Thesis

Submitted to the School of Graduate Studies in Partial Fulfillment of the Requirements
for the Degree Doctor of Philosophy

McMaster University

© Copyright by Dalia Mahmoud, July 2020

DOCTOR OF PHILOSOPHY (2019)

McMaster University

(Mechanical Engineering)

Hamilton, Ontario

TITLE: Selective Laser Melting of Porosity Graded Gyroids for
Bone Implant Applications

AUTHOR: Dalia Mahmoud
B.Sc. in Production Engineering (Alexandria University)
M.Sc. in Production Engineering (Alexandria University)

SUPERVISORS: Dr. M. A. Elbestawi

NUMBER OF PAGES: xxiv, 181

Lay Abstract

This thesis studies the integration of design aspects, SLM manufacturability, and mechanical characterization of Ti6Al4V gyroid lattice structures used for bone implants. A MATLAB® code was developed to design novel porosity graded gyroids, and develop permissible design map to aid the choice of different gyroid designs for bone implants.. Process maps were also developed to investigate the relationship among laser power, scan speed, and the errors in the relative density of lattice structures. Moreover, the normalized fatigue strength of thin struts gyroid was found to be higher than that of thicker struts. Analytical models and finite element analysis (FEA) models were compared to experimental results. The variation of the results gives a better understanding of the effect of manufacturing defects. An improved insight of gyroids manufacturability has been obtained by integrating the permissible design space with the process-structure-property relationship, and the defect analysis of porosity graded gyroids.

Abstract

The main aim of this thesis is to investigate the manufacturability of different gyroid designs using Selective laser melting (SLM) process . This study paves the way for a better understanding of design aspects, process optimization, and characterization of titanium alloy (Ti6Al4V) gyroid lattice structures for bone implant applications.

First, A MATLAB® code was developed to create various gyroid designs and understand the relationship between the implicit equation parameters and the measurable outputs of gyroid unit cells. A novel gyroid lattice structure is proposed, where the porosity is graded in a radial direction. Second, gyroid designs were investigated by developing a permissible design map to help choose the right gyroid parameters for bone implants.

Third, response surface methodology was used to study the process-structure-property relationship and understand the effect of SLM process parameters on the manufacturability of Ti6Al4V gyroid lattice structures. Laser power was found to be the most significant factor affecting the errors in relative density and strut size of gyroid structures. A volumetric energy density between 85 and 103 J/mm³ induces the least errors in the gyroid's relative density.

Fourth, the quasi-static properties of the novel designs were compared to uniform gyroids. The proposed novel gyroids had the highest compressive strength reaching 160 MPa. Numerical simulations were studied to give insight into how manufacturing irregularities can affect the mechanical properties of gyroids. Last, an in-depth defect analysis was conducted to understand how SLM defects may influence the fatigue properties of different Ti6Al4V gyroids. Thin struts have less internal defects than thick ones; thus, they show

less crack propagation rate and higher normalized fatigue life. These favorable findings contributed to scientific knowledge of manufacturability of Ti6Al4V porosity graded gyroids and determined the influence of SLM defects on the mechanical properties of gyroid designs for bone implants.

Preface

This thesis deals with the selective laser melting of gyroid lattice structures for bone implant applications. The thesis is composed of five journal articles, and the contributions are listed below:

Chapter 2: A version of this chapter is published as a review article “Dalia Mahmoud, and Mohamed A. Elbestawi. "Lattice structures and functionally graded materials applications in additive manufacturing of orthopedic implants: a review." *Journal of Manufacturing and Materials Processing* 1.2 (2017): 13.” Dalia Mahmoud wrote the first draft and Dr. Mohamed A. Elbestawi revised the manuscript.

Chapter 3: A version of this chapter is published as a research article “Dalia Mahmoud, and Mohamed. A. Elbestawi. "Selective laser melting of porosity graded lattice structures for bone implants." *The International Journal of Advanced Manufacturing Technology* 100.9-12 (2019): 2915-2927.” Dalia Mahmoud performed the experimental work, data collection, analysis, and wrote the first draft. Dr. Mohamed A. Elbestawi revised and edited the manuscript.

Chapter 4: A version of this chapter is accepted in the STP1631 on Fourth ASTM Symposium on Structural Integrity of Additive Manufactured Materials & Parts, “Dalia Mahmoud, Mohamed A. Elbestawi, and Kassim S. Al-Rubaie " Effect of Microstructure and Internal defects on the Mechanical Properties of Ti6Al4V Gyroid Lattice Structures for Biomedical Implants." Dalia Mahmoud performed the experimental work, data collection, analysis, and wrote the first draft. Dr. Kassim S. Al-Rubai revised the microstructure analysis in the experimental work. Dr. Mohamed A. Elbestawi revised and edited the manuscript.

Chapter 5: A version of this chapter is published as a research article “Dalia Mahmoud, M. A. Elbestawi, and Bosco Yu. "Process–Structure-Property Relationships in Selective Laser Melting of Porosity Graded Gyroids." *Journal of Medical Devices* 13.3 (2019).” Dalia Mahmoud performed the experimental work, data collection, analysis, and wrote the first draft. Dr. Bosco Yu revised the quasi-static analysis in the experimental work. Dr. Mohamed A. Elbestawi revised and edited the manuscript.

Chapter 6: A version of this chapter is submitted to the additive manufacturing journal, “The Influence of Selective Laser Melting Defects on the Fatigue Properties of Ti6Al4V Porosity Graded Gyroids for Bone Implants.” Dalia Mahmoud performed the experimental work, data collection, analysis, and wrote the first draft. Dr. Kassim S. Al-Rubai revised the microstructure and fatigue analysis in the experimental work. Dr. M Mohamed A. Elbestawi revised and edited the manuscript.

*To my parents,
I owe you everything*

Acknowledgments

First and foremost, I would like to express my deepest gratitude to my supervisor Dr. Elbestawi; I am thankful for his motivation, patience, and immense knowledge. His support and guidance from day one helped me to overcome the most challenging parts of this journey. Dr. Elbestawi has taught me how to tackle each problem scientifically and how to overcome the research challenges one at a time. I consider myself beyond lucky to have completed my thesis under his supervision and to have him as a mentor and teacher.

I would also like to extend my gratitude to my supervisory committee: Dr. Wohl and Dr. Fang, for their interesting discussions, insightful comments, and guidance. I wish to thank Dr. Al-Rubaie for all his effort and encouraging remarks during the last year. I am also very thankful for the help and assistance of McMaster's Department of Mechanical Engineering staff. I am also grateful for the support of the Natural Sciences and Engineering Research Council of Canada (NSERC).

I would like to show my appreciation to my colleagues in the AMG at McMaster University, for the ongoing discussions, presentation rehearsals, and fruitful group meetings. Special thanks to Mostafa, Mohamed, and Ramy for the coffee breaks and the continuous support throughout the last four years. I am thankful to my friends in Canada and Egypt for their warm reassurance and encouragement for the past four years, Somiraa, Noha, Heba, Shaza, Asmaa, Aliaa, and Dalia.

My heartfelt appreciation to my family in the USA and Egypt for their unconditional love, understanding, and warmth. I am indebted to my parents for their love and devotion throughout my life. I am grateful for my kids, Laila and Amr, for being the first and best motivation. Last but not least, my husband Sherif, none of this could have been possible without him.

Contents

	Page
Preface	vi
Abstract	iv
Acknowledgments	ix
Contents	x
List of Figures	xvi
List of Tables	xxi
List of Abbreviations	xxiii
Nomenclature	xxiv
1 Introduction	1
1.1 Background	1
1.2 Motivation.....	5
1.3 Rationale	5
1.4 Research objectives.....	6
1.5 Thesis outline	6
1.6 References.....	8

2	Lattice Structure and Functionally Graded Materials Applications in Additive Manufacturing of Orthopedic Implants: A review	11
1.1	Introduction.....	13
2.1	Lattice structures.....	16
2.1.1	Classification	16
2.1.2	Manufacturing	19
2.1.3	Characterization.....	22
2.1.4	Modelling and validation.....	26
2.2	FGM.....	30
2.2.1	Classification and manufacturing	30
2.2.2	Case Studies.....	32
2.3	Challenges and future directions.....	37
2.4	Conclusions.....	38
2.5	References.....	39
3	Selective Laser Melting of Porosity Graded Lattice Structures for Bone Implants	48
3.1	Introduction.....	51
3.2	Design of porosity graded lattice structures.....	54
3.3	Experimental work.....	57
3.3.1	Materials and methods.....	57
3.3.2	Scanning strategies	59
3.3.3	Volume fraction.....	60
3.3.4	Dimensional accuracy.....	60
3.3.5	Surface integrity	61

3.4	Results and discussion	61
3.4.1	Visual evaluation	61
3.4.2	Volume fraction.....	62
3.4.3	Dimensional accuracy.....	64
3.4.4	Surface integrity	69
3.5	Conclusion and future work.....	72
3.6	References.....	51
4	Effect of Microstructure and Internal defects on the Mechanical Properties of Ti6Al4V Gyroid Lattice Structures for Biomedical Implants	77
4.1	Introduction.....	80
4.2	Materials and methods	82
4.2.1	Design and 3d printing	82
4.2.2	Microstructure characterization.....	85
4.2.3	Morphology and internal defects characterization	85
4.2.4	Mechanical Testing.....	85
4.2.5	Finite element analysis	86
4.3	Results and discussion	87
4.3.1	Microstructure	87
4.3.2	Internal porosity.....	91
4.3.3	Mechanical properties.....	94
4.4	Conclusions.....	97
4.5	References.....	98

5	Process-structure-property relationships in selective laser melting of porosity graded gyroids.....	103
5.1	Introduction.....	106
5.2	Experimental procedure.....	108
5.2.1	Materials: Alloy powders	108
5.2.2	Lattice design.....	109
5.2.3	Selective laser melting.....	111
5.2.4	Characterization.....	112
5.2.4.1	Microstructure and morphology	112
5.2.4.2	Mechanical Properties	113
5.3	Results and discussion	113
5.3.1	Microstructure and microhardness	113
5.3.2	Morphology	115
5.3.2.1	Effect of energy density on part morphology.....	115
5.3.2.2	Laser Power, Scan Speed, porosity grading effect.....	117
5.3.3	Mechanical properties.....	119
5.3.3.1	The effect of VED on the mechanical properties	120
5.3.3.2	Failure Mode	124
5.4	Conclusion	126
5.5	References.....	127
6	The Influence of Selective Laser Melting Defects on the Fatigue Properties of Ti6Al4V Porosity Graded Gyroids for Bone Implants.....	131
6.1	Introduction.....	134
6.2	Materials and methods	137

6.2.1	Sample design.....	137
6.2.2	Powder characterization and SLM process parameters	139
6.3	Characterization	141
6.3.1	Morphology and microstructure	141
6.3.2	Quasi-static compression.....	142
6.3.3	Finite element analysis	143
6.3.4	Fatigue testing	144
6.4	Results and discussion	145
6.4.1	Morphology	145
6.4.1.1	Qualitative analysis	145
6.4.1.2	Quantitative analysis	147
6.4.2	Microstructure and microhardness	148
6.4.3	Quasi-static compression.....	150
6.4.3.1	Experimental results.....	150
6.4.3.2	Analytical solution	151
6.4.3.3	Finite Element Analysis	152
6.4.4	Fatigue testing	154
6.4.4.1	Strain accumulation.....	154
6.4.4.2	Cyclic stress-strain	156
6.4.4.3	S-N curves	158
6.4.4.4	Fracture surface.....	160
6.5	Conclusions.....	161
6.6	References.....	163
7	Summary and Conclusions	169

7.1	Summary and conclusive remarks	169
7.2	Strength and limitations	170
7.3	Future work.....	172
7.4	Contribution	173
Appendix A: Process-Structure property relationship ANOVA tables		174
A.1	Introduction.....	174
A.2	ANOVA test results for relative errors in $T_b T_h$ and ρ_m	175
A.2	ANOVA test results for relative errors in E_{app} and σ_p	176
Appendix B		177
B.1	Evaluation of fatigue life of uniform porous structures	177
B.2	Prediction of the fatigue life of G24.....	180
	References.....	181

List of Figures

Figure 1-1: Illustration of a typical SLM process.....	3
Figure 1-2: a) schematic diagram of cortical and trabecular bone and b) biomimetic porosity graded gyroid design.....	4
Figure 2-1: Different unit cells designs of lattice structures used in biomedical implants	18
Figure 2-2: Classification of FGM according to (a) composition, (b) microstructure, (c) porosity	31
Figure 3-1: Morphology of a single gyroid unit cell.....	54
Figure 3-2: (a) Volume fraction, (b) strut and pore size as a function of level constant (t) for gyroid unit cell	56
Figure 3-3: Permissibility design space for gyroid unit cell	51
Figure 3-4: Porosity graded gyroids (PGGs)	58
Figure 3-5: SLM scanning strategies used for printing the PGGs	59
Figure 3-6: Visual evaluation of PGGs.....	62
Figure 3-7: Total volume fraction obtained from different measurement methods compared to corresponding design values	64
Figure 3-8: Layer's volume fraction obtained via μ CT and compared to corresponding design values.....	64
Figure 3-9: Strut size obtained via μ CT and compared to corresponding design values..	66
Figure 3-10: Laser scanning strategies along different layers of PGG	67
Figure 3-11: Mesh comparison of μ CT reconstruction and the CAD model for last layer of the three PGGs, red and blue represents plus and minus errors. Histograms represents the occurrence of each value, dimensions in mm.	68

Figure 3-12: Mesh comparison of one row from the last layer obtained via μ CT and compared to the CAD model for the three PGGs, red and blue represents plus and minus errors. Histograms represents the occurrence of each value, dimensions in mm..... 69

Figure 3-13: Average surface roughness “Ra” values for each layer along the powder layer thickness..... 70

Figure 3-14: SEM images of the (a) first two layers and (b) last two layers of the PGGs. 72

Figure 4-1: (a) Gyroid part design and as-built parts using SLM process at different VED levels: (b) 43 J/mm³, (c) 103 J/mm³, and (d) 192 J/mm³. 84

Figure 4-2: Optical micrographs (100x) of the Ti6Al4V gyroids printed at three VED levels: (a), (d) at 43 J/mm³; (b), (e) at 103 J/mm³; and (c), (f) at 192 J/mm³. (a), (b), and (c) were taken along the build direction. (d), (e), and (f) were taken from the top side. Scale bars are equal to 100 μ m..... 87

Figure 4-3: SEM images (5000x) of the gyroid parts printed at different VED levels: (a) 43 J/mm³, (b) 103 J/mm³, and (c) 192 J/mm³. 88

Figure 4-4: XRD analysis for the Ti6Al4V gyroid parts printed at different VED. 89

Figure 4-5: Micro-CT slices taken from a constant height = 9.5 mm from base of the gyroid parts at different VED levels (a) design, (b) 43 J/mm³, (c) 103 J/mm³, and (d) 192 J/mm³. 90

Figure 4-6: Reconstructed gyroid unit cells at different VED levels: (a) 43 J/mm³, (b) 103 J/mm³, and (c) 192 J/mm³. 91

Figure 4-7: Pore frequency distribution along with the build directions of gyroid lattice structures printed at three VED levels: (a) 43 J/mm³, (b) 103 J/mm³, and (c) 192 J/mm³. 92

Figure 4-8: Internal pore size distribution for equivalent pore diameter in gyroid lattice structures printed at different VED levels: (a) 43 J/mm³, (b) 103 J/mm³, and (c) 192 J/mm³. 93

Figure 4-9: Aspect ratio for internal pores of the different gyroid lattice structures printed at different VED: (a) 43 J/mm³, (b) 103 J/mm³, and (c) 192 J/mm³. 94

Figure 4-10: Stress-strain diagram of the gyroid parts at different VED levels.	95
Figure 4-11: Experimental versus FEA stress-strain diagram for gyroid parts.....	97
Figure 5-1: SEM images showing the starting Ti6Al4V powder shape and morphology (a) 100 x magnification (b) at 50 x magnification.....	109
Figure 5-2: Linearly porosity graded gyroids (L-PGGs) samples.	110
Figure 5-3: Microstructural analysis (a) L-PGGs-3- VED = 42.735 J/mm ³ lack of fusion indicated by arrow, (b) L-PGGs 6- VED= 85.47 J/mm ³ , and (c) L-PGGs 7- VED=192.31 J/mm ³ internal porosities indicated by arrows , scale bar is 50 μm.	114
Figure 5-4: Microhardness results for L-PGGs printed with different VED.	115
Figure 5-5: SEM images of L-PGGs printed at different VED (a) STL file (b)L-PGGs-3- VED= 42.735 J/mm ³ (c) L-PGGs-6- VED= 85.47 J/mm ³ , (d) L-PGGs-7- VED =192.31 J/mm ³ , scale bar = 500 μm.....	116
Figure 5-6: Recommended VED for PGGs printed by SLM.....	117
Figure 5-7: Main effects plot for relative error in $T_b T_h$ and ρ_m	118
Figure 5-8: Process maps to identify the relative error in strut size and volume fraction.	119
Figure 5-9: Top view of radially PGGs designs.	120
Figure 5-10: Typical stress strain diagram for a 3D printed gyroid lattice.....	121
Figure 5-11: E_{app} and σ_p for graded and non-graded PGGs.....	122
Figure 5-12: Mechanical properties of different R-PGGs designs at same VED.	123
Figure 5-13: Main effect plot for E_{app} and σ_p at different factors.....	124
Figure 5-14: Process maps for E_{app} and σ_p of the three R-PGGs designs.....	124
Figure 5-15: Failure modes observed during uniaxial compression tests.....	125
Figure 6-1: a) Gyroid cylindrical sample and b) single unit cell of gyroid showing the unit cell size (L).	138

Figure 6-2. Top view of the proposed gyroid designs samples designed at 20% relative density a) G2 having 200 μm struts, b) G4, having 400 μm struts and c) G24 with graded struts in the radial direction (200 μm in the center and 400 μm at the borders).	139
Figure 6-3: Ti6Al4V powder: a) SEM morphology (scale bar=100 μm) and b) size distribution analysis	139
Figure 6-4. The laser scan path in thick struts (G4) versus thin struts (G2), showing the same process parameters used to print the gyroid parts.....	141
Figure 6-5: SEM side-view images (scale bar =200 μm) of the Ti6Al4V gyroid lattice structures: a) G2, b) G4, and c) G24 (borders).	146
Figure 6-6: Top view (Y-X) and along build direction view (Z-X) of scanned parts vs. designed gyroid lattice structures a) G2 b) G4 and c) G24.....	147
Figure 6-7: Microstructure (scale bar=100 μm) along the build direction of the Ti6AL4V gyroid lattice structures: a) G2, b) G4, and c) G24, and SEM images (scale bar=10 μm , 5000x): e) G2, f) G4 and c) G24.....	149
Figure 6-8: Microhardness results for the different designs of Ti6Al4V gyroid lattice structures.....	149
Figure 6-9: Stress-strain diagram for the different Ti6Al4V gyroid lattice structures....	151
Figure 6-10: Force distribution on a) a single layer, and b) single unit cell of the gyroid lattice structure.....	152
Figure 6-11: FEA simulation results on design unit cells at 5% strain level a) G2 design and b) G2 scanned unit cells.	Error! Bookmark not defined.
Figure 6-12: Analytical, FEA, and experimental results for E_{app}	153
Figure 6-13. Strain accumulation curves: a) G2, b) G4, and c) G24. d) Crack propagation rate for the three designs.	155
Figure 6-14: a) Internal porosity distribution in three gyroid lattice structures. Frequency of internal porosity along the x-direction in b) G2, c) G4, and d) G24.....	156
Figure 6-15: a) Calculation of ϵ_c and ϵ_f . Cyclic stress-strain for b) G2, c) G4, and d) G24.	157

Figure 6-16: Creep strain and fatigue damage strain for the three different designs: a) G2, b) G4, and c) G24..... 158

Figure 6-17: S-N curves of the G2, G4, and G24 gyroid lattice structures: a) global stress method and b) normalized global stresses method. 159

Figure 6-18: SEM micrographs of the fatigue fracture surfaces of the gyroid lattice structures, (a, b) multiple strut fracture surfaces, (c) possible initiation sites at the strut surface, d) higher magnification of striations. 161

Appendix B

Figure B - 1: Schematic illustration of the radially graded gyroid 178

Figure B - 2: The comparison of predicted and experimental fatigue life of G24 180

List of Tables

Table 2-1: Characterization of different lattice structures	25
Table 2-2: Summary for the different finite element (FE) models used to predict mechanical properties of lattice structure.	29
Table 2-3: Case studies for using FGM for biomedical implants	33
Table 3-1: SLM process parameters	58
Table 4-1: Chemical composition (wt.%) of the Ti6Al4V powder	83
Table 4-2: Process parameters and calculated volumetric energy density (VED) for each sample.	84
Table 4-3: Apparent density, strut size, and internal defect percentage of Ti6Al4V gyroid parts at three VED levels.	91
Table 4-4: Apparent modulus of elasticity and compressive strength of the gyroid parts at different VED levels.	96
Table 5-1: Element composition of used Ti6Al4V powder.....	109
Table 5-2: SLM Process parameters with the calculates VED in each case.....	112
Table 5-3: Mechanical properties results	120
Table 6-1: The SLM process parameters used for printing the gyroid parts.....	140
Table 6-2: The quantitative analysis of relative density, strut thickness, and internal defects for the Ti6Al4V gyroid lattice structures.....	148

Appendix A

Table A- 1: ANOVA test results for relative errors in $T_b T_h$	175
Table A- 2: ANOVA test results for relative errors in ρ_m	175
Table A- 3: Regression equations for estimation of relative error in $T_b T_h$ and ρ_m	175
Table A- 4: ANOVA test results for E_{app}	176
Table A- 5: ANOVA test results for σ_p	176

Table A- 6: Regression equations for E_{app} 176

Table A- 7: Regression equations for σ_p 176

Appendix B

Table B - 1: The stress levels, experimental fatigue lives, and crack initiation strains for G2 and G4..... 180

Table B - 2: Calculated material constants for G2 and G4 180

List of Abbreviations

AM	Additive manufacturing
ANOVA	Analysis of variance
CAD	Computer-aided design
CT	Computer tomography
DED	Directed energy deposition
D-I	Dense in
D-O	Dense out
DOE	Design of experiments
EBM	Electron beam melting
FEA	Finite element analysis
FEM	Finite element modeling
FGM	Functionally graded materials
HB	Hatching with borders
HNB	Hatching with no borders
LENS	Laser engineered net shaping
L-PGGs	Linearly porosity graded gyroids
MRI	Magnetic resonance imaging
N-G	Non-graded
OM	Optical microscope
PGG	Porosity graded gyroids
PSP	Process structure property
PBF	Powder bed fusion
R-PGGs	Radially porosity graded gyroids
RSM	Response surface methodology
SEM	Scanning electron microscope
SLM	Selective laser melting
STL	Stereolithography
TF	Total fill
TPMS	Triply periodic minimal surface
VED	Volumetric energy density
VED	Volumetric energy density

Nomenclature

P	Laser power
V	Laser scan speed
h	Hatch spacing
R_a	Average roughness
t	Layer thickness
$T_b T_h$	Trabecular thickness
ρ_d	Design relative density
ρ_m	Measured relative density
E_{app}	Modulus of Elasticity
σ_p	Compressive Strength

Chapter 1

Introduction

1.1 Background

Additive Manufacturing (AM) processes have evolved from printing parts used as prototypes to manufacturing parts that can be used as end products [1]. AM is defined by the American Society for Testing and Materials (ASTM) as “a process of joining materials to make objects from 3D model data, usually layer upon layer, as opposed to subtractive manufacturing methodologies”. Compared to traditional methods, AM has the capability of producing customized, complicated geometries without the need for tools and dies [2]. Thus, AM processes are well-suited for biomedical industries, where there is no need for mass production, but a particular necessity for customized implants that suits the anatomy of each specific patient [3]. The biomedical industry utilizes AM processes in various applications, including but not limited to medical education, tissue engineering, surgical planning models, organ printing, and orthopedic implants [4].

Orthopedic implants often refer to permanent joint replacements such as hip, knee and elbow implants, or temporary fracture fixation devices, such as screws, plates, and pins [5]. About 50 % of the orthopedic implants are manufactured from metallic materials [6], the most common metallic materials often used are titanium alloys, cobalt-chromium alloys,

and some stainless steel alloys [7]. Titanium alloys are highly employed in orthopedic implants due to its superior biocompatibility, corrosion, and wear resistance and mechanical properties that are close to that of natural bone [8]. Titanium alloys can be manufactured using AM processes, without the hassle of subtractive processes and the need for dies as in casting and forging, making it more cost-efficient [9]. Powder bed fusion (PBF) processes is one type of AM process that is capable of processing titanium powders efficiently.

The PBF processes are known for their relatively high accuracy and ability to create complex geometries. According to the ASTM F42 Committee [10], selective laser melting (SLM) is one of the powder bed fusion processes. A typical SLM process is schematically shown in Figure 1-1. In the SLM process, a laser source is used to melt the powder, and the fresh powder is placed in a delivery reservoir next to the building platform. A re-coater (roller/blade) lays down a uniform layer of powder from the reservoir on the building platform. The energy source (laser) scans across following a predefined path; this should fully melt the powder in this path and fuse it to the layer below (base plate for the first layer). The building platform is located on a stage and is lowered each layer; afterwards, the process is repeated until the desired part is completely printed. The whole process takes place in a closed chamber under inert gas protection (argon, nitrogen) to prevent oxidation of the parts during melting [11].

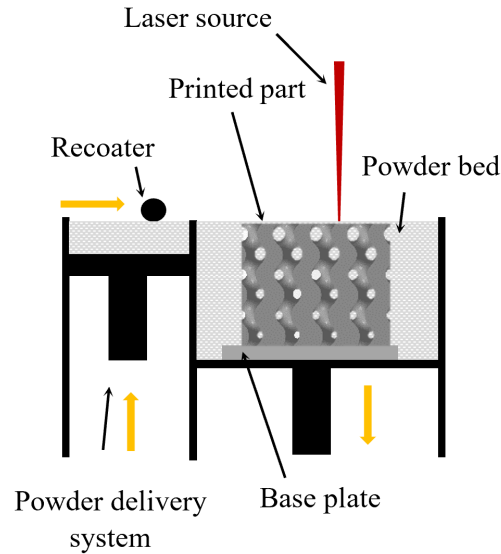


Figure 1-1: Illustration of a typical SLM process.

Titanium implants manufactured by SLM still have higher stiffness than natural bone. Thus they tend to carry most of the load, leaving the bone around them unloaded [12]. Bone requires continuous mechanical stimulation to remodel and regrow; otherwise, the bone will start reducing its mass by getting thinner or becoming more porous from around the implant [13]. This behaviour might lead to the stress shielding phenomena, where the bone resorption around the implant takes place, leading to complications such as peri-prosthetic fracture[14]. One possible solution to avoid stress shielding phenomena is to integrate designed porosities within the implant design [15]. Hence, it helps to reduce the implant's weight and, therefore, its stiffness.

Moreover, the designed porosities would allow bone cells to grow within the implant, helping the fixation and stability of the implant [16]. These designed porosities are often referred to as lattice structures, where the designed porosities are controlled by the unit cells forming those lattice structures. Lattice structures can be classified according to their

deformation behaviour (stretch or bending dominant) [17] , method of generation (Computer-aided design (CAD), image based, minimal surfaces or topology optimized) [18], lattice beam design (strut bases, minimal surfaces, shell based) [19]. Triply periodic minimal surfaces (TPMS) designs are biomimetic; they mimic bone geometry and may help with enhancing cell proliferation, making it more desirable for bone implant applications [20].

TPMS structures can have a skeletal based or sheet structures, the design of the unit cell would highly impact its properties. It is noteworthy to mention that comparative studies between sheet and skeletal TPMS have shown that sheet TPMS can have enhanced mechanical properties than skeletal gyroids [21]. However skeletal gyroids have lower values of modulus of elasticity which might be more efficient for bone implant applications [22]. Bone tissues are composed of a compact bone layer (cortical) that changes in porosity and distribution to form a less dense bone (cancellous) [20]. Biomimetic gyroid lattice can be designed to have porosity gradation, as illustrated in Figure 1-2. The change in pore size and distribution can be altered according to the implant position in the body and application.

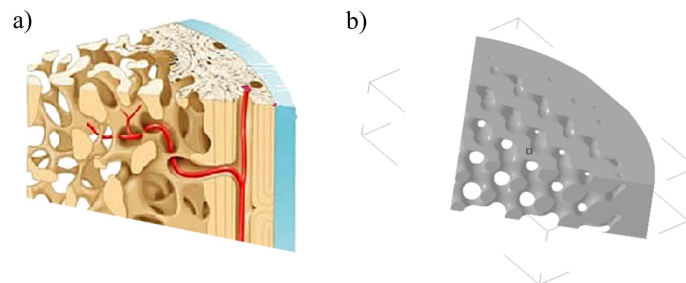


Figure 1-2: a) schematic diagram of cortical and trabecular bone and b) biomimetic porosity graded gyroid design

1.2 Motivation

The need for load-bearing implants has increased in the past few years. In Canada within the period from 2017 to 2018, around 130,000 hip and knee implant surgeries were performed as reported by the Canadian Joint Replacement Registry (CJRR) [23]. Although the industry is well evolved, some complications limit the success of these replacements, such as aseptic loosening, instability, wear, and misalignment [24]. Aseptic loosening can be defined as the failure of the implant without the involvement of bacteria. A possible reason for aseptic loosening is stress shielding [25]. Hence, a lot of research has been directed towards the design enhancement of these implants using AM techniques. The capabilities of AM techniques are not limited to their customization ability but also in modifying the implant design in an approach that conventional manufacturing methods are incapable of doing. The creation of a controlled metallic lattice structure that can help to solve the stress shielding problem and can also enhance osseointegration (bone growth); thus, the implant becomes customized and more fixed to the host bone.

1.3 Rationale

To date, most studies focus on the design aspect of lattice structures and how different designs can affect the mechanical properties for these designs. Very limited studies investigate the permissible design of lattice structures for bone implants, especially TPMS designs, and correlate them to bone-implant applications in terms of pore size and relative density. Moreover, improper choice of SLM process parameters may lead to inconsistency and low repeatability of the printed lattice structure. The interaction among the design aspects, SLM process, and mechanical characterization of TPMS lattice is not clear and needs more investigation.

1.4 Research objectives

The main objective of the research is to use the full capability of additive manufacturing to enhance the quality of printed gyroid lattice structures. The methods to optimize the SLM process for manufacturing porosity graded gyroids will be assessed. The objective can be further divided into the following sub-objectives:

- 1) Develop new gyroid designs that mimics the bone geometry.
- 2) Create permissible design maps for gyroid unit cells to understand the appropriate design space that can be used in biomedical implants.
- 3) Characterize the different defect types in gyroid lattice structures printed using SLM process.
- 4) Evaluating the Process-Structure-Property (PSP) relationships of gyroid lattice structures. By studying the effect of volumetric energy density and SLM process parameters on the quality of gyroid lattice structures.
- 5) Characterizing the quasi-static properties of the novel gyroid designs and their applicability for bone implant applications.
- 6) Study the influence of SLM defects on the quasi-static and fatigue properties of gyroid lattice structures.

1.5 Thesis outline

Overall, the main results of this thesis have been prepared into five journal articles, in which three articles are already published, one is accepted, and the other article is submitted to a peer-review journal. The thesis is divided into the following chapters:

Chapter 1 introduces the background, motivation, and objectives of the research, to frame the scope of the thesis

Chapter 2 is the first published journal article; it provides a comprehensive literature review of the additive manufacturing of lattice structures used in bone implants.

Chapter 3 is the second published journal article; it covers the first two objectives. The chapter describes in detail the design of gyroid lattice structures and provides a permissible design map that helps with the choice of design parameters for gyroid lattice structures used in bone implants. Moreover, the chapter presents the effect of different SLM scanning strategies on the quality of printed gyroid lattice structures.

Chapter 4 is an accepted journal article that presents the effect of printing the gyroid lattice structures at different volumetric energy density (VED), thus the third objective was met. The dimensional, defects, microstructure analysis and mechanical characterization of the gyroid lattice structures are discussed in detail.

Chapter 5 is the third accepted journal article and describes how the fourth and fifth objective were achieved. The chapter discusses the in-depth study on the process-structure-property relationship of selective laser melting of gyroid lattice structures. Moreover, it presents the design and mechanical characterization of the novel radial graded gyroid.

Chapter 6 is a journal article that explains the manufacturability of radial gyroids and uniformly graded gyroids. This chapter main objective was to focus on accomplishing the last goal of this thesis. It shows the influence of selective laser melting defects on the quasi-static and fatigue properties of gyroid lattice structures.

Chapter 7 summarizes the main conclusions and contribution of the thesis, highlights the strength and limitations and presents some suggestions for future work. Finally it defines the contribution of this thesis to the literature.

Appendix A presents the analysis of variance (AVOVA) test results to determine the significance of SLM process parameters on errors in relative density and strut size.

Appendix B presents a complementary analytical study on the fatigue properties of gyroid lattice structures.

1.6 References

- [1] M. Attaran, “The rise of 3-D printing: The advantages of additive manufacturing over traditional manufacturing,” *Bus. Horiz.*, vol. 60, no. 5, pp. 677–688, Sep. 2017.
- [2] T. DebRoy et al., “Additive manufacturing of metallic components – Process, structure and properties,” *Progress in Materials Science*, vol. 92. Elsevier Ltd, pp. 112–224, 01-Mar-2018.
- [3] J. D. Avila, S. Bose, and A. Bandyopadhyay, “Additive manufacturing of titanium and titanium alloys for biomedical applications,” in *Titanium in Medical and Dental Applications*, Elsevier, 2018, pp. 325–343.
- [4] M. Javaid and A. Haleem, “Additive manufacturing applications in medical cases: A literature based review,” *ajol.info*, 2018.
- [5] W. Jin and P. K. Chu, “Orthopedic implants,” in *Encyclopedia of Biomedical Engineering*, vol. 1–3, Elsevier, 2018, pp. 425–439.
- [6] MRFR/MED/2089-CR, “Medical Implants Market Research Report – Global Forecast To 2023,” 2018.
- [7] S. Bauer, P. Schmuki, K. von der Mark, and J. Park, “Engineering biocompatible implant surfaces. Part I: Materials and surfaces,” *Prog. Mater. Sci.*, vol. 58, no. 3, pp. 261–326, 2012.
- [8] F. Trevisan et al., “Additive manufacturing of titanium alloys in the biomedical field: processes, properties and applications,” *J. Appl. Biomater. Funct. Mater.*, no. 11, pp. 0–0, 2017.
- [9] T. Grover et al., “Role of titanium in bio implants and additive manufacturing: An overview,” *Mater. Today Proc.*, Mar. 2020.
- [10] ASTM International, F2792-12a - Standard Terminology for Additive Manufacturing Technologies. 2013.
- [11] I. Gibson, D. Rosen, and B. Stucker, *Additive manufacturing technologies: 3D printing, rapid prototyping, and direct digital manufacturing*, no. 3. Springer-Verlag New York, 2014.
- [12] S. Nasr Esfahani, M. Taheri Andani, N. Shayesteh Moghaddam, R. Mirzaeifar, and M. Elahinia, “Independent tuning of stiffness and toughness of additively manufactured

titanium-polymer composites: Simulation, fabrication, and experimental studies,” *J. Mater. Process. Technol.*, vol. 238, pp. 22–29, Dec. 2016.

[13] H. M. Frost, “Skeletal structural adaptations to mechanical usage (SATMU): 1. Redefining Wolff’s law: The bone modelling problem,” *Anat. Rec.*, vol. 226, no. 4, pp. 423–432, 1990.

[14] S. Arabnejad, B. Johnston, M. Tanzer, and D. Pasini, “Fully porous 3D printed titanium femoral stem to reduce stress-shielding following total hip arthroplasty,” *J. Orthop. Res.*, vol. 35, no. 8, pp. 29–31, 2016.

[15] S. Arabnejad and D. Pasini, “Fatigue design of a mechanically biocompatible lattice for a proof-of-concept femoral stem,” *J. Mech. Behav. Biomed. Mater.*, vol. 22, pp. 65–83, 2013.

[16] J. Van Der Stok et al., “Full regeneration of segmental bone defects using porous titanium implants loaded with BMP-2 containing fibrin gels,” *Eur. Cells Mater.*, vol. 29, pp. 141–154, 2015.

[17] X. P. Tan, Y. J. Tan, C. S. L. Chow, S. B. Tor, and W. Y. Yeong, “Metallic powder-bed based 3D printing of cellular scaffolds for orthopaedic implants : A state-of-the-art review on manufacturing , topological design , mechanical properties and biocompatibility,” *Mater. Sci. Eng. C*, vol. 76, pp. 1328–1343, 2017.

[18] S. M. Giannitelli, D. Accoto, M. Trombetta, and A. Rainer, “Current trends in the design of scaffolds for computer-aided tissue engineering,” *Acta Biomater.*, vol. 10, no. 2, pp. 580–594, 2014.

[19] T. Maconachie et al., “SLM lattice structures: Properties, performance, applications and challenges,” *Materials and Design*, vol. 183. Elsevier Ltd, p. 108137, 05-Dec-2019.

[20] Z. Wang, C. Huang, J. Wang, P. Wang, S. Bi, and C. A. Abbas, “Design and Simulation of Flow Field for Bone Tissue Engineering Scaffold Based on Triply Periodic Minimal Surface,” *Chinese J. Mech. Eng. (English Ed.)*, vol. 32, no. 1, p. 19, Dec. 2019.

[21] S. C. Kapfer, S. T. Hyde, K. Mecke, C. H. Arns, and G. E. Schröder-Turk, “Minimal surface scaffold designs for tissue engineering,” *Biomaterials*, vol. 32, no. 29, pp. 6875–6882, 2011.

[22] O. Al-Ketan, R. Rowshan, and R. K. Abu Al-Rub, “Topology-mechanical property relationship of 3D printed strut, skeletal, and sheet based periodic metallic cellular materials,” *Addit. Manuf.*, vol. 19, pp. 167–183, 2018.

[23] Canadian Institute for Health Information, *Hip and Knee Replacements in Canada, 2017-2018*. 2019.

[24] K. Thiele, C. Perka, G. Matziolis, H. O. Mayr, M. Sostheim, and R. Hube, “Current Failure Mechanisms After Knee Arthroplasty Have Changed: Polyethylene Wear Is Less Common in Revision Surgery,” *J. Bone Jt. Surg.*, vol. 97, no. 9, pp. 715–720, 2015.

[25] M. Sundfeldt, L. V Carlsson, C. B. Johansson, P. Thomsen, and C. Gretzer, "Aseptic loosening, not only a question of wear: a review of different theories.," *Acta Orthop.*, vol. 77, no. 2, pp. 177–97, 2006.

Chapter 2

Lattice Structures and Functionally Graded Materials Applications in Additive Manufacturing of Orthopedic Implants: A review

Complete Citation:

Mahmoud, Dalia, and Mohamed A. Elbestawi. "Lattice structures and functionally graded materials applications in additive manufacturing of orthopedic implants: a review." *Journal of Manufacturing and materials Processing* 1.2 (2017):

13.<https://doi.org/10.3390/jmmp1020013>

Copyright:c

Reprinted with permission copyrighted by MDPI, 2017.

Relative Contributions:

Dalia Mahmoud: Wrote the first draft of the manuscript.

M. A. Elbestawi: Revised and edited the manuscript.

Abstract:

A major advantage of additive manufacturing (AM) technologies is the ability to print customized products, which makes these technologies well suited for the orthopedic implants industry. Another advantage is the design freedom provided by AM technologies to enhance the performance of orthopedic implants. This paper presents a state-of-the-art overview of the use of AM technologies to produce orthopedic implants from lattice structure and functionally graded materials. It discusses how both techniques can improve the implants' performance significantly, from a mechanical and biological point of view. The characterization of lattice structures and the most recent finite element analysis models are explored. Additionally, recent case studies that use functionally graded materials in biomedical implants are surveyed. Finally, this paper reviews the challenges faced by these two applications and suggests future research directions required to improve their use in orthopedic implants.

Keywords:

Additive manufacturing; orthopedic implants; lattice structure; finite element modeling; functionally graded material.

1.1 Introduction

Recent progress in Additive Manufacturing (AM) technologies has allowed for the development of novel applications in various industries. The aerospace, automotive and tooling industries, for example, are increasingly beginning to use AM technologies. AM is no longer just a rapid prototyping technique; in fact, the applications of AM in the medical segment are numerous [1]. Some of these applications include: the planning of surgical operations, printing of biodegradable tissues and, most importantly, the development of orthopedic implants. Moreover, the application of reverse engineering in AM technology ensures the customization of the printed implants [2]. The reverse engineering process starts with data acquisition, or obtaining the exact anatomical data from scanning techniques, such as computed tomography (CT) or magnetic resonance imaging (MRI). The 2D images can then be converted to a 3D CAD model using specialized software. Afterwards, the CAD model is converted to a stereolithography (STL) file to be fed to the AM machine for printing.

AM techniques are favorable, as compared to other traditional methods such as casting and forging, because of their ability to tailor the implant according to the patient's anatomy. Other various benefits of AM technologies include their lower cost, shorter lead time, and the lack of tooling as compared to other manufacturing methods. According to the ASTM committee F42 on additive manufacturing technologies, AM technologies can be classified into seven categories according to the state of the material used. These seven categories are material jetting, binder jetting, material extrusion, powder bed fusion, directed energy deposition, sheet lamination, and vat photopolymerization. Comparative studies outlining the advantages and limitations and applications of each method has been presented in

several reviews [3,4,5]. The techniques used for biomedical applications will be discussed in more details later in the review.

Different materials have been developed to suit the numerous functions of the orthopedic implants, including metallic, ceramic, and polymers. The material selection criteria may vary depending on both the application and the implant type. For instance, most of the load bearing implants are fabricated from metallic materials, since these have higher mechanical reliability than other materials [6]. On the other hand, for articulating surfaces, two material combinations are used: hard on soft couples and hard on hard couples [7]. The hard materials refer to metal and ceramics, while the soft materials refer to polyethylene. Some of the most suitable metallic biomaterials are titanium alloys, cobalt-chromium alloys, and various stainless steels [8]. One downside of metallic materials is the high stiffness and weight, which sometimes make them unsuitable for orthopedic implant. Therefore, a lot of research has been directed to reduce their stiffness and weight.

The most significant benefit of reducing the stiffness of the metallic material used in orthopedic implants is to avoid the “stress shielding” phenomenon [9]. This phenomenon is associated with the fact that the stiff metal implanted beside the bone will bear most of the load, leaving the bones with less load. Conforming to Wolff’s Law [10], bone requires continuous mechanical stimulation to regrow, or else it will start reducing its mass by getting thinner or becoming more porous (external and internal remodeling). Commercially pure titanium printed using AM technology showed low stiffness [11] when compared to other titanium alloys fabricated by powder metallurgy [12]. The replacement of aluminum elements by titanium showed a reduction of 5% in the stiffness of titanium alloys [13]. The use of porous metallic materials has also been considered for reducing metallic material stiffness [14].

The fabricated porosity also enhances the metallic material from the biological point of view, since porous metals have better osseointegration [15]. Osseointegration, first described by Bothe et al. [16] and Leventhal [17], denotes the fixation of synthetic material to bone without the formation of any other tissues. Thus, bone grows into the porous structure and enhances the fixation of the implant to the host bone. The designs that can be used by AM technologies to print porous implants are numerous, and the ability of AM to precisely control the shape and size of these porosities is impressive as well. Harryson et al. [18] were among the first groups to discuss the suitability of AM technologies for fabricating patient-specific implants. The fabrication of a femoral stem using a lattice structure was suggested to reduce stiffness while maintaining strength. Murr et al. [19] worked on the application of AM to manufacture customized implants, taking into consideration its ability to fabricate porous structures. Novel designs for the femoral and tibial components were suggested, and lattice structures were used instead of the porous coating. Therefore, cracking, de-attachment, and instability drawbacks resulting from porous coating were prevented. Bose et al. [20] focused on the application of AM in bone tissue engineering, wherein the mechanical properties of some 3D printed scaffolds material were summarized.

Another advantage of AM is the possible printing of functionally graded materials (FGM). FGM are materials that vary in composition or microstructure following a certain design law [21]. A major benefit of these materials over composite and coated materials is that for FGM, the variation in composition is gradual, which reduces the stress concentration effects near the interface between different phases [22]. The human body is composed of several functionally graded materials, the most important of these being bone and teeth. Bone tissues are composed of compact bone layer (cortical) that changes in porosity and

distribution to form a less dense bone (cancellous) [23]. Since bones and joints are prone to failure due to natural wear or accidents, there is a need to mimic natural joints and fabricate orthopedic implants with FGM. The use of FGM can ensure improvement in both the mechanical properties of implants and the interaction of the implant with the host body [24]. The 3D printing of load bearing implants having FGM was discussed by Sola et al. [25]. Several research case studies have been recently proposed, as will be discussed later.

This paper aims to focus on the applications of lattice structures and FGM in the orthopedic implants industry, more specifically concerning load bearing implants. Although the customization of implants is a key factor in choosing AM technologies as a manufacturing method for implants, the ability to print implants using lattice structures and FGM is an important added benefit. In what follows, manufacturing of lattice structures using AM technologies is first discussed, followed by a description of how lattice structures can be characterized to evaluate its performance. One contribution of this review is the emphasis on the numerical modelling of lattice structures, illustrating the difference between different modelling methods reported in the literature. In addition, the manufacturing of FGM using AM technologies is presented, and various types of FGM that can be applied in orthopedic implants are discussed. Finally, some challenges are discussed to identify future research directions for both lattice structures and FGM applications in orthopedic implants.

2.1 Lattice structures

2.1.1 Classification

The terms cellular material and lattice structure are often used interchangeably in the literature; in fact, the lattice structure is one type of cellular material [26]. Cellular materials

are usually classified according to their porosity type (open, closed) and their building unit cells order (stochastic, non-stochastic). There are several applications for cellular materials including heat exchangers, filters, load bearing components, and biomedical implants [27]. Some typical examples of cellular materials are: foam, honeycomb, sponges, folded materials and lattice structures. Lattice structures are characterized by open pores and non-stochastic orientations of the building unit cells. The unit cell geometry and topology are used to tailor the mechanical properties of the part. Tan et al. [28] indicated that the unit cells used in biomedical implants can be classified according to their form or deformation behavior. The form of the unit cells can be reticulated or stochastic. If the unit cells are arranged in a specific order, they are called reticulated (non-stochastic). The deformation behavior dictates how unit cells fail, and this behavior can take the form of stretching or bending. Reticulated meshes were found to be favorable to stochastic meshes when mechanical properties were compared, while stretch dominated unit cells proved to be more satisfactory in orthopedic implants than bend dominated unit cells [28].

The lattice structures used in tissue engineering and bone scaffolds is usually classified according to the unit cells design. This design can be divided into the following four groups: CAD-based [29], image-based [30], implicit surfaces [31], or topology optimized unit cells [32]. Figure 1 represents the different types of lattice structures used in biomedical implant applications. The CAD-based design uses unit cells that are adopted from Platonic and Archimedean polyhedral solids [33]. Examples include simple cube, diamond, tetrahedral, and dodecahedron unit cells. Implicit-based unit cells, are sometimes referred to as triply periodic minimal surfaces (TPMS). These minimal surfaces are based on the concept of the differential geometry of surfaces [34] and are gaining attention in bone tissue engineering as they have a mean curvature of zero, like the trabecular bone. An

example of TPMS based on implicit surfaces is the gyroid and Schwartz's diamond unit cells [35]. Load bearing implants have multiple requirements, such as low stiffness, high strength, and high permeability. Recent research has been oriented towards the topology optimization (TO) of the base unit cell [36]. This technique relies on numerical methods to change the shape of the unit cell to satisfy the multiple objective functions required for enhanced performance.

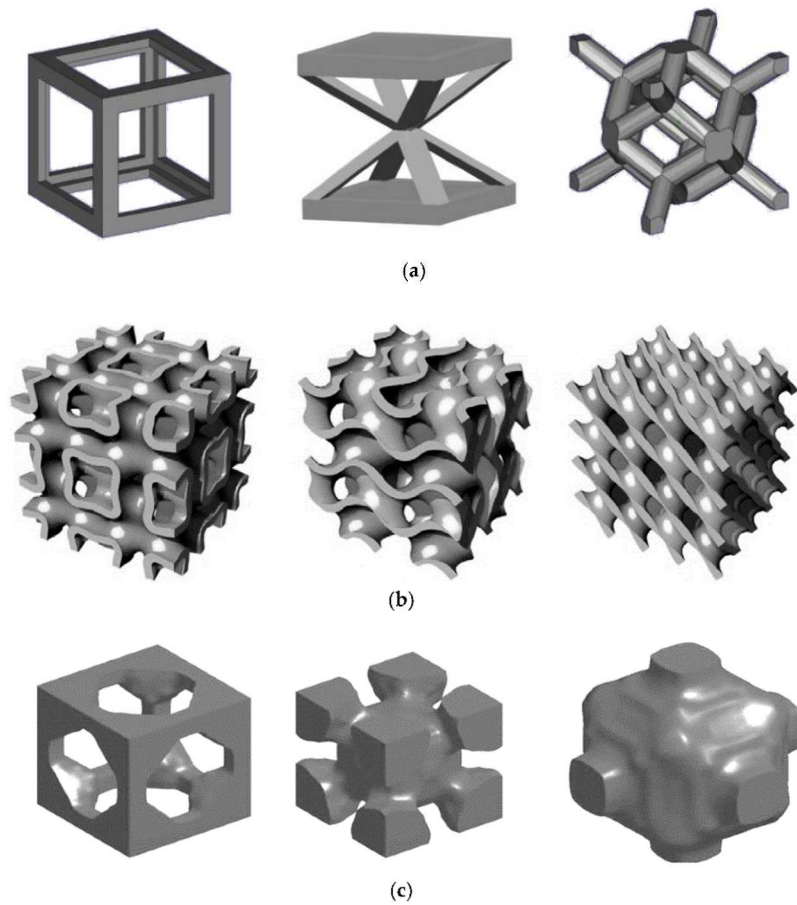


Figure 2-1: Different unit cell designs of lattice structures used in biomedical implants. (a) CAD-based unit cells [37]; (b) Implicit surface based unit cells [34]; (c) Topology optimized unit cells [38].

2.1.2 Manufacturing

Various manufacturing methods have been used to create porous metallic implants, including powder metallurgy [39,40], metal foaming techniques [41], and space holder methods [42]. However, these techniques are limited to fabricating randomly organized porous structures, providing limited control of pore size, geometry, and distribution. AM processes, on the other hand, offer methods capable of manufacturing parts with a predefined customized external shape, as well as providing accurate control of internal cell geometry [43]. A comparison between conventional manufacturing methods and AM technology was provided by Rashed et al. [27]. AM technologies were clearly distinguished due to their accuracy and precision. Therefore, they are now being used more frequently than other methods. As discussed in the introduction, metallic materials are the most common materials used for load-bearing implants.

The powder bed fusion technique (PBF) and the directed energy deposition method (DED) are the most common AM technologies used to print metallic orthopedic implants. In PBF, an energy source (electron or laser beam) is used to selectively melt parts of the powder bed based on the data fed to the machine. When one layer is fused, the building platform is lowered by a predetermined distance via a piston. A mechanical coater (roller or blade) places a new layer of powder on top of the platform, and the process is repeated until the final shape has been reached [4]. The literature reports two main PBF technologies that can print metallic parts. These are Electron Beam Melting (EBM) and Selective Laser Melting (SLM). The second AM technology, DED, is also known by the commercial name laser engineering net shaping (LENS). In DED, an energy source (electron or laser beam) is used to build complex parts as the material is being deposited from a nozzle [4]. Material can take the form of powder or wire, and there is no powder bed to support the parts as in PBF.

Parts are built directly on the substrate, so this method has the advantage of being able to build new parts or fix old ones.

SLM and EBM are both more accurate and can achieve a better resolution. Therefore, they can be used to print lattice structures. LENS, on the other hand, can be used to print porous structures without the capability of controlling the unit cell size or shape. Irregular porous structures have been fabricated using LENS where porosity is controlled by the laser power and scanning speed [44]. When comparing SLM, EBM, and LENS, some differences are noted in the mechanical properties of the printed part. These differences are usually related to the difference in the microstructure of the parts [45]. The high energy resulted from the EBM is attributed to the electron energy source, thus fully dense parts can be printed. SLM has higher cooling rate than EBM, resulting in coarser microstructure, higher tensile strength, and lower ductility than parts [46]. Both SLM and LENS were used to produce commercial pure titanium samples with mechanical properties better than conventional methods [47]. The cooling rate in SLM is also higher, which resulted in finer microstructure and therefore produced more desirable mechanical properties.

The dimensional and mechanical properties of lattice structures can be improved by choosing the optimum process parameters [48]. For SLM, the most significant process parameters are laser power, scan speed, hatch spacing, and layer thickness. Overall energy input was found to be the most significant factor affecting the dimensional accuracy. The energy input can be calculated from the laser power, scan speed, and the laser spot diameter. Moreover, the higher the energy input, the more susceptible the strut is to have internal porosity [48]. Ahmadi et al. [49] studied the effect of laser power and exposure time on the mechanical properties of lattice structures. The diamond unit cell was studied, where the authors developed a novel method of printing the lattice by using a vector-based

approach. The struts were defined by their start and end coordinates in the absence of diameter data. Therefore, the laser power and exposure time were used to determine the strut diameter. Since maximum laser power with maximum exposure time will develop a thick strut, the highest mechanical properties were obtained at this point. Another important factor that can affect the lattice structure's mechanical properties is the build orientation. It was noted that the horizontal struts of the diamond unit lattice structures had the worst quality in terms of dimensions and internal porosity, leading to its poor mechanical properties [50].

Statistical analysis can be used to determine which of the process parameters have the most significant effects on lattice structures. Sing et al. [51] used analysis of variance (ANOVA) to determine the most significant factor in determining the elastic constant of lattice structures. In their study, laser power, scan speed, strut diameter, and unit cell shape were varied, and the mechanical properties of lattice structures was evaluated. It was found that only the cell geometry and strut diameter effected the elastic constant. These two parameters changed the porosity of the structure, which is directly related to its stiffness. In a further study, the same authors used a regression analysis to study the effect of process parameters on the dimensional accuracy of lattice structures [52]. The lattice structure examined had simple cube unit cells, having diagonal struts on all four sides. In this study, the laser power, scanning speed, and layer thickness of an SLM machine were changed, and the horizontal, vertical, and diagonal struts were characterized. The experimental results show that laser power has the most significant effect on dimensional accuracy, porosity, and stiffness.

Dimensional accuracy plays an important role in obtaining the proper mechanical properties of lattice structures. The proper choice of process parameters results in better

and enhanced lattice structure quality [53]. More research is needed in this area to investigate different unit cells (implicit and topology optimized), different materials, and different pore sizes. Moreover, appropriate dimensional and mechanical characterization protocols should be put in place to ensure the proper characterization of different lattice structures.

2.1.3 Characterization

Achieving the accurate characterization of lattice structures is necessary for several reasons, including assessing the quality of printing. Characterization includes microstructure, dimensional, and mechanical properties. The microstructure of lattice structures is expected to be different than that of bulk, since its strut thickness decreases significantly as compared to bulk parts. Another factor impacting the microstructure is the cooling rate, which depends on the thickness of the part being printed [54]. Algardh et al. [55] investigated the change in microstructure for different wall thicknesses printed using EBM. It was noticed that the thinner the wall, the faster the cooling rate, and the finer the grain structure. Cheng et al. [56] studied the microstructure of lattice structures and concluded from their experimental work that, as the strut thickness decreases, the hardness increases. Dimensional characterization is related to the evaluation of the strut size, pore size, and pore shape. A few techniques are used in the literature to measure this diameter/size, such as optical microscopes (OM), scanning electron microscopes (SEM), and micro computed topography (CT) [57].

The mechanical properties of lattice structures depend mainly on the following three parameters: the material, the cell topology, and the relative density of the part [58]. One technique used to assess the mechanical properties of lattice structures is to perform a static compression test for the printed samples. The difference in mechanical properties

between a stochastic foam and a non-stochastic lattice structures was evaluated by Cheng et al. [56]. The non-stochastic lattice was found to have higher specific strength than that of the foam specimens. Li et al. [37] studied the effect of different unit cells on the mechanical properties of lattice structures that could be used in biomedical applications. It was suggested that the mechanical properties depend mainly on the failure mechanism of the unit cell being either bending or stretching dominated. Ahmadi et al. [59] studied the effect of unit cell design and porosity on the mechanical properties of lattice structures. It was noted that stiffness decreased with the increase of porosity, which is desirable for reducing the stress shielding effect. Yáñez et al. [60] evaluated the compressive behavior of gyroid lattice structures for cancellous bone applications. The strut angle was found to be a critical factor that affected the compressive properties: as the strut angle decreased, the stiffness and compressive strength increased.

Although increasing the controlled porosity reduces the stiffness and provides space for bone ingrowth, fatigue properties may suffer [61]. Therefore, relying on static mechanical tests alone is not sufficient. More research should investigate the fatigue properties of lattice structures. The effect of porosity and unit cell shape on the fatigue strength of lattice structures was investigated by Harbe et al. [62]. Normalized fatigue strength was found to be less than that of solid samples of the same material. This difference was traced to the presence of stress concentrations (from un-melted powder or closed pores) and the martensitic microstructure resulting from the process. Yavari et al. [63] investigated the effect of different unit cells and porosity on the fatigue properties of a titanium lattice fabricated by SLM. It was noted that high porosity structures had shorter fatigue life than structures with low porosity. In addition, it was noted that, for some unit

cells, the fatigue resulted in compressive loading of the struts. This led to the shrinking of the fatigue cracks which enhances fatigue life.

The dimensional characterization, mechanical properties, and fatigue properties of some lattice structures reported on in recent literature are summarized in Table 1. It is noted that both the material and unit cell shape play a key role in defining the mechanical and fatigue properties of lattice structures. As expected, the higher the relative density, the better the yield and normalized fatigue strengths. The stiffness values for different lattice structures follows the same pattern as the yield strengths [64]. The difference between nominal values and measured values could be traced back to defects resulting from poor choice of process parameters. Additional research in this area should focus on creating process-structure-property (PSP) relationships to relate the defects of AM processes with their root causes. Data on the mechanical properties for the different unit cells are still limited, and more information about different biomaterials is still needed. The possible combinations of different unit cell size, shape, and porosity lead to numerous design options. Therefore, accurate numerical modelling is needed to assess the mechanical properties of lattice structures.

Table 2-1: Characterization of different lattice structures

Unit Cells	Material/Method	Relative Density (%)		Pore Size (μm)		Strut Size (μm)		Yield Strength (Mpa)	Normalized Fatigue Strength at 10^6 Cycles	Ref.
		Nominal	Measured	Nominal	Measured	Nominal	Measured			
Cube	Ti-6AL-4V/SLM	24.2–39.1	29.7–49.3	2040–1000	1960–765	450–800	466–941	7.28–163.02	---	[65]
	Ti-6AL-4V/SLM	11–34	11–36	1452–1080	1413–1020	348–720	451–823	29.9–112.6	$0.2 \sigma_y$	[63]
Diamond	Ti-6AL-4V/EBM	17–40	---	1540–570		430–570	---	19.1–112.73	$0.15-0.25 \sigma_y$	[62]
	Ti-6AL-4V/SLM	20–33	17–36	1040–807	1142–826	234–693	350–564	6.8–70.6	$0.32 \sigma_y$	[63]
Dodecahedron	Ti-6AL-4V/SLM	10–34	11–32	1250–950	1305–920	250–550	246–506	~10–120	---	[59]
	Ti-6AL-4V/SLM	---	15.8–31.6	500–450	608–560	120–230	140–251	19.4–117.2	$0.12 \sigma_y$	[61]
	CP Ti/SLM	19–34	18.3–33.7	500–450	---	120–230	---	8.6–36.9	$0.32-0.51 \sigma_y$	[66]
Truncated cuboctahedron	Ti-6AL-4V/SLM	18–36	19–36	1024–807	1142–862	324–693	350–564	~30–150	----	[59]
	Ti-6AL-4V/SLM	11–34	13–37	1452–1080	1413–1020	348–720	451–823	41.4–110.1	$0.35 \sigma_y$	[63]
Gyroid	NiTi/SLM	21.7	25.2	850	---	320	298	29	$0.2 \sigma_y$	[67]
	Ti-6AL-4V/SLM	5–20	---	1600–560	---	---	---	6.5–81.3	---	[68]
	Ti-6AL-4V/SLM	31–49	38–52	---	464–406	169–261	258–330	~120–240	$\sim 0.6 \sigma_y$	[34]

2.1.4 Modelling and validation

Finite element methods (FEM) can be used to predict the mechanical properties of lattice structures and test the several possibilities of different unit cell shapes and sizes. One major benefit of these methods is that they reduce a significant amount of the experimental work needed to fully characterize the printed lattice structures. Another key advantage for using FEM is that a detailed stress-strain distribution can be obtained, which is useful for the design optimization of lattice structures. Moreover, FEM can be used to evaluate the failure modes of lattice structures, which is important for biomedical implants. The accuracy of FEM depends on the material properties assigned to the model, the meshing element geometry (struts representation), size (finite or infinite), and the model design (CAD/implicit surface).

The material properties of struts are needed to be known for characterization, since this information will affect the predicted results. Yavari et al. [61] predicted that using the same energy density in all lattice structures would result in the same material properties and that there would be no significant differences between the bulk and strut material properties. Experiments performed by Tsopanos et al. [69] indicated a reduction of 74% in the stiffness of struts as compared to bulk. The difference was attributed to the drastic change in surface area, orientation angle, and laser exposure time when printing struts. The mesh elements used can be classified into one dimensional (1D) and three dimensional (3D) models. The 3D mesh elements deal with the struts as a volume rather than a beam, meaning that better accuracy can be obtained, but longer computation time is needed. Gumruk et al. [70] attributed deviations between numerical models with 1D and 3D elements to the fact that the 1D models cannot represent the actual material volume at the nodes. Smith et al. [71]

suggested increasing the material volume at the nodes of the lattice structures to enhance the accuracy of 1D mesh elements. The size of the model is another important factor to be considered.




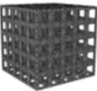


With infinite models, only the periodically repeating part of the structure is modeled; thus, a small model size can be obtained, and less computation time is required than with finite models. Finite models were found to be more accurate when predicting the mechanical properties of implants made from lattice structures, since they are more accurate [72]. Reducing the volume of the CAD model by voxelization is a research direction being pursued to reduce the computation time in FEA modelling. Where the 3D model is presented in a discretized method instead of continuous [73], this technique represents the model as discrete voxels that give a suitable approximation for the continuous model. Dumas et al. [74] proposed a novel approach to model the lattice structures: the model itself was generated in MATLAB using the voxelization method. It was proved that this model would require less computation time as compared to those designed in CAD software. The difference between both experimental and numerical techniques are considerably high, reaching an average of 40%. Another method proposed to reduce the volume of CAD models is to use voronoi tessellations [75]. This method requires less space; however, it might not be able to mimic abrupt changes in the lattice as well as CAD designs.

The difference between numerical and experimental results can be traced to several factors, including the process parameter's effect on the build, un-melted powder, and broken struts if they exist in the part [76]. Campoli et al. considered the strut variation diameter and the internal porosity defects resulting from the EBM process when modelling lattice structures. Gonzalez et al. [77] proposed accounting for three manufacturing errors: strut diameter variation, strut inclination, and fractured struts. Although these methods will reduce the

significant gap between numerical and experimental results if successfully applied, the application of such methods on different unit cells requires significant dimensional characterization and may be challenging to achieve.

Table 2 summarizes some of the recent and important research that has been conducted on the modelling of mechanical properties of lattice structures used in biomedical implant applications. The different mesh size, material property, model size, model input, and deviations between experimental and numerical results are presented. The 3D mesh elements and finite size are preferred when modelling small objects, such as those needed for biomedical applications. It was noted that most of the research conducted assumes the material property model to be the same as the bulk material. Although voxelization can reduce the numerical modelling computation time, more effort is needed to improve the complex geometrical representations of this method. Finally, the gap between experimental and numerical modelling is presented. One possible approach to reducing the gap between numerical and experimental results is to develop methodologies for optimizing process parameters, thus limiting manufacturing errors.

Table 2-2: Summary for the different finite element (FE) models used to predict mechanical properties of lattice structure.

Unit Cell	Material/Method	Material Model	Element	Model Size	Input Model	Stiffness Prediction Deviation between Numerical/Experimental	Ref.
 BCC ¹	Stainless steel/SLM	Same as bulk	1D and 3D	Infinite	CAD	Underestimated by 10% when using 1D elements Initial prediction is acceptable in 3D elements,	[70]
	316 L SS/SLM	Less than bulk	1D and 3D	Finite	CAD	Overestimated by 15% 1D and 3D mesh elements	[71]
	Ti-6AL-4V/SLM	Same as bulk	3D	Finite/Infinite	CAD	Overestimated by 5% finite Overestimated by 9% infinite,	[78]
 BCC-Z ²	316 L SS/SLM	Less than bulk	1D and 3D	Finite	CAD	Overestimated by 5% 1D mesh elements 30% by 3D mesh	[71]
 Diamond	Ti-6AL-4V/SLM	Linear isotropic	3D	Finite	CAD	Overestimated by an average of $27.5 \pm 3.1\%$	[76]
	Ti-6AL-4V/SLM	Same as bulk	3D	Finite	Voxel mesh	Overestimated by 40%	[74]
	Ti-6AL-4V/SLM	Elastic-plastic model	3D	Infinite	CAD	Overestimated and underestimated by 6–21%	[79]
 Cubic	Ti-6AL-4V/EBM	----	1D	Finite	CAD	Overestimated specially in high densities	[80]
	Ti-6AL-4V/SLM	Elastic-plastic model	3D	Infinite	CAD	Overestimated by 21–117%	[79]
 I-WP ³	Ti-6AL-4V/SLM	Elastic-plastic model	3D	Finite	Voxel mesh	Underestimated by 6.6% (30% relative density) Overestimated by 10.2% (45% relative density)	[81]
 F-RD ³	Ti-6AL-4V/SLM	Elastic-plastic model	3D	Finite	Voxel mesh	Overestimated by 31.6%	[81]

¹ BCC: Body centered cube. ² BCC-Z: Body centered cube with a vertical strut in the middle. ³ I-WP and F-RD: are TPMS unit cells based on implicit equations.

2.2 Functionally Graded Materials

2.2.1 Classification and manufacturing

FGM can be classified into three distinct groups: gradient microstructure, gradient composition, and gradient porosity [82]. Figure 2 represents a schematic illustration of the three different types of FGM. The functionally graded composition can be defined as “A change in composition across the bulk volume of a material aimed to dynamically mix and vary the ratios of materials within a three dimensional volume to produce a seamless integration of monolithic functional structures with varied properties” [83]. FGM can provide an enhanced substitute for the coating in orthopedic implants, thus avoiding the sudden change in chemical composition and the “peeling-off” effect of the coated layer [84]. Functionally graded coating (FGC) was developed prior to FGM. The fabrication of FGC can be accomplished using vapor deposition techniques, plasma spraying, and Ion Beam Assisted Deposition (IBAD) [85]. These methods are energy extensive and are therefore not suitable for bulk FGM parts fabrication. Techniques like powder metallurgy [86] and the centrifugal method [87] are more commonly used in the fabrication of bulk parts. However, the 3D shapes obtained from these techniques are relatively simple and limited to cylinders or blocks. Accordingly, AM technologies may be considered a suitable method of fabricating customized parts with the required accuracy [25]. The ability to use more than one material using the DED technique is employed to print FGM parts from two, and sometimes three, materials.

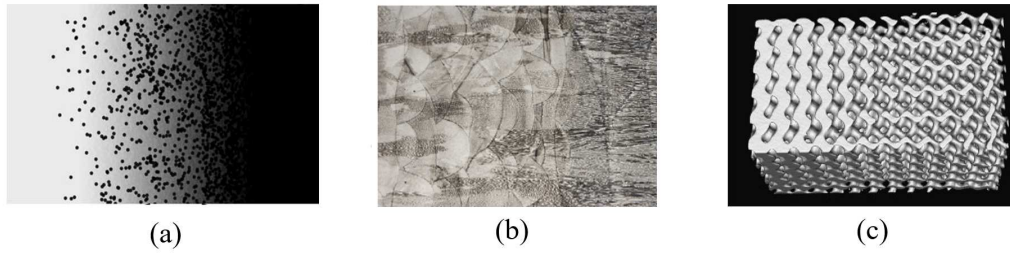


Figure 2-2: Classification of FGM according to (a) composition, (b) microstructure, (c) porosity

Functionally graded porosity can be created in materials by changing the porosity across the bulk volume. The variation in density will combine variation in mechanical properties, which can make the part more functional than a single constitutive material for some applications. Parts of the implants with low porosity have high mechanical stability, while high porosity regions support bone ingrowth and help with the implant's fixation [88]. The functionally graded porosity can be manufactured using any method used to fabricate lattice structures, as mentioned earlier. However, AM remains an attractive method for fabricating such structures with the required geometry and precise control of unit cells [89]. Two common AM technologies used to print this type of functional gradation are PBF and DED technologies. In general, when using the DED technique, porosity shape, size, and distribution cannot be controlled [90]. Differentially, the use of PBF techniques, like SLM and EBM, can result in precisely controlled pores that follow a specific design rule in size and allocation [91].

A material with varying microstructures along its volume could be achieved by controlling heat treatment. This recent progress in the fabrication of gradient microstructures was investigated by Popovich et al. [92]. In this study, the precise control of laser power and scanning speed of a DED technology was used to create specimens of graded

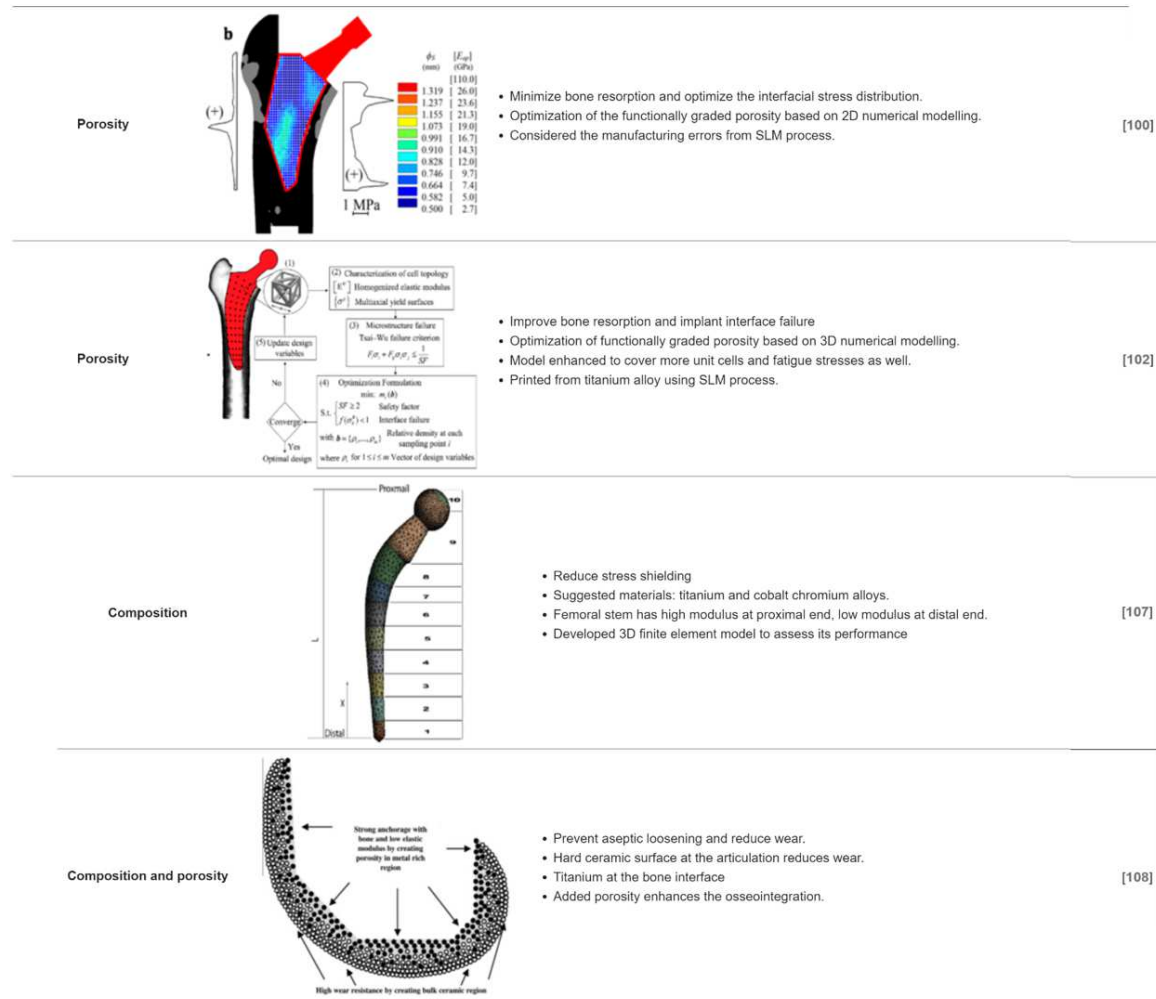
microstructure in Inconel. The advantage of this technique is that a tougher core can be obtained, with a hardened surface that would increase wear resistance. Although this technique has not been applied in the biomedical realm, it suggests a direction for improving the hardness of articulating surfaces

2.2.2 Case Studies

The aim of most research is to use FGM in orthopedic implants to achieve a better mechanical or biological advantage. Several advantages can be achieved, such as improving the fixation of implant to bone, enhancing the stress shielding phenomena, hardening the articulating surface, and removing interfacial stresses between the implant and bone. The method used to evaluate the performance of the implant is usually based on numerical optimization. The use of FGM in orthopedic implants reported in the available literature has been limited to gradation in porosity and composition. Most of the case studies discussed numerical models, but only a small amount of research has validated the model by using AM technologies. In this section, some examples of functionally grading porosity will be illustrated, followed by examples of functionally graded composition. A detailed description for some important case studies from the literature is presented in Table 3.

Table 2-3: Case studies for using FGM for biomedical implants

FGM Type	Proposed Design	Description	Ref.
Porosity		<ul style="list-style-type: none"> Enhance joint stability An increase in strut diameter of octet truss unit cell from the exterior to inner surface is proposed Mechanics analysis of the design was provided. 	[95]
Porosity and Composition		<ul style="list-style-type: none"> Enhance joint stability and reduce wear. Cobalt alloy mating with the metallic part to reduce the wear rate. Porous titanium alloy mating with the bone to enhance osseointegration and stability. 	[96]
Porosity		<ul style="list-style-type: none"> Reduce the stress shielding effect A porous femoral stem with a functionally graded square pore cellular structure. Strut thickness changes from thin to thick towards the femoral head. Printed from Co-Cr alloy using the SLM process. Validation by the cantilever bending test. 	[97]
Porosity		<ul style="list-style-type: none"> Reduce the proximal bone stress shielding, while preserving the stability. Comparison of axially and radially gradation using a developed 3D model. Octahedron unit cell was used for the functionally gradation. Printed using Co-Cr alloy and the SLM process and validated by the 3-point testing method. 	[99]



An implant's stability after implantation depends on the pore shape and size of the implant surface facing the host bone. Wang et al. [95] suggested the use of SLM to print a functionally graded porosity for the acetabular cup to enhance its stability after implantation. The proposed lattice structure had octet truss unit cells that varied in length across its design. Mathematical analysis and manufacturability issues for the proposed design were discussed, and it was shown that this design could withstand the maximum stresses that this area is usually subjected to in normal daily activities. España et al. [96] also suggested the use of the DED process to print an acetabular cup from functionally graded composition. For the part mating with the femoral head, cobalt alloy was suggested. For the part mating with the bone, titanium alloy with fabricated porosity was proposed. DED techniques have the advantage of printing more than one material. However, they cannot obtain precise and controlled unit cell shapes, as can SLM.

To reduce the femoral stem stiffness and avoid the stress shielding phenomena, the use of functionally graded porosity is a new approach that has recently generated significant attention. Hazlehurst et al. [97,98] proposed the fabrication of an implant from cobalt-based alloys using SLM. The internal lattice for the design had a simple cube shape. A 3D FEA model was developed to model the proposed designs. An experimental cantilever bending test was performed to validate the efficiency of the designs. Both experimental and numerical results proved that functionally graded porosity would reduce overall stiffness. However, a difference between experimental and numerical results was noted. The difference, in this case, was attributed to the SLM accuracy and manufacturing errors. Functionally graded porosity in both axial and radial directions of a CoCr femoral stem have been suggested by Limmahakhun et al. [99]. This innovative design was proposed to

work on solving the proximal bone stress shielding problems while also trying to maintain the implant's stability. The unit cell chosen for this lattice structure was pillar octahedron. A 3D FEA analysis model was developed to evaluate the stress shielding effect on the implant. Furthermore, a three-points bending test was performed for the printed femoral stems to validate the model. Numerical and experimental results both proved an enhancement in the stress shielding effect when compared to solid titanium femoral stems.

The use of optimization models to numerically assign the porosity in the femoral stem is another promising approach. Fernando [100] proposed an optimization method to reduce the stress shielding and the interfacial stresses. The developed FEA model considered the additive manufacturing errors. The proposed model was a 2D model, which might be a significant approximation. Arabnejad et al. [101] proposed a similar optimization method based on the homogenization concept. The authors were able to develop a 3D FEA model and extended their research to cover femoral stems generated from a tetrahedron unit cell lattice structure [102]. The same authors extended their optimization method to enhance the design of the implant against fatigue fractures [103] caused by the cyclic loading associated with walking stresses. This opens a wide area of research possibilities to experiment with other lattice structure unit cells, such as gyroids, and evaluate their performance in the fully porous femoral stem.

The functionally grading of metals with other materials such as ceramics and hydroxyapatite has shown superior performance results and increases in service life of implants in several case studies. A 3D FEM was developed by Oshkour et al. [104,105] for the femoral component of a knee through functionally graded composition. Three different material combinations were suggested: titanium, cobalt chromium, and hydroxyapatite. Hedia et al. [106] compared numerical models of 1D FGM and 2D FGM for the acetabular

cup of a hip implant. A combination of titanium, bio-glass and hydroxyapatite was suggested. All numerical results pointed toward a reduction in stress shielding. Low modulus at the distal end and high modulus at the proximal end was suggested by Al-Jassir et al. [107] to improve the performance of the femoral stem. The proposed material combination was titanium alloy and cobalt chromium alloy, which may be challenging to grade together. To overcome aseptic loosening, Bahraminasab et al. [108] suggested using a gradient from titanium alloys and alumina-ceramic for a knee femoral component. Moreover, some porosity was added to the surface of the implant mating with the bone to improve fixation and eliminate the effect of soft tissue formation. The manufacturing of such a part using AM technologies could only be done using DED in the present time. The bonding of the metallic and ceramic material needs to be further researched, specifically when printing complex parts, to validate the model.

2.3 Challenges and future directions

The employment of lattice structures and FGM in the design and manufacturing of orthopedic implants should have a promising future. In order to substantially increase the use of these technologies in the biomedical implant industry, several challenges need to be addressed:

- The overall characterization of the lattice structure needs to be improved. A standard protocol for assessing the dimensions/microstructure/mechanical performance needs to be developed.
- There is a need to trace the defects of lattice structures manufactured by AM technology to their root causes. This can be performed by creating process-structure-property (PSP) relationships for different lattice structures.

- A library for the different unit cells used in orthopedic implants should be established to allow for the assessment of different unit cells' performances in different applications. Moreover, the database should contain both mechanical and biological information about the different unit cells.
- The development of new FGM designed from biomaterials using AM technologies should be studied in more depth. The combination of metallic, ceramic and inorganic materials could result in an implant having high functionality.
- Integration between the simulation and AM of implants fabricated from FGM is needed to ensure that the gap between modelling and fabrication is eliminated.
- The long-term performance of functionally graded implants produced by additive manufacturing technologies needs to be assessed. The in vivo performance would determine the benefits and limitations from a biological point of view.

2.4 Conclusions

This review highlights that AM technologies can add more benefits to the key advantage, which is customization, in the manufacturing of the orthopedic implants. Lattice structures can be used to reduce stress shielding and enhance osseointegration, while the use of FGM addresses significant issues such as: stress shielding, implant stability and aseptic loosening. To obtain high quality lattice structures, the process parameters of AM technologies need to be optimized. Different factors affect the mechanical properties of these structures, such as: material, shape of unit cells and porosity. More accurate FEA models should be developed to assess the seemingly limitless combinations that could be obtained from these factors. AM technologies have been studied to create functionally graded composition implants, as well as functionally graded porosity for customized

implants. The modelling of the biological and mechanical performance of implants fabricated from FGM has been well established. More experimental studies are needed to validate these models and further enhance their applicability in orthopedic implants.

2.5 References

- [1] S. A. M. Tofail, E. P. Koumoulos, A. Bandyopadhyay, S. Bose, L. O’Donoghue, and C. Charitidis, “Additive manufacturing: scientific and technological challenges, market uptake and opportunities,” *Mater. Today*, vol. 0, no. 0, pp. 1–16, 2017.
- [2] I. Gibson, *Advanced manufacturing technology for medical applications*, vol. 53, no. 9. John Wiley & Sons Ltd, England, 2005.
- [3] N. Guo and M. C. Leu, “Additive manufacturing: Technology, applications and research needs,” *Front. Mech. Eng.*, vol. 8, no. 3, pp. 215–243, 2013.
- [4] I. Gibson, D. Rosen, and B. Stucker, *Additive manufacturing technologies: 3D printing, rapid prototyping, and direct digital manufacturing*, no. 3. Springer-Verlag New York, 2014.
- [5] W. Gao et al., “The status, challenges, and future of additive manufacturing in engineering,” *Comput. Des.*, 2015.
- [6] M. Niinomi, T. Narushima, and M. Nakai, *Advances in Metallic Biomaterials, Processing and Applications*, vol. 3. Springer Berlin Heidelberg, 2015.
- [7] A. Rajpura, D. Kendoff, and T. N. Board, “The current state of bearing surfaces in total hip replacement,” *Bone Jt. J.*, vol. 96–B, no. 2, pp. 147–156, 2014.
- [8] Q. Chen and G. A. Thouas, “Metallic implant biomaterials,” *Mater. Sci. Eng. R Reports*, vol. 87, pp. 1–57, 2015.
- [9] R. Huiskes, H. Weinans, and B. van Rietbergen, “The relationship between stress shielding and bone resorption around total hip stems and the effects of flexible materials,” *Clin. Orthop. Relat. Res.*, no. 274, pp. 124–134, 1992.
- [10] H. M. Frost, “Skeletal structural adaptations to mechanical usage (SATMU): 1. Redefining Wolff’s law: The bone modelling problem,” *Anat. Rec.*, vol. 226, no. 4, pp. 423–432, 1990.
- [11] H. Attar et al., “Mechanical behavior of porous commercially pure Ti and Ti-TiB composite materials manufactured by selective laser melting,” *Mater. Sci. Eng. A*, vol. 625, pp. 350–356, 2015.
- [12] H. Attar, M. Bönisch, M. Calin, L. C. Zhang, S. Scudino, and J. Eckert, “Selective laser melting of in situ titanium-titanium boride composites: Processing, microstructure and mechanical properties,” *Acta Mater.*, vol. 76, pp. 13–22, 2014.

- [13] I. V. Okulov et al., “Composition optimization of low modulus and high-strength TiNb-based alloys for biomedical applications,” *J. Mech. Behav. Biomed. Mater.*, vol. 65, no. May 2016, pp. 866–871, 2017.
- [14] B. R. Levine and D. W. Fabi, “Porous metals in orthopedic applications - A review.,” *Mater. Wiss. und Werkstofftechnik*, vol. 41, no. 12, pp. 1001–1010, 2010.
- [15] J. Van Der Stok et al., “Selective laser melting-produced porous titanium scaffolds regenerate bone in critical size cortical bone defects,” *J. Orthop. Res.*, vol. 31, no. 5, pp. 792–799, 2013.
- [16] H. A. Bothe, R. T., Beaton, L. E., and Davenport, “Reaction of bone to multiple metallic implants,” *Surgery, Gynecol. Obstet.*, vol. 71, p. 598, 1940.
- [17] G. S. (1951) Leventhal, “Titanium, a Metal for Surgery,” *J. Bone Jt. Surg.*, vol. 33A, pp. 473–474, 1951.
- [18] O. L. A. Harrysson, O. Cansizoglu, D. J. Marcellin-Little, D. R. Cormier, and H. A. West, “Direct metal fabrication of titanium implants with tailored materials and mechanical properties using electron beam melting technology,” *Mater. Sci. Eng. C*, vol. 28, no. 3, pp. 366–373, 2008.
- [19] L. E. Murr, S. M. Gaytan, E. Martinez, F. Medina, and R. B. Wicker, “Next generation orthopaedic implants by additive manufacturing using electron beam melting,” *Int. J. Biomater.*, vol. 2012, no. February 2017, p. 245727, 2012.
- [20] S. Bose, S. Vahabzadeh, and A. Bandyopadhyay, “Bone tissue engineering using 3D printing,” *Mater. Today*, vol. 16, no. 12, pp. 496–504, 2013.
- [21] A. Gupta and M. Talha, “Recent development in modeling and analysis of functionally graded materials and structures,” *Prog. Aerosp. Sci.*, vol. 79, pp. 1–14, 2015.
- [22] K. Shah, I. ul Haq, A. Khan, S. A. Shah, M. Khan, and A. J. Pinkerton, “Parametric study of development of Inconel-steel functionally graded materials by laser direct metal deposition,” *Mater. Des.*, vol. 54, pp. 531–538, 2014.
- [23] L. Hao and R. Harris, “Customised implants for bone replacement and growth,” in *Bio-Materials and Prototyping Applications in Medicine*, 2008, pp. 79–107.
- [24] W. Pompe et al., “Functionally graded materials for biomedical applications,” *Mater. Sci. Eng. A*, vol. 362, no. 1–2, pp. 40–60, 2003.
- [25] A. Sola, D. Bellucci, and V. Cannillo, “Functionally graded materials for orthopedic applications-an update on design and manufacturing,” *Biotechnol. Adv.*, vol. 34, no. 5, pp. 504–531, 2016.
- [26] S. Park, D. W. Rosen, and C. E. Duty, “Comparing mechanical and geometrical properties of lattice structure fabricated using Electron Beam Melting,” *Solid Free. Fabr. Proc.*, vol. 1, pp. 1359–1370, 2015.
- [27] M. G. Rashed, M. Ashraf, R. A. W. Mines, and P. J. Hazell, “Metallic microlattice materials: A current state of the art on manufacturing, mechanical properties and applications,” *Mater. Des.*, vol. 95, no. April, pp. 518–533, 2016.

- [28] X. P. Tan, Y. J. Tan, C. S. L. Chow, S. B. Tor, and W. Y. Yeong, “Metallic powder-bed based 3D printing of cellular scaffolds for orthopaedic implants : A state-of-the-art review on manufacturing , topological design , mechanical properties and biocompatibility,” *Mater. Sci. Eng. C*, vol. 76, pp. 1328–1343, 2017.
- [29] O. Cansizoglu, D. Cormier, O. Harrysson, H. West, and T. Mahale, “An evaluation of non-stochastic lattice structures fabricated via electron beam melting .,” pp. 209–219, 2006.
- [30] T. G. Chu and J. W. Halloran, “An image-based approach for designing and manufacturing craniofacial scaffolds,” *Int. J. Oral Maxillofac. Surg.*, vol. 29, no. 1, pp. 67–71, 2000.
- [31] S. M. Giannitelli, D. Accoto, M. Trombetta, and A. Rainer, “Current trends in the design of scaffolds for computer-aided tissue engineering,” *Acta Biomater.*, vol. 10, no. 2, pp. 580–594, 2014.
- [32] X. Huang, A. Radman, and Y. M. Xie, “Topological design of microstructures of cellular materials for maximum bulk or shear modulus,” *Comput. Mater. Sci.*, vol. 50, no. 6, pp. 1861–1870, 2011.
- [33] X. Wang et al., “Topological design and additive manufacturing of porous metals for bone scaffolds and orthopaedic implants: A review,” *Biomaterials*, vol. 83, no. September, pp. 127–141, 2016.
- [34] F. S. L. Bobbert et al., “Additively manufactured metallic porous biomaterials based on minimal surfaces : A unique combination of topological , mechanical , and mass transport properties,” *Acta Biomater.*, vol. 53, pp. 572–584, 2017.
- [35] L. Hao, D. Raymont, C. Yan, A. Hussein, and P. Young, “Design and additive manufacturing of cellular lattice structures,” *Innov. Dev. Virtual Phys. Prototyp.*, no. November 2014, pp. 249–254, 2011.
- [36] C. Lin, C. Hsiao, P. Chen, and S. J. Hollister, “Interbody fusion cage design using integrated global layout and local microstructure topology optimization,” vol. 29, no. 16, pp. 1747–1754, 2004.
- [37] S. J. Li et al., “Influence of cell shape on mechanical properties of Ti-6Al-4V meshes fabricated by electron beam melting method,” *Acta Biomater.*, vol. 10, no. 10, pp. 4537–4547, 2014.
- [38] Y. Wang, Z. Luo, N. Zhang, and Q. Qin, “Topological shape optimization of multifunctional tissue engineering scaffolds with level set method,” pp. 333–347, 2016.
- [39] G. Ryan, A. Pandit, and D. P. Apatsidis, “Fabrication methods of porous metals for use in orthopaedic applications,” *Biomaterials*, vol. 27, no. 13, pp. 2651–2670, 2006.
- [40] Y. Chen et al., “Mechanical properties and biocompatibility of porous titanium scaffolds for bone tissue engineering,” *J. Mech. Behav. Biomed. Mater.*, vol. 75, no. May, pp. 169–174, 2017.

- [41] Y. W. Gu, M. S. Yong, B. Y. Tay, and C. S. Lim, "Synthesis and bioactivity of porous Ti alloy prepared by foaming with TiH₂," *Mater. Sci. Eng. C*, vol. 29, no. 5, pp. 1515–1520, 2009.
- [42] M. Bram, C. Stiller, H. P. Buchkremer, D. Stöver, and H. Baur, "High-porosity titanium, stainless Steel, and superalloy parts," *Adv. Eng. Mater.*, vol. 2, no. 4, pp. 196–199, 2000.
- [43] X. Deng, Y. Wang, J. Yan, T. Liu, and S. Wang, "Topology optimization of total femur structure: application of parameterized Level set method under geometric constraints," *J. Mech. Des.*, vol. 138, no. 1, p. 11402, 2015.
- [44] M. Das, V. K. Balla, T. S. S. Kumar, and I. Manna, "Fabrication of biomedical implants using laser engineered net shaping (LENSTM)," *Trans. Indian Ceram. Soc.*, vol. 72, no. 3, pp. 169–174, 2013.
- [45] L. E. Murr, "Additive manufacturing of biomedical devices: an overview," *Mater. Technol.*, vol. 33, no. 1, pp. 57–70, 2018.
- [46] X. Zhao et al., "Comparison of the microstructures and mechanical properties of Ti–6Al–4V fabricated by selective laser melting and electron beam melting," *Jmade*, vol. 95, no. April, pp. 21–31, 2015.
- [47] H. Attar, S. Ehtemam-Haghighi, D. Kent, X. Wu, and M. S. Dargusch, "Comparative study of commercially pure titanium produced by laser engineered net shaping, selective laser melting and casting processes," *Mater. Sci. Eng. A*, vol. 705, no. August, pp. 385–393, 2017.
- [48] E. Sallica-Leva, A. L. Jardini, and J. B. Fogagnolo, "Microstructure and mechanical behavior of porous Ti-6Al-4V parts obtained by selective laser melting," *J. Mech. Behav. Biomed. Mater.*, vol. 26, pp. 98–108, 2013.
- [49] Z. A. Ahmadi SM, Hedayati R, Jain RA, Li Y, Leeflang S, "Effects of laser processing parameters on the mechanical properties, topology, and microstructure of additively manufactured porous metallic biomaterials: A vector-based approach," *Mater. Des.*, vol. 134, pp. 234–243, 2017.
- [50] R. Wauthle et al., "Effects of build orientation and heat treatment on the microstructure and mechanical properties of selective laser melted Ti6Al4V lattice structures," *Addit. Manuf.*, vol. 5, no. May, pp. 77–84, Jan. 2015.
- [51] S. L. Sing, W. Y. Yeong, F. E. Wiria, and B. Y. Tay, "Characterization of titanium lattice structures fabricated by selective laser melting using an adapted compressive test method," *Exp. Mech.*, vol. 56, no. 5, pp. 735–748, 2016.
- [52] S. L. Sing, F. E. Wiria, and W. Y. Yeong, "Selective laser melting of lattice structures: A statistical approach to manufacturability and mechanical behavior," *Robot. Comput. Integr. Manuf.*, vol. 49, no. January 2017, pp. 170–180, 2018.
- [53] S. L. Sing, Y. Miao, F. E. Wiria, and W. Y. Yeong, "Manufacturability and mechanical testing considerations of metallic scaffolds fabricated using selective laser melting: a review," *Biomed. Sci. Eng.*, vol. 1, no. 1, 2016.

- [54] L. E. Murr et al., “Characterization of Ti-6Al-4V open cellular foams fabricated by additive manufacturing using electron beam melting,” *Mater. Sci. Eng. A*, vol. 527, no. 7–8, pp. 1861–1868, 2010.
- [55] J. Karlsson et al., “Thickness dependency of mechanical properties for thin-walled titanium parts manufactured by Electron Beam Melting (EBM),” *Addit. Manuf.*, vol. 12, pp. 45–50, 2016.
- [56] W. R. Cheng XY, Li SJ, Murr LE, Zhang ZB, Hao YL, Yang R, Medina F, “Compression deformation behavior of Ti-6Al-4V alloy with cellular structures fabricated by electron beam melting,” *J. Mech. Behav. Biomed. Mater.*, no. 16, pp. 153–162, 2012.
- [57] O. Cansizoglu, O. Harrysson, D. Cormier, H. West, and T. Mahale, “Properties of Ti-6Al-4V non-stochastic lattice structures fabricated via electron beam melting,” *Mater. Sci. Eng. A*, vol. 492, no. 1–2, pp. 468–474, 2008.
- [58] A. M. F. Ashby, “The Properties of Foams and Lattices,” *Philos. Trans. R. Soc. A Math. Phys. Eng. Sci.*, vol. 364, no. 1838, pp. 15–30, 2005.
- [59] S. M. Ahmadi et al., “Additively manufactured open-cell porous biomaterials made from six different space-filling unit cells: The mechanical and morphological properties,” *Materials (Basel)*, vol. 8, no. 4, pp. 1871–1896, 2015.
- [60] A. Yáñez, A. Herrera, O. Martel, D. Monopoli, and H. Afonso, “Compressive behaviour of gyroid lattice structures for human cancellous bone implant applications,” *Mater. Sci. Eng. C*, vol. 68, pp. 445–448, 2016.
- [61] S. Amin Yavari et al., “Fatigue behavior of porous biomaterials manufactured using selective laser melting,” *Mater. Sci. Eng. C*, vol. 33, no. 8, pp. 4849–4858, 2013.
- [62] N. W. Hrabe, P. Heintl, B. Flinn, C. Ko, and R. K. Bordia, “Compression-compression fatigue of selective electron beam melted cellular titanium (Ti-6Al-4V),” *J. Biomed. Mater. Res. Part B Appl. Biomater.*, vol. 99, no. 2, pp. 313–320, 2011.
- [63] S. Amin Yavari et al., “Relationship between unit cell type and porosity and the fatigue behavior of selective laser melted meta-biomaterials,” *J. Mech. Behav. Biomed. Mater.*, vol. 43, no. January, pp. 91–100, 2015.
- [64] X. Zhang, G. Fang, and J. Zhou, “Additively manufactured scaffolds for bone tissue engineering and the prediction of their mechanical,” *Materials (Basel)*, vol. 10, no. 50, 2017.
- [65] J. Parthasarathy, B. Starly, S. Raman, and A. Christensen, “Mechanical evaluation of porous titanium (Ti6Al4V) structures with electron beam melting (EBM),” *J. Mech. Behav. Biomed. Mater.*, vol. 3, no. 3, pp. 249–259, 2010.
- [66] R. Wauthle et al., “Revival of pure titanium for dynamically loaded porous implants using additive manufacturing,” *Mater. Sci. Eng. C*, vol. 54, no. May 2016, pp. 94–100, 2015.
- [67] M. Speirs, B. Van Hooreweder, J. Van Humbeeck, and J.-P. Kruth, “Fatigue behaviour of NiTi shape memory alloy scaffolds produced by SLM, a unit cell design

comparison,” *J. Mech. Behav. Biomed. Mater.*, vol. 70, no. October 2016, pp. 53–59, Jun. 2017.

[68] C. Yan, L. Hao, A. Hussein, and P. Young, “Ti – 6Al – 4V triply periodic minimal surface structures for bone implants fabricated via selective laser melting,” *J. Mech. Behav. Biomed. Mater.*, vol. 51, pp. 61–73, 2015.

[69] R. A. W. Mines, Y. Shen, W. J. Cantwell, W. Brooks, and C. J. Sutcliffe, “The influence of processing parameters on the mechanical properties of selectively laser melted stainless steel microlattice structures,” *J. Manuf. Sci. Eng. Copyr.*, vol. 132, pp. 1–12, 2010.

[70] W. Mines, “Compressive behaviour of stainless steel micro-lattice structures,” *Int. J. Mech. Sci.*, vol. 68, pp. 125–139, 2013.

[71] M. Smith, Z. Guan, and W. J. Cantwell, “Finite element modelling of the compressive response of lattice structures manufactured using the selective laser melting technique,” *Int. J. Mech. Sci.*, vol. 67, pp. 28–41, 2013.

[72] F. J. Quevedo González and N. Nuño, “Finite element modelling approaches for well-ordered porous metallic materials for orthopaedic applications: cost effectiveness and geometrical considerations,” *Comput. Methods Biomech. Biomed. Engin.*, vol. 19, no. 8, pp. 845–854, 2016.

[73] Q. P. Zhao Dong, Wei Chen, Hujun Bao, Hongxin Zhang, “Real-time voxelization for complex models,” in *Computer Graphics and Applications Proceedings. 12th Pacific Conference on. IEEE, 200AD.*

[74] M. Dumas, P. Terriault, and V. Brailovski, “Modelling and characterization of a porosity graded lattice structure for additively manufactured biomaterials,” *Mater. Des.*, 2017.

[75] K. Li, X. Gao, and G. Subhash, “Effects of cell shape and strut cross-sectional area variations on the elastic properties of three-dimensional open-cell foams,” vol. 54, pp. 783–806, 2006.

[76] A. Herrera, A. Yáñez, O. Martel, H. Afonso, and D. Monopoli, “Computational study and experimental validation of porous structures fabricated by electron beam melting: A challenge to avoid stress shielding,” *Mater. Sci. Eng. C*, vol. 45, pp. 89–93, 2014.

[77] F. J. Q. González and N. Nuño, “Finite element modeling of manufacturing irregularities of porous materials,” *Biomater. Biomech. Bioeng.*, vol. 3, no. 1, pp. 1–14, 2016.

[78] V. Crupi, E. Kara, G. Epasto, E. Guglielmino, and H. Aykul, “Static behavior of lattice structures produced via direct metal laser sintering technology,” *Mater. Des.*, 2017.

[79] J. Kadkhodapour et al., “Failure mechanisms of additively manufactured porous biomaterials: Effects of porosity and type of unit cell,” *J. Mech. Behav. Biomed. Mater.*, vol. 50, no. October, pp. 180–191, 2015.

- [80] G. Campoli et al., “Mechanical properties of open-cell metallic biomaterials manufactured using additive manufacturing,” *Mater. Des.*, vol. 49, no. August 2013, pp. 957–965, 2013.
- [81] J. Kadkhodapour, H. Montazerian, A. C. Darabi, A. Zargarian, and S. Schmauder, “The relationships between deformation mechanisms and mechanical properties of additively manufactured porous biomaterials,” *J. Mech. Behav. Biomed. Mater.*, vol. 70, pp. 28–42, 2016.
- [82] E. T. A. Rasheedat Modupe Mahamood, S. Tammas-Williams, and I. Todd, *Functionally Graded Materials*. Springer, 2016.
- [83] R. P. Eujin Pei, Giselle Hsiang Loh, David Harrison, Henrique de Amorim Almeida, Mario Domingo Monzón Verona, “Exploring the concept of functionally graded additive manufacturing,” *Assem. Autom.*, vol. 37, no. 2, pp. 147–153, 2017.
- [84] R. Roop Kumar and M. Wang, “Functionally graded bioactive coatings of hydroxyapatite/titanium oxide composite system,” *Mater. Lett.*, vol. 55, no. 3, pp. 133–137, 2002.
- [85] R. M. Mahamood, E. T. Akinlabi, M. Shukla, and S. Pityana, “Functionally graded material: an overview,” *Proc. World Congr. Eng. WCE 2012*, vol. III, pp. 2–6, 2012.
- [86] B. Kieback, A. Neubrand, and H. Riedel, “Processing techniques for functionally graded materials,” *Mater. Sci. Eng. A*, vol. 362, no. 1–2, pp. 81–105, 2003.
- [87] Y. Watanabe, oshifumi Inaguma, H. Sato, and E. Miura-Fujiwara, “A novel fabrication method for functionally graded materials under centrifugal force: The centrifugal mixed-powder method,” *Materials (Basel)*, vol. 2, no. 4, pp. 2510–2525, 2009.
- [88] A. Boccaccio, A. E. Uva, M. Fiorentino, G. Mori, and G. Monno, “Geometry design optimization of functionally graded scaffolds for bone tissue engineering: A mechanobiological approach,” *PLoS One*, vol. 11, no. 1, 2016.
- [89] S. L. Sing, J. An, W. Y. Yeong, and F. E. Wiria, “Laser and electron-beam powder-bed additive manufacturing of metallic implants: A review on processes, materials and designs,” *J. Orthop. Res.*, vol. 34, no. 3, pp. 369–385, 2016.
- [90] B. V. Krishna, S. Bose, and A. Bandyopadhyay, “Low stiffness porous Ti structures for load-bearing implants,” *Acta Biomater.*, vol. 3, no. 6, pp. 997–1006, 2007.
- [91] J. Choy, S. Y., Sun, C. N., Leong, K. F., Tan, K. E., & Wei, “Functionally graded material by additive manufacturing,” in *Proceedings of the 2nd International Conference on Progress in Additive Manufacturing (Pro-)*, 2016, pp. 206–211.
- [92] V. A. Popovich, E. V. Borisov, A. A. Popovich, V. S. Sufiiarov, D. V. Masaylo, and L. Alzine, “Functionally graded Inconel 718 processed by additive manufacturing: Crystallographic texture, anisotropy of microstructure and mechanical properties,” *Mater. Des.*, vol. 114, pp. 441–449, 2016.
- [93] P. Popoola, G. Farotade, O. Fatoba, and O. Popoola, “Laser engineering net shaping method in the area of development of functionally graded materials (FGMs) for aero engine applications - a review,” in *Fiber Laser*, 2016, pp. 383–399.

- [94] R. Gabbrielli, I. Turner, and C. R. Bowen, "Development of modelling methods for materials to be used as bone substitutes," *Key Eng. Mater.* Vol. 361. Trans Tech Publ. 2008., vol. 361, pp. 903–906, 2008.
- [95] R. Gabbrielli et al., "Design of a graded cellular structure for an acetabular hip replacement component," *Biofabrication*, vol. 6, no. 4, p. 45007, 2006.
- [96] F. A. España, V. K. Balla, S. Bose, and A. Bandyopadhyay, "Design and fabrication of CoCrMo alloy based novel structures for load bearing implants using laser engineered net shaping," *Mater. Sci. Eng. C*, vol. 30, no. 1, pp. 50–57, 2010.
- [97] K. B. Hazlehurst, C. J. Wang, and M. Stanford, "The potential application of a Cobalt Chrome Molybdenum femoral stem with functionally graded orthotropic structures manufactured using Laser Melting technologies," *Med. Hypotheses*, vol. 81, no. 6, pp. 1096–1099, 2013.
- [98] K. B. Hazlehurst, C. J. Wang, and M. Stanford, "An investigation into the flexural characteristics of functionally graded cobalt chrome femoral stems manufactured using selective laser melting," *Mater. Des.*, vol. 60, no. 4, pp. 177–183, 2014.
- [99] S. Limmahakhun, A. Oloyede, and N. Chantarapanich, "Alternative designs of load – sharing cobalt chromium graded femoral stems," *Mater. Today Commun.*, vol. 12, no. May, pp. 1–10, 2017.
- [100] Fernando José Quevedo González, "Computational design of functionally graded hip implants by means of additively manufactured porous materials," *École de technologie supérieure*, 2016.
- [101] S. Arabnejad and D. Pasini, "Multiscale Design and Multiobjective Optimization of Orthopedic Hip Implants with Functionally Graded Cellular Material," *J. Biomech. Eng.*, vol. 134, no. 3, p. 31004, 2012.
- [102] S. Arabnejad, B. Johnston, M. Tanzer, and D. Pasini, "Fully porous 3D printed titanium femoral stem to reduce stress-shielding following total hip arthroplasty," *J. Orthop. Res.*, vol. 35, no. 8, pp. 29–31, 2016.
- [103] S. Arabnejad and D. Pasini, "Fatigue design of a mechanically biocompatible lattice for a proof-of-concept femoral stem," *J. Mech. Behav. Biomed. Mater.*, vol. 22, pp. 65–83, 2013.
- [104] A. Oshkour, N. Abu Osman, Y. Yau, F. Tarlochan, and W. Wan Abas, "Design of new generation femoral prostheses using functionally graded materials : A finite element analysis," vol. 227, no. 1, pp. 3–17, 2012.
- [105] A. Oshkour et al., "Finite element analysis on longitudinal and radial functionally graded femoral prosthesis," *Int. j. numer. method. biomed. eng.*, vol. 29, no. 1, pp. 1412–1427, 2013.
- [106] H. S. Hedia, M. A. N. Shabara, T. T. El-Midany, and N. Fouda, "A method of material optimization of cementless stem through functionally graded material," *Int. J. Mech. Mater. Des.*, vol. 1, no. 4, pp. 329–346, 2005.

[107] F. F. Al-Jassir, H. Fouad, and O. Y. Alothman, "In vitro assessment of Function Graded (FG) artificial Hip joint stem in terms of bone/cement stresses: 3D Finite Element (FE) study," *Biomed. Eng. Online*, vol. 12, no. 1, p. 5, 2013.

[108] M. Bahraminasab, B. B. Sahari, K. L. Edwards, F. Farahmand, T. S. Hong, and H. Naghibi, "Material tailoring of the femoral component in a total knee replacement to reduce the problem of aseptic loosening," *Mater. Des.*, vol. 52, pp. 441–451, 2013.

Chapter 3

Selective Laser Melting of Porosity Graded Lattice Structures for Bone Implants

Complete Citation:

Mahmoud, Dalia, and M. A. Elbestawi. "Selective laser melting of porosity graded lattice structures for bone implants." *The International Journal of Advanced Manufacturing Technology* 100.9-12 (2019): 2915-2927. <https://doi.org/10.1007/s00170-018-2886-9>

Copyright:

Reprinted with permission copyrighted by Springer Nature, 2017.

Relative Contributions:

Dalia Mahmoud: Performed experiments, analysis, and data interpretation. Wrote the first draft of the manuscript.

M. A. Elbestawi: Revised and edited the manuscript.

Abstract:

Porosity graded lattice structures are used in bone implants to mimic natural bone properties. Rather than having uniform pore size distribution, the size distribution is gradually changed in a certain direction to achieve specific mechanical and biological properties. Selective laser melting (SLM) has been used to print uniform metallic lattice structures with high accuracy. However, the accuracy of SLM in printing lattice structures with a wide range of pore sizes and volume fractions needs to be defined. The effect of SLM process scanning strategies on morphological properties of graded porosity metallic lattice structures is investigated in this study. Three different scanning strategies are proposed, and their effect on volume fraction, strut size, and surface integrity is investigated. Characterization of the printed parts reveals that the effect of different scanning strategies on the morphological quality is highly dependent on the design volume fraction for the chosen unit cell design. It was noted that using hatching strategies results in better dimensional accuracy and surface integrity in high volume fraction lattice structures. While the use of total fill scanning strategy resulted in significantly distorted geometries in high volume fractions. However, in lower volume fractions the dimensional accuracy as well as the surface integrity is comparable to that of hatching strategies. This work highlights the importance of understanding the limitations and capabilities of the SLM process in this application, and to enhance the printing quality of porosity graded metallic lattice structures.

Keywords:

Selective laser melting; Porosity graded lattice structures; Gyroids; Dimensional accuracy; Surface integrity.

Acknowledgment:

We acknowledge the support of the Natural Sciences and Engineering Research Council of Canada (NSERC), [funding reference number 518494].

3.1 Introduction

Additive manufacturing (AM) technology is capable of printing customized biomedical implants, precisely tailored to the anatomy of each patient. Compared to other implant manufacturing methods, AM can print implants with lower costs, less material waste and shorter times [1], [2]. Another important advantage besides customization is its ability to print implants from lattice structures instead of bulk/solid parts. The use of lattice structures in orthopedic implants accomplishes two important functional enhancements to the implants. The first is that lattice structures reduces the stiffness of the implant, therefore avoiding the stress shielding phenomena [3]. The second is that the presence of interconnected pore structure in the contact surface between the implant and the bone facilitate the bone tissue growth [4]. Selective Laser Melting (SLM), is an AM technology that is widely used for printing metallic parts, reaching an accuracy of 0.2 mm or less [5]. This has made it one of the most suitable techniques for printing lattice structures used for bone implants.

Porosity graded lattice structures can be designed using computer aided design (CAD) software or based on implicit equations [6]. Implicit equations are used to create triply periodic minimal surfaces (TPMS) unit cells [7], which are known for their biomorphic design, high surface area to volume ratio, interconnected pore channels, high permeability, and adequate mechanical integrity [8]. Furthermore, TPMS unit cells are considered self-supporting structures and therefore are well suited to be manufactured by SLM. Compared to CAD based designs the implicit based unit cells can be manufactured with fewer defects [9]. These types of unit cells are also known for their ability to be designed in a continuous

porosity gradation in contrast to the discontinuity between layers resulting from CAD unit cells.

Lattice structures are formed from repetitive unit cells. The amount of porosity in these unit cells affect the mechanical and biological properties of lattice structures [10]. Large pore size (high porosity) allows more flow of nutrients and therefore enhances tissue growth [11]. However, this affects the mechanical properties of the lattice structure, and may become inadequate for bone implant applications [12]. To avoid this tradeoff between mechanical and biological properties, porosity graded lattice structures represent a good alternative. The mechanical properties of linear porosity graded lattice structures shows better mechanical properties than uniform ones [13], [14]. Onal et al. [15] tailored the porosity in the linear direction to obtain mirror like structures with porosity increasing towards the center and vice versa. The authors suggested that the most suitable design would have high porosity on the outer volumes to enhance biological properties and prevent cell occlusions. Their results proved that small porosity in the inner volumes would enhance the mechanical integrity of the structures.

Although experimental results are promising, improper choice of SLM process parameters can lead to inconsistency and low repeatability. Investigating the effect of process parameters on the quality of printed lattice structures is required to optimize them. Few studies address the effects of SLM process parameters on the dimensional accuracy of lattice structures, and these studies primarily focused on uniform CAD based lattice structures. A statistical approach to determine the manufacturability of Ti6Al4V CAD-based lattice structure was performed by Sing et al. [16], [17], where the laser power was found to be the most significant parameter influencing dimensional accuracy and mechanical properties. Ahmadi et al. [18] studied the effect of laser power and exposure

time on the dimensional and mechanical properties of CAD based lattice structures. It was found that for the intervals used in their study, increasing the laser power and exposure time, increases the strut size and relative density of lattice structure. Therefore, the mechanical properties improve as well. The highest laser power used was 128 W, although higher laser powers can be used with Ti6Al4V.

The laser beam scan path can be varied in SLM process, as the laser path changes the thermal distribution and thermal history also changes. This leads to change in powder melting and solidification rates and thus affects the morphological and mechanical properties of printed parts [19]. The effect of scanning strategy on the quality of lattice structures is usually overlooked. Ghose et al. [20] studied the influence of SLM scanning strategies and process parameters on stochastic lattice structures. Three scanning strategies were investigated: contouring, point and pulsing strategies. The authors observed that those scanning strategies had no major effect on the strut thickness. It is assumed that changing the unit cell design (geometry) will change the effect of scanning strategies on the strut morphology.

Most of the afore-mentioned results targeted either CAD-based lattice structures or uniform graded ones. The lack of knowledge and understanding about TPMS lattice structures design, makes it less understood than CAD based lattice structures. Therefore, this study aims to investigate the manufacturability of porosity graded TPMS lattice structures. First the design space of one type of TPMS unit cells is investigated, relating the biological needs for bone implants and SLM capabilities with the unit cell's morphology. Then the effect of scanning strategy on the morphology of graded lattice structures is investigated. The density, dimensional accuracy, and surface integrity are examined, since they are the

main contributing factors that affect lattice structures' mechanical and biological properties for bone implants.

3.2 Design of porosity graded lattice structures

Gyroids are one type of TPMS that have been studied extensively over the past decade. Compared to other TPMS unit cells, gyroids are known for their comparatively good mechanical and biological properties [21], [22]. Gyroid surface can be defined by the parametric equation:

$$G = \cos\left(\frac{2\pi}{L} \cdot x\right) \sin\left(\frac{2\pi}{L} \cdot y\right) + \cos\left(\frac{2\pi}{L} \cdot y\right) \sin\left(\frac{2\pi}{L} \cdot z\right) + \cos\left(\frac{2\pi}{L} \cdot z\right) \sin\left(\frac{2\pi}{L} \cdot x\right) - t = 0 \quad \text{Equation 3-1}$$

Where “L” is the size of each unit cell as shown in **Figure 3-1**, “t” is the “level constant” that controls the volume fraction of each unit cell. Volume fraction is the ratio between the volume of material and volume of the unit cell (L^3). Like sine and cosines waves, the gyroid surface has a period that could be scaled to control the lattice size and number of pores. By changing the value of “t”, the volume fraction of each unit cell changes as well.

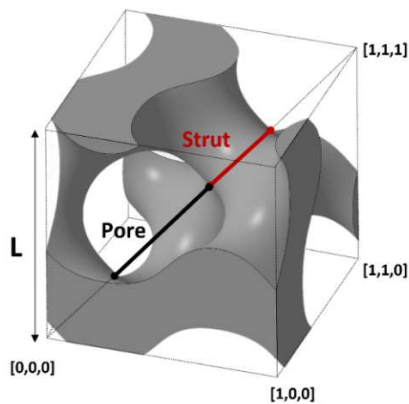


Figure 3-1: Morphology of a single gyroid unit cell

The mathematical equation provide insight into the morphology of gyroids which allows for better understanding of gyroid lattice structures. The relationship between the equation inputs: “t” and “L”, and the gyroid lattice outputs: volume fraction, strut size and pore size were investigated. A MATLAB[®] code was written to create gyroid lattice structures in STL (stereolithography) format. Then the file was imported to Netfabb[®], for post-processing and measurements. Thirty single unit cells were created at different values of “t”, the volume fraction relationship with “t” is plotted in Fig. 2(a). As the value of “t” increases the volume fraction increases as well. When $t=0$, the gyroid surface divides the space into two equal domains, thus the unit cell would have a volume fraction of 50%. For “t” values greater than 1.5 the unit cell turns into solid, while for values of “t” below -1.5 the gyroid equation does not exist.

The strut and pore sizes are also measured using Netfabb[®], the strut size of the gyroid would differ in each location. Therefore, all the measurements were taken at the intersection between a vector in the direction of [111] and the gyroid unit cell as explain by Walker et al. [23]. As illustrated by Fig. 2 (b), as the value of “t” increases the volume fraction increases, the pore size increases, and the strut size decreases. As the equations for regression were obtained, the morphology (i.e. volume fraction, strut size, and pore size) can be determined using two input parameters “t, L”.

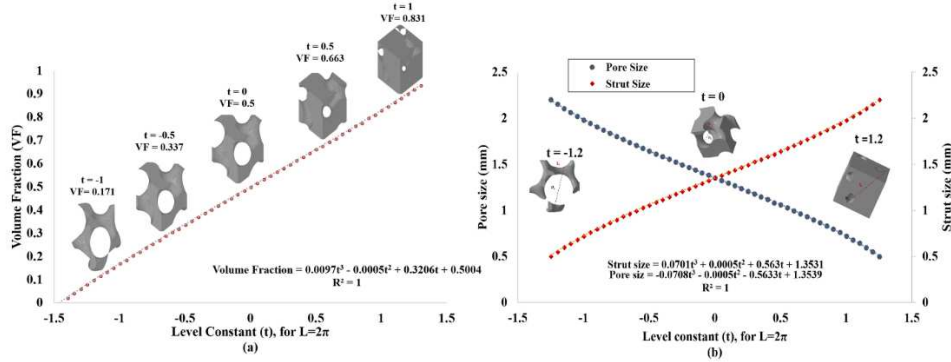


Figure 3-2: (a) Volume fraction, (b) strut and pore size as a function of level constant (t) for gyroid unit cell

Volume fraction, pore size and strut thickness play an important role to define the bone cell attachment to the bone implant. Therefore, the permissibility design space would vary from one unit cell to the other [23]. The minimum strut thickness to be manufactured using SLM can be defined by 0.2 mm [24]. The bone volume to total volume (volume fraction) of trabecular bone is in the range of 5% to 60% (95%-40% porosity), while that of cortical bone is 85%-95% (5%-15% porosity). The morphological requirements for trabecular and cortical bone differ according to the region of the body [25], for example the average pore size for trabecular bone in a femoral head is in the range of 0.456-0.982 mm, while that of the vertebrae is around 0.922 mm. For bone growth requirement porosity higher than 50% is essential, and pore size between 0.609-0.110 mm is needed [26], [27].

illustrates the permissible design space for gyroid unit cells. Pore and strut size distributions are plotted in dotted lines for different unit cell sizes. The biological requirements for successful implants are represented in the red lines, while the SLM capabilities is presented in black line. The shaded area represents the allowable design space for gyroid lattice structures for bone implants applications. The map acts as a guide to determine the gyroid's morphological outputs from the equation inputs (t, L). It

facilitates the choice of the correct parameters to match the bone implants' requirements and capabilities of SLM.

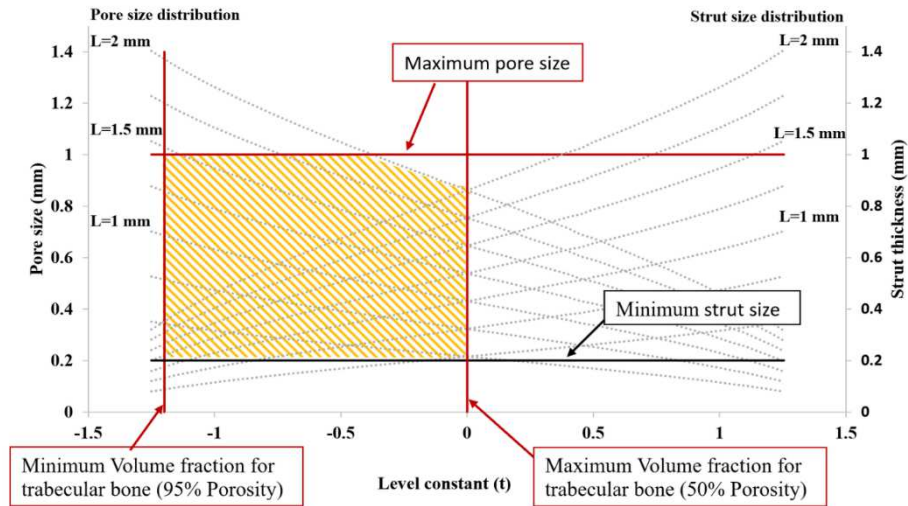


Figure 3-3: Permissibility design space for gyroid unit cell

3.3 Experimental work

3.3.1 Materials and methods

The porosity graded gyroids (PGGs) printed in this study were obtained using the gyroid equations. By replacing the constant value of “ t ” to a linear function, the porosity gradation/change in volume fraction design is displayed in Fig. 4. By setting the value of L to 1 mm and using boundary limits $(-0.5\pi$ to $9.5\pi)$, $10 \times 10 \times 10$ mm cubes were created in a stereolithography “STL” format. A solid base layer of 5 mm was added to the part, to facilitate adhesion and removal from the build plate. One major advantage of that type of structure is that the change in the geometry is continuous. Therefore, no sudden interruptions between layers occur, ensuring a continuous change between layers.

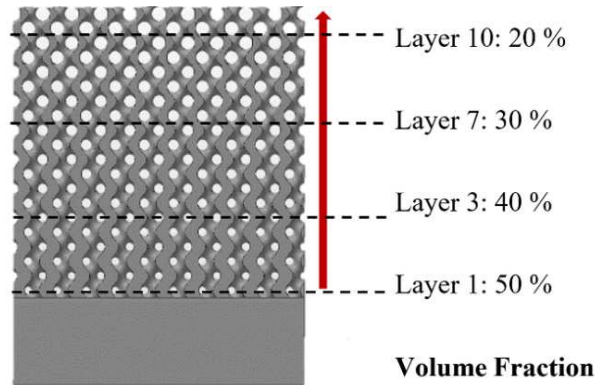


Figure 3-4: Porosity graded gyroids (PGGs)

A Renishaw AM400 machine (Renishaw Solution center, Kitchener, Ontario, Canada) equipped with 400 W pulsed fiber laser was used to manufacture the PGGs. Titanium is one of the most common alloys to be used for bone implant applications [28], for this study Ti6Al4V ELI-0406 powder supplied by Renishaw was used. Three PGGs were printed using fixed process parameters, reported in **Table 3-1**. For each PGG a different scanning strategy was used. As built PGGs were ultrasonically cleaned in acetone and ethanol for 10 minutes each. Then compressed air was used to make sure no trapped powder was stuck inside the structures.

Table 3-1: SLM process parameters

Power	200 W
Exposure time	75 μm
Point distance	50 μm
Hatch distance	65 μm
Layer thickness	30 μm
Laser power at boarder	100 W
Contour offset distance	60 μm

3.3.2 Scanning strategies

Three different scanning strategies were investigated: hatching with border (HB), hatching with no borders (HNB), and total fill (TF). Figure 3-5 represents the schematic laser path for each of these strategies. The HNB scan strategy, consists of scanning stripes oriented with 67° in the first layer. The second layer is rotated by 67° relative to the first one to reduce the residual stresses [29]. Residual stresses are caused when high thermal stresses are introduced to the part, while the part volume is not free to expand nor contract [30]. In the HB strategy, the hatching is first scanned by the same strategy as HNB, and at the end one final contour is scanned around the hatches. In TF strategy the layer is printed by making concentric contours of the geometry until the whole part is covered. In this strategy the laser moves from inner contours to outer ones, and there is no rotation between two successive layers.

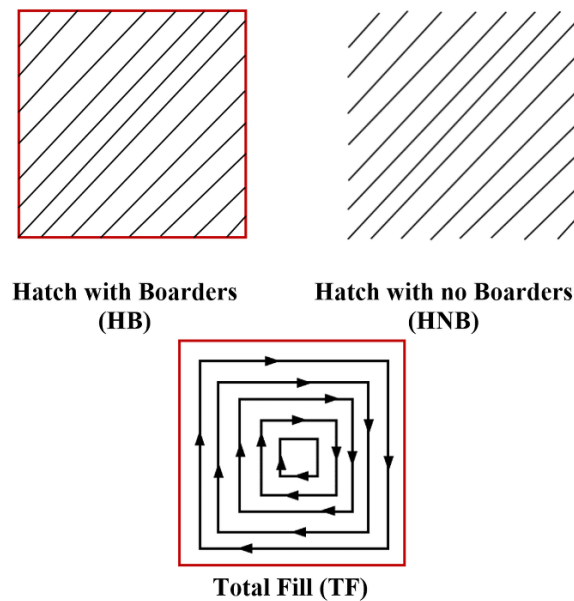


Figure 3-5: SLM scanning strategies used for printing the PGGs

3.3.3 Volume fraction

Four different methods were used to obtain the density of the PGGs: dry weighing, Archimedes principle using water, Archimedes using acetone and micro Computed Tomography (μ CT). Dry weighing simply weighs the part and divides it by its measured volume to obtain the calculated density. The volume fraction is calculated by dividing the calculated density on the theoretical density of the material used [16]. Archimedes principle was also used to determine the density of the porosity graded lattice structures. The weight of each part was measured in the air and water using a digital scale (accuracy of ± 0.01 g), the process was repeated three times for reliability. The relative density was calculated by dividing the calculated density of the lattice structure by the relative density of Ti6Al4V alloy (4.42 g/cm³). Next, acetone was used instead of water, and the whole process was repeated, replacing the density of water by that of acetone. A Bruker SkyScan1172 X-ray tomography scanner was used for quantitative analysis for the printed lattice structures at 100 kV using an Al/Cu filter. The total volume (10 x10 x 10 mm³) of the PGGs was scanned allowing a voxel resolution of 8.4 μ m³. Additionally, the volume fraction of each layer was evaluated using μ CT, by obtaining the ratio between material and voids in each layer.

3.3.4 Dimensional accuracy

The reconstructed scans from the μ CT was used to investigate the dimensional accuracy of the porosity graded lattice structures. Netfabb[®] was used for virtual measurements and post processing of reconstructed scans. Reconstructed strut sizes in different layers were measured and compared to the design values. For consistent results the strut size was measured in the direction of the [111] vector as described by Walker et al. [31]. Five randomly distributed readings were obtained in each layer of measurements to reduce

errors. To obtain a better understanding of the struts variation, mesh comparisons were used to evaluate the overall variation between the design and the as built specimens.

3.3.5 Surface integrity

Due to the relatively small size of the struts and the large amount of partially melted powder, the roughness on some of the internal struts were inaccessible using optical methods. Surface roughness was characterized via stylus profilometry (Surftest Sj-410) on the outer flat surface of the PGGs. Side roughness was measured along the layer's direction, 5 mm of the surface was evaluated. A cut-off wavelength of 0.8 mm was used to determine the arithmetic average roughness "Ra", this value ensured the proper distinguish between wave form roughness and the high frequency ones. Five measurements were taken in each layer to reduce the errors and ensure reliability of results. A scanning electron microscope (SEM) was used to investigate the surface of the printed graded lattice structures.

3.4 Results and discussion

3.4.1 Visual evaluation

The primary focus of this work is to evaluate the effect of scanning strategies on the quality of porosity graded lattice structures. Figure 3-6 represents the macroscopic evaluation of the as built PGGs. The PGG scanned using TF strategy failed in the first 6 layers, since the contours are concentric, contour overlapping may occur increasing the amount of laser input energy delivered to the powder [32]. The PGG scanned with HB strategy had better defined structure than the HNB strategy, this is attributed to the final contour used for enhancing surface finish in this strategy [33]. Overall, the geometry of the pores appeared

to be deviated from the design, and some pores appeared to be clogged. This may indicate that the process parameters chosen need some tuning to obtain more accurate geometry.

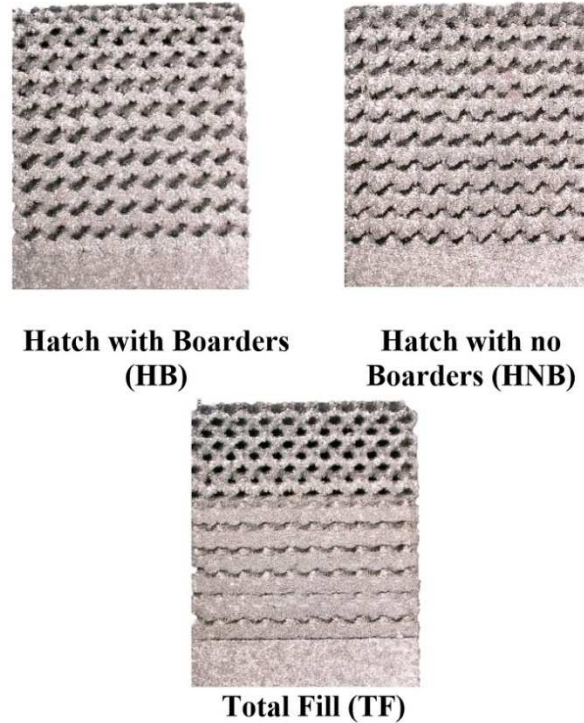


Figure 3-6: Visual evaluation of PGGs

3.4.2 Volume fraction

The deviation in volume fraction using the four measurement methods for the three PGGs is illustrated by **Figure 3-7**, all measurements were found to be greater than the designed volume fraction. Dry weighing overestimated the volume fraction, due to the omission of the internal porosity. This method gives an indication of the general trend of the volume fractions. Using water as a suspension liquid in the Archimedes method, gave an over estimation of the volume fraction as well. This can be attributed to the high surface roughness of the parts. Rough surfaces may lead to the formation of air bubbles and therefore results in inconsistent measurements [34]. Very low deviation between volume

fraction measured using the Archimedes method using acetone and μ CT were observed. These methods were therefore considered more reliable than the other two methods. The variation between the two methods can be related to several factors such as the inability of acetone to penetrate the pores and the rough surface of the struts preventing the liquid to fully fill the voids. The presence of internal voids as well could not be detected using Archimedes methods. Some errors that might occur in μ CT scanning include image thresholding, beam hardening, misalignment errors and limited resolution [35].

Overall, the obtained volume fraction is higher than expected, this suggests that the PGGs are less porous than designed. This agrees with the findings of Ataei et al. [36] and Han et al. [37]. The volume fraction increase is attributed to the errors resulting in the small strut sizes, small pore sizes of the parts, and the partially melted powder to the struts. The PGG scanned by the HB strategy resulted in the least deviation, while the PGG scanned by TF strategy resulted in the largest deviation.

The deviation in volume fraction obtained from μ CT reconstruction for each layer of the PGGs is plotted in Figure 3-8. Visual evaluation of the first 6 layer in the PGG scanned using TF strategy gave the highest deviation. However, after the 6th layer (volume fraction = 30%), the deviation reduced significantly, reaching better results than the PGGs printed using HB and HNB strategies. The PGGs scanned using HB and NHB strategies show the same trend in volume fraction deviation. An average increase in volume fraction of 27% and 32% was evaluated for PGGs scanned by HB and HNB respectively. The last layers in the three PGGs show less deviation in volume fraction. This can be attributed to the accumulative shrinkage in each layer of the PGGs, which was amplified in only the last

layer. It might also be attributed to misalignment errors while CT scanning the PGGs. The variations can be better understood by evaluating dimensional accuracy of printed struts.

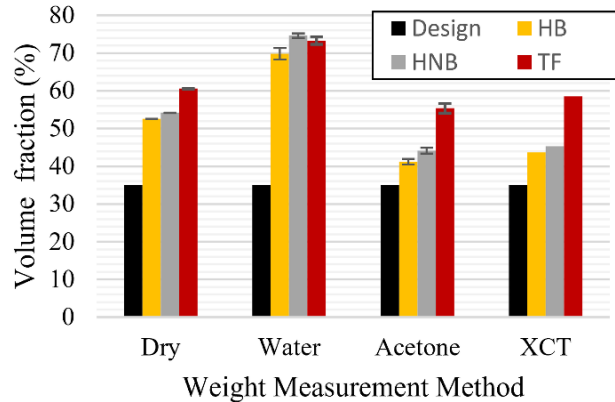


Figure 3-7: Total volume fraction obtained from different measurement methods compared to corresponding design values

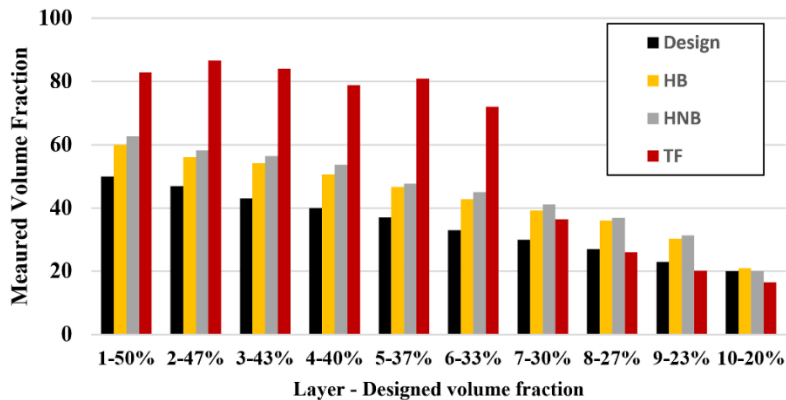


Figure 3-8: Layer's volume fraction obtained via μ CT and compared to corresponding design values

3.4.3 Dimensional accuracy

The struts sizes were measured in 4 different reconstructed layers [volume fractions=50%, 40%, 30% and 20%]. The deviation in size between the design struts and the reconstructed

struts are plotted in Fig. 9. The PGG scanned using TF strategy had significantly high size deviation in lower layers (high volume fraction), these deviations are reduced significantly at upper layers (low volume fraction). The PPGs scanned using HB and HNB strategies again show similar trends, with the HB strategy being more accurate. The measurements taken were randomly distributed from the same layer to make sure the results were consistent and reduce the errors resulting from misalignment while scanning. Average errors were in the order of 0.07 mm in the first layers (large struts), reaching a maximum of 0.25 mm in the last layers (small struts).

The TF strategy resulted in the highest errors in strut sizes in the first layers (high volume fraction), when compared to HB and HNB strategies. By analyzing the scan path scan path of the three scanning strategies as shown in Fig. 10. In the TF strategy three contours are needed to cover the strut size geometry at the first layers. The process parameter settings determine the amount of energy delivered to the powder, therefore affects the melt pool size generated in each scan. The higher the laser energy input, the larger the melt pool size.

The distance between hatch spacing and contours affects the melt pools to overlapping. Although overlapping is required to ensure good melt structure, too much overlapping can cause accumulation of energy [38]. It is assumed that the collapse of the first 6 layers is a result of large amount of energy generated from overlapping from concentric contours. In addition to the fact that no rotation occurs between successive layers in this strategy, which also accumulates the energy [32]. This energy might be transferred to the layer below and re-melt it, thereby, changing the strut dimensions, pore distribution and volume fractions.

Large errors in small struts are attributed to the fact that the length of laser hatches is short and frequently repeated, and consequently the small printed struts has no time to cool

down. Kruth et al. [39] explained this phenomenon, the repetitive short scans increase the amount of laser energy input added to the small parts. Therefore, some accumulated energy may be conducted to the printed part sides leading to the adhesion of powder and resulting in an increase the measured volume fraction and strut size. This can be demonstrated by comparing the three laser scan paths used in this study, as illustrated by **Figure 3-10**. Since repetitive scans are performed in HB and HNB strategies, more errors were found in these parts than the part scanned with the TF strategy. The TF strategy compared to HB and HNB needed almost one contour to fully build the strut.

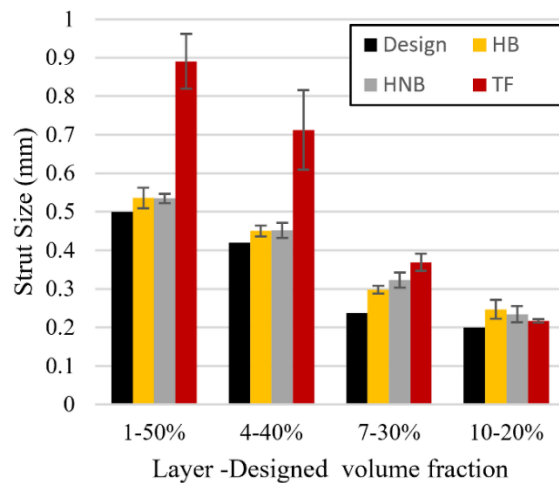


Figure 3-9: Strut size obtained via μ CT and compared to corresponding design values

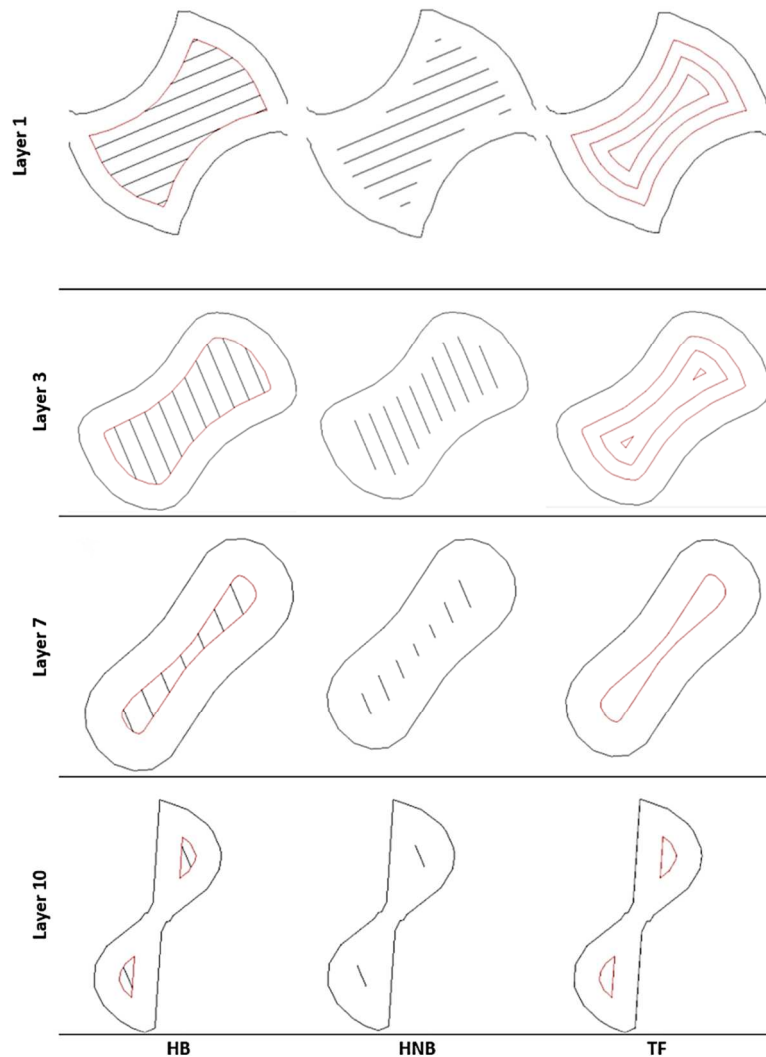


Figure 3-10: Laser scanning strategies along different layers of PGG

It was noted that the struts on the corner of the last layers were highly deviated from other struts in the middle of this layer. Therefore, a reconstruction of the last layer (volume fraction 20 %) from the three parts were all compared to the design reference layer. The mesh comparison tool in Netfabb[®] was used to evaluate the difference between the reference (design) and the printed (reconstructed) layers. **Figure 3-11** shows the mesh comparison for the last three layers of the printed PGGs. A notable deviation from the four

corners was observed. Parts printed using HB strategy had the highest deviation (± 1.21 mm, with a high repeatability of 0.253 mm). This deviation can be attributed to the presence of residual stress after the parts are separated from the base plate.

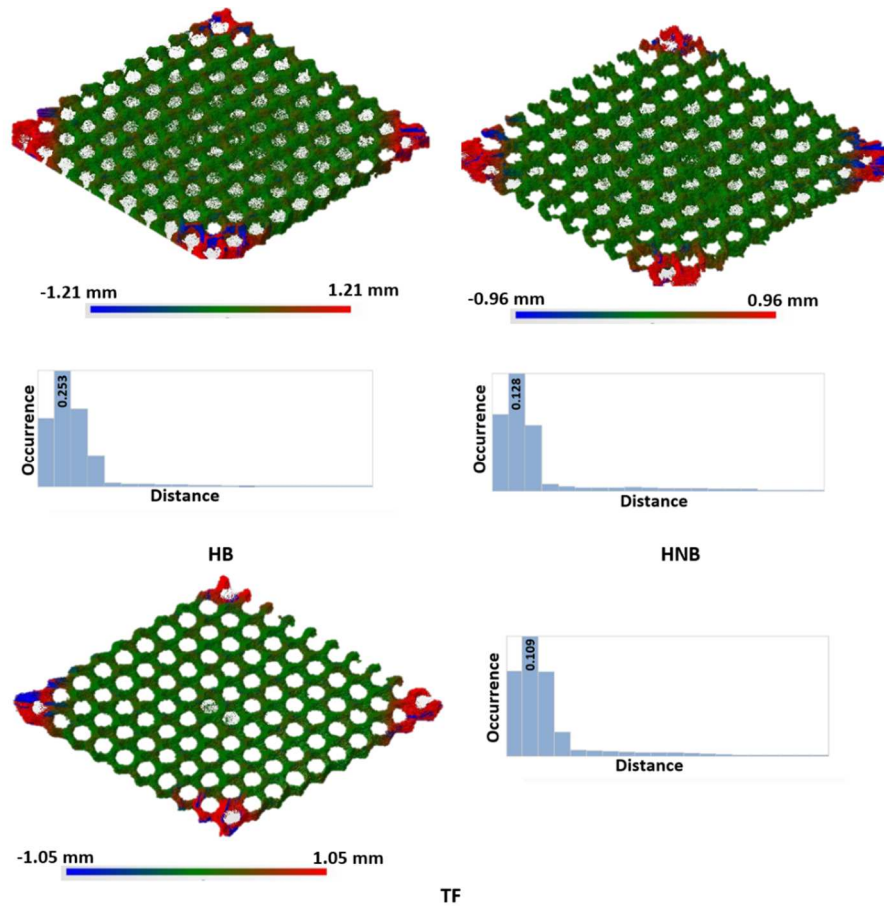


Figure 3-11: Mesh comparison of μ CT reconstruction and the CAD model for last layer of the three PGGs, red and blue represents plus and minus errors.

Histograms represents the occurrence of each value, dimensions in mm.

To observe the deviation on a strut level, a single row of the last layer of each part was compared to the reference design. From mesh comparison it was noted that errors in the PGG scanned by HB strategy were higher than the other strategies. All errors were found to be within ± 0.25 mm matching the results obtained from the vector [111] intersection

with single reconstructed gyroid unit cells. **Figure 3-12** displays the mesh comparison in each reconstructed layer. The benefit of using mesh comparison is to check the whole geometry, rather than one single position. For example, the PGGs scanned by HB and HNB strategies had large deviation in the diagonal struts, while the PGG scanned by TF strategy had some deviations in the struts but more deviations in the horizontal parts as well.

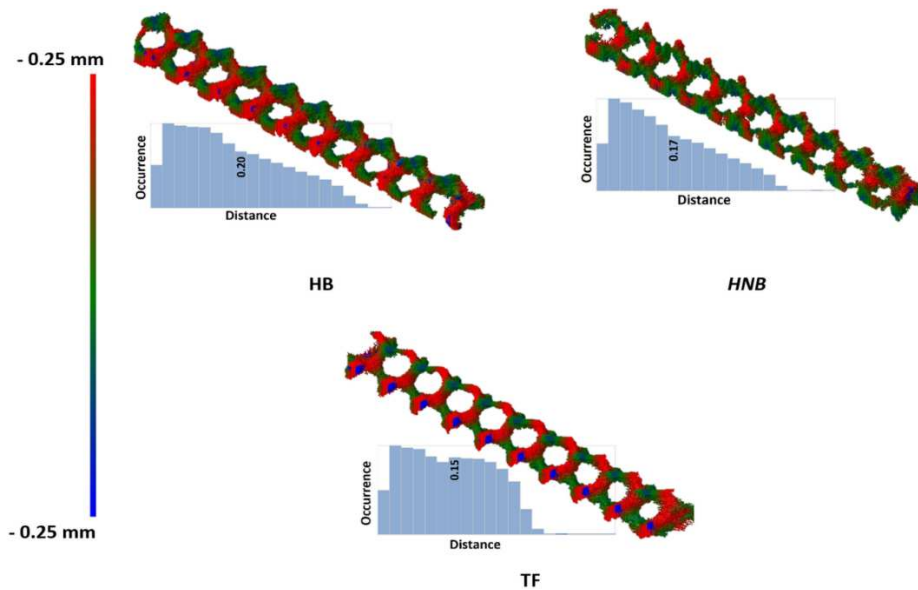


Figure 3-12: Mesh comparison of one row from the last layer obtained via μ CT and compared to the CAD model for the three PGGs, red and blue represents plus and minus errors. Histograms represent the occurrence of each value, dimensions in mm.

3.4.4 Surface integrity

The average surface roughness “Ra” values for different volume fractions are represented in Figure 3-13. It is noted that at upper layers (lower volume fraction) the surface roughness increases. The main reason for this increase is attributed to the geometry of the gyroids. As the struts become thinner, the connection between two adjacent struts become thinner, to the extent that it cannot be printed. Therefore, the upper layers are characterized

by a sinewave that was evident in the scanned profile. The first 6 layers, parts printed using TF strategy had a significantly lower surface roughness than the other two strategies. However, in the last 4 layers it was noted that there was high variation in roughness. The PGGs scanned by HB strategy had the least Ra. However according to Mumtaz et al. [40], Ra might not show strong correlation with the surface integrity. Therefore, to enhance the understanding of the surface integrity SEM was used to investigate the parts.

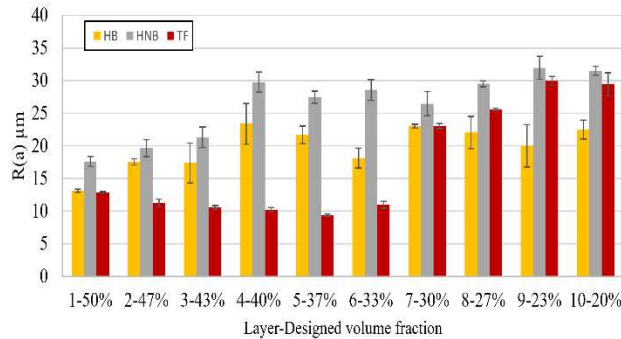


Figure 3-13: Average surface roughness “Ra” values for each layer along the powder layer thickness.

The SEM images for the first three layers and the last three layers are represented in Fig. 14. The PGGs scanned by HB and HNB strategies were seen to have a high appearance of balling effects present in the first three layers. The balling phenomena can occur due to the instability of melt pool, small sized droplets tend to splash out forming relatively large (micrometer-scaled) solidified spheres on the side of the printed parts [41]. Moreover, repetitive low speed scans contribute to increasing the amount of energy in the melt pool, causing balling phenomena to appear in PGGs scanned by HB and HNB strategies [42]. The PGG scanned by the TF strategy had a significantly large amount of partially melted powder adhering to its surface. This can be attributed again to the scans overlap and the accumulated energy in these struts. The energy gets conducted to the surface, however

since it is not high enough to melt the surrounding powder, the powder gets partially melted to the sides.

In the upper layers (lower volume fractions) the PGG scanned by HNB strategy have the highest amount of partially melted powder since no contour is made in this strategy. The surface of the PGG scanned by HB strategy has more partially melted powder and more non-uniform melted material compared to the part printed using TF strategy. This can be understood better by observing the laser scan paths presented by **Figure 3-14**. In HB scanning strategy, the hatch intersects the outer boundary of the laser. If the laser meltpool generated from the hatches is bigger than the meltpool generated to create the boundary contour, this can lead to the appearance of balling phenomena and irregular surface. As for the HNB strategy, if the distance between two successive laser exposures is too far it would result in an irregular surface as illustrated by **Figure 3-14(b)** The PGGs scanned using TF strategy needs only one boarder contour to melt the whole area of the strut in the upper layers. Therefore, no overlapping between contours occur and it is assumed that less accumulation of laser energy density occurs. Moreover, since there is no hatching in this strategy, the undesirable effect of hatching and boarders intersecting is avoided. Hence a more stable meltpool is evident and more melted tracks are detected.

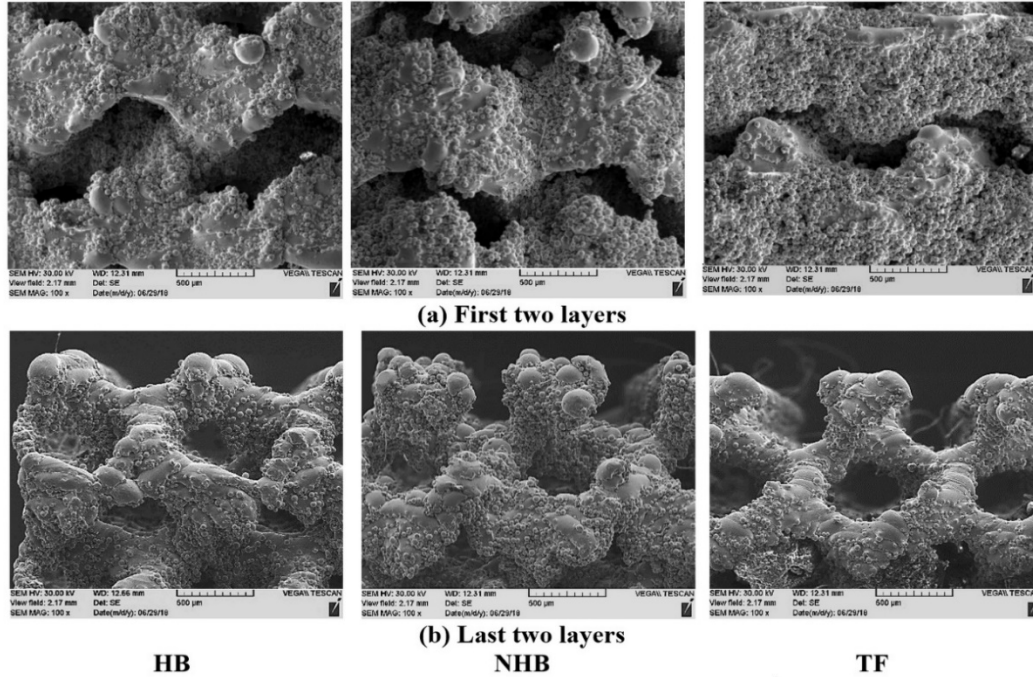


Figure 3-14: SEM images of the (a) first two layers and (b) last two layers of the PGGs.

3.5 Conclusion and future work

The scanning strategy in SLM was found to have a profound effect on the accuracy of printed lattice structures having porosity graded gyroid design. This paper presents a guide for the design of porosity grading of TPMS lattice structures for bone implant applications. The morphology of PGGs printed using SLM are investigated systematically and the following conclusions are derived:

- 1-The measured volume fraction and strut sizes of PGGs are higher than the design values. These errors are attributed to the partially melted powder on the surface of the PGGs and inability of SLM to create small strut size with high accuracy.

2-Each layer of the PGGs is affected differently by the scanning strategies. In lower layers (high volume fractions) the deviation in volume fraction and strut size is lower than that of the upper layers (low volume fraction).

3-Melt pool size, hatch spacing, and contour spacing may be considered as key factors in enhancing the strut size accuracy.

4-The TF scanning strategy might not be suitable for high volume fractions by the current process parameters settings. Proper control of the SLM process parameters, would enhance both high and low volume fraction struts quality.

In this study the process parameters recommended in the open literature for the SLM of bulk Ti6Al4V were used. These settings need to be adjusted for printing graded lattice structures. More research should target the “optimum” choice of laser energy density while printing those graded structures. Although the meltpool size and temperature weren’t measured in this study, it is suggested that they strongly affect the quality of the graded lattice structures. The precise monitoring of meltpool is considered extremely important to control the dimensional and surface integrity of printed graded lattice structures. The main objective should target reducing the amount of partially melted powder to the surfaces, enhance the dimensional accuracy, and surface integrity of the porosity graded lattice structures.

3.6 References

- [1] M. Cronskär, M. Bäckström, and L.-E. Rännar, “Production of customized hip stem prostheses – a comparison between conventional machining and electron beam melting (EBM),” *Rapid Prototyp. J.*, vol. 19, no. 5, pp. 365–372, 2013.
- [2] O. L. A. Harrysson, O. Cansizoglu, D. J. Marcellin-Little, D. R. Cormier, and H. A. West, “Direct metal fabrication of titanium implants with tailored materials and mechanical properties using electron beam melting technology,” *Mater. Sci. Eng. C*, vol. 28, no. 3, pp. 366–373, 2008.

- [3] R. Huiskes, H. Weinans, and B. van Rietbergen, “The relationship between stress shielding and bone resorption around total hip stems and the effects of flexible materials.,” *Clin. Orthop. Relat. Res.*, no. 274, pp. 124–134, 1992.
- [4] J. Van Der Stok et al., “Selective laser melting-produced porous titanium scaffolds regenerate bone in critical size cortical bone defects,” *J. Orthop. Res.*, vol. 31, no. 5, pp. 792–799, 2013.
- [5] E. Abele, H. A. Stoffregen, M. Kniepkamp, S. Lang, and M. Hampe, “Selective laser melting for manufacturing of thin-walled porous elements,” *J. Mater. Process. Technol.*, vol. 215, no. 1, pp. 114–122, Jan. 2015.
- [6] M. Helou and S. Kara, “Design, analysis and manufacturing of lattice structures: an overview,” *Int. J. Comput. Integr. Manuf.*, vol. 31, no. 3, pp. 243–261, 2017.
- [7] S. Rajagopalan and R. A. Robb, “Schwarz meets Schwann : Design and fabrication of biomorphic and durataxic tissue engineering scaffolds,” vol. 10, pp. 693–712, 2006.
- [8] H. A. Almeida and P. J. Bártolo, “Design of tissue engineering scaffolds based on hyperbolic surfaces: Structural numerical evaluation,” *Med. Eng. Phys.*, vol. 36, no. 8, pp. 1033–1040, 2014.
- [9] C. Yan, L. Hao, A. Hussein, and P. Young, “Ti – 6Al – 4V triply periodic minimal surface structures for bone implants fabricated via selective laser melting,” *J. Mech. Behav. Biomed. Mater.*, vol. 51, pp. 61–73, 2015.
- [10] A. Kumar, K. C. Nune, L. E. Murr, and R. D. K. Misra, “Biocompatibility and mechanical behaviour of three-dimensional scaffolds for biomedical devices: process–structure–property paradigm,” *Int. Mater. Rev.*, vol. 61, no. 1, pp. 20–45, 2016.
- [11] N. Taniguchi et al., “Effect of pore size on bone ingrowth into porous titanium implants fabricated by additive manufacturing: An in vivo experiment,” *Mater. Sci. Eng. C*, vol. 59, no. October 2015, pp. 690–701, 2016.
- [12] S. M. Ahmadi et al., “Additively manufactured open-cell porous biomaterials made from six different space-filling unit cells: The mechanical and morphological properties,” *Materials (Basel)*, vol. 8, no. 4, pp. 1871–1896, 2015.
- [13] S. Zhang, C. Li, W. Hou, S. Zhao, and S. Li, “Longitudinal Compression Behavior of Functionally Graded Ti–6Al–4V Meshes,” *J. Mater. Sci. Technol.*, vol. 32, no. 11, pp. 1098–1104, Nov. 2016.
- [14] D. S. J. Al-Saedi, S. H. Masood, M. Faizan-Ur-Rab, A. Alomarah, and P. Ponnusamy, “Mechanical properties and energy absorption capability of functionally graded F2BCC lattice fabricated by SLM,” *Mater. Des.*, vol. 144, pp. 32–44, 2018.
- [15] E. Onal, J. E. Frith, M. Jurg, X. Wu, and A. Molotnikov, “Mechanical properties and in vitro behavior of additively manufactured and functionally graded Ti6Al4V porous scaffolds,” *Metals (Basel)*, vol. 8, no. 4, 2018.
- [16] S. L. Sing, F. E. Wiria, and W. Y. Yeong, “Selective laser melting of lattice structures: A statistical approach to manufacturability and mechanical behavior,” *Robot. Comput. Integr. Manuf.*, vol. 49, no. January 2017, pp. 170–180, 2018.

- [17] S. L. Sing, W. Y. Yeong, F. E. Wiria, and B. Y. Tay, “Characterization of titanium lattice structures fabricated by selective laser melting using an adapted compressive test method,” *Exp. Mech.*, vol. 56, no. 5, pp. 735–748, 2016.
- [18] Z. A. Ahmadi SM, Hedayati R, Jain RA, Li Y, LeeFlang S, “Effects of laser processing parameters on the mechanical properties, topology, and microstructure of additively manufactured porous metallic biomaterials: A vector-based approach,” *Mater. Des.*, vol. 134, pp. 234–243, 2017.
- [19] D. Dai et al., “Influence of scan strategy and molten pool configuration on microstructures and tensile properties of selective laser melting additive manufactured aluminum based parts,” *Opt. Laser Technol.*, vol. 99, pp. 91–100, Feb. 2018.
- [20] S. Ghouse, S. Babu, R. J. Van Arkel, K. Nai, P. A. Hooper, and J. R. T. Jeffers, “The influence of laser parameters and scanning strategies on the mechanical properties of a stochastic porous material,” *Mater. Des.*, vol. 131, pp. 498–508, 2017.
- [21] S. C. Kapfer, S. T. Hyde, K. Mecke, C. H. Arns, and G. E. Schröder-Turk, “Minimal surface scaffold designs for tissue engineering,” *Biomaterials*, vol. 32, no. 29, pp. 6875–6882, 2011.
- [22] F. P. W. Melchels, K. Bertoldi, R. Gabbriellini, A. H. Velders, J. Feijen, and D. W. Grijpma, “Mathematically defined tissue engineering scaffold architectures prepared by stereolithography,” *Biomaterials*, vol. 31, no. 27, pp. 6909–6916, 2010.
- [23] D. Melancon, Z. S. Bagheri, R. B. Johnston, L. Liu, M. Tanzer, and D. Pasini, “Mechanical characterization of structurally porous biomaterials built via additive manufacturing: experiments, predictive models, and design maps for load-bearing bone replacement implants,” *Acta Biomater.*, vol. 63, pp. 350–368, 2017.
- [24] S. Arabnejad, R. Burnett Johnston, J. A. Pura, B. Singh, M. Tanzer, and D. Pasini, “High-strength porous biomaterials for bone replacement: A strategy to assess the interplay between cell morphology, mechanical properties, bone ingrowth and manufacturing constraints,” *Acta Biomater.*, vol. 30, pp. 345–356, 2016.
- [25] F. S. L. Bobbert et al., “Additively manufactured metallic porous biomaterials based on minimal surfaces : A unique combination of topological , mechanical , and mass transport properties,” *Acta Biomater.*, vol. 53, pp. 572–584, 2017.
- [26] P. Heintz, L. Müller, C. Körner, R. F. Singer, and F. A. Müller, “Cellular Ti-6Al-4V structures with interconnected macro porosity for bone implants fabricated by selective electron beam melting,” *Acta Biomater.*, vol. 4, no. 5, pp. 1536–1544, Sep. 2008.
- [27] J. Yang et al., “In Vivo Study of a Self-Stabilizing Artificial Vertebral Body Fabricated by Electron Beam Melting,” *Spine (Phila. Pa. 1976)*, vol. 39, no. 8, pp. E486–E492, Apr. 2014.
- [28] H. J. Rack and J. I. Qazi, “Titanium alloys for biomedical applications,” *Mater. Sci. Eng. C*, vol. 26, no. 8, pp. 1269–1277, Sep. 2006.

- [29] P. Mercelis, J. Kruth, and J.-P. Kruth, “Residual stresses in selective laser sintering and selective laser melting Residual stresses in selective laser sintering and selective laser melting,” *Rapid Prototyp.*, vol. 12, no. 10, pp. 254–265, 2006.
- [30] J.-P. Kruth, J. Deckers, E. Yasa, and R. Wauthlé, “Assessing and comparing influencing factors of residual stresses in selective laser melting using a novel analysis method.”
- [31] J. M. Walker, E. Bodamer, A. Kleinfehn, Y. Luo, M. Becker, and D. Dean, “Design and mechanical characterization of solid and highly porous 3D printed poly(propylene fumarate) scaffolds,” *Prog. Addit. Manuf.*, vol. 2, no. 1–2, pp. 99–108, 2017.
- [32] A. Kudzal et al., “Effect of scan pattern on the microstructure and mechanical properties of Powder Bed Fusion additive manufactured 17-4 stainless steel,” *Mater. Des.*, vol. 133, pp. 205–215, Nov. 2017.
- [33] T. Schwanekamp, M. Bräuer, and M. Reuber, “Geometrical and topological potentialities and restrictions in selective laser sintering of customized carbide precision tools,” vol. 49, no. 0, 2017.
- [34] G. Ter Haar, T. H. Becker, G. M. Ter Haar, and T. H. Becker, “Selective Laser Melting Produced Ti-6Al-4V: Post-Process Heat Treatments to Achieve Superior Tensile Properties,” *Materials (Basel)*, vol. 11, no. 1, p. 146, Jan. 2018.
- [35] S. T. Ho and D. W. Hutmacher, “A comparison of micro CT with other techniques used in the characterization of scaffolds,” *Biomaterials*, vol. 27, no. 8, pp. 1362–1376, Mar. 2006.
- [36] A. Ataee, Y. Li, D. Fraser, G. Song, and C. Wen, “Anisotropic Ti-6Al-4V gyroid scaffolds manufactured by electron beam melting (EBM) for bone implant applications,” *Mater. Des.*, vol. 137, pp. 345–354, Jan. 2018.
- [37] C. Han et al., “Continuous functionally graded porous titanium scaffolds manufactured by selective laser melting for bone implants,” *J. Mech. Behav. Biomed. Mater.*, vol. 80, no. March 2017, pp. 119–127, 2018.
- [38] X. Su and Y. Yang, “Research on track overlapping during Selective Laser Melting of powders,” *J. Mater. Process. Technol.*, vol. 212, no. 10, pp. 2074–2079, Oct. 2012.
- [39] J. P. Kruth, L. Froyen, J. Van Vaerenbergh, P. Mercelis, M. Rombouts, and B. Lauwers, “Selective laser melting of iron-based powder,” *J. Mater. Process. Technol.*, vol. 149, no. 1–3, pp. 616–622, Jun. 2004.
- [40] K. Mumtaz and N. Hopkinson, “Top surface and side roughness of Inconel 625 parts processed using selective laser melting,” *Rapid Prototyp. J. Rapid Prototyp. J. Iss Rapid Prototyp. J.*, vol. 15, no. 5, 2009.
- [41] D. Gu and Y. Shen, “Balling phenomena in direct laser sintering of stainless steel powder: Metallurgical mechanisms and control methods,” *Mater. Des.*, vol. 30, no. 8, pp. 2903–2910, Sep. 2009.
- [42] K. A. Mumtaz and N. Hopkinson, “Selective Laser Melting of thin wall parts using pulse shaping,” *J. Mater. Process. Technol.*, vol. 210, no. 2, pp. 279–287, Jan. 2010.

Chapter 4

Effect of Microstructure and Internal defects on the Mechanical Properties of Ti6Al4V Gyroid Lattice Structures for Biomedical Implants

Complete Citation:

Mahmoud, Dalia, M. A. Elbestawi, and Kassim S. Al-Rubaie " Effect of Microstructure and Internal defects on the Mechanical Properties of Ti6Al4V Gyroid Lattice Structures for Biomedical Implants." *Accepted in selected technical papers of ASTM*

Copyright:

© 2020 ASTM

Relative Contributions:

Dalia Mahmoud: Performed experiments, analysis, and data interpretation. Wrote the first draft of the manuscript.

M. A. Elbestawi: Revised and edited the manuscript.

Kassim S. Al-Rubaie: Revised the microstructural analysis and interpretation.

Abstract

Selective laser melting (SLM) is a laser powder bed fusion (L-PBF) technique that can be used to print lattice structures with fine complicated features. Much effort has been made to choose a lattice design that enhances the mechanical and biological functions for biomedical implants. Triply periodic minimal surfaces (TPMS) lattice structures, namely gyroids, have shown a great potential to match the mechanical and biological properties of bone tissue. Although the design plays a major role in determining the properties of lattice structures, the effect of the SLM process on the lattice structure quality is often overlooked. This work focuses on the relationship between the resultant microstructure and the mechanical properties of Ti6Al4V gyroid lattice structures. Different process parameter combinations were used to develop a wide range of volumetric energy density (VED). The gyroid design was then printed at three VED levels: 43, 103, and 192 J/mm³. The apparent density, morphology, and internal defects were analyzed. Micro-computed tomography (micro-CT) was used for characterizing the morphology of the samples. The results showed that the apparent density was highly dependent on the VED level; the density of the parts printed with VED of 192 J/mm³ was 150% higher than that of those printed with VED of 43 J/mm³. The percentage of internal defects ranged from 0.3 to 2.1%, was directly proportional to the VED level. The mechanical strength was more dependent on the overall density rather than the internal defects. Thus, parts printed at VED of 192 J/mm³ had almost 200% higher apparent compressive modulus and peak strength compared to those printed at VED of 43 J/mm³. In addition, a finite element model has been developed using ABAQUS®. The numerical results were in good agreement with the experimental data and may be used to make predictions for different gyroid design

Keywords:

Lattice structures, Selective Laser Melting, Mechanical properties, Internal defects, Gyroids, Finite element analysis.

Acknowledgment:

The authors acknowledge the funding of the Natural Sciences and Engineering Research Council of Canada (NSERC; funding reference number 518494).

4.1 Introduction

Titanium and its alloys have excellent biocompatibility, low stiffness, high specific strength, and high corrosion resistance. These advantages make these alloys superior for biomedical applications over other metallic alloys such as stainless steels and Co-Cr alloys[1]. Moreover, the breakthrough in additive manufacturing technology, specifically selective laser melting (SLM), makes titanium alloys excellent candidates for manufacturing biomedical implants[2]. Since titanium alloys are hard to machine and relatively expensive, SLM offers a much easier way to manufacture implants. Conventional processes, such as casting and forging, are energy-consuming and incapable of producing the required customization that is easily provided by SLM processes[3]. Furthermore, SLM provides shorter production time and more advanced functionality, such as the option of printing the parts in the form of lattice structures or functionally graded materials[4].

A major challenge in the SLM process is the rapid solidification that results in highly non-equilibrium microstructures [5]. Therefore, much work is dictated to relate SLM process parameters to the resulting microstructure and internal defects of the printed titanium parts[6]–[8]. Numerical modelling can also help in predicting the microstructure features of metallic parts printed by SLM[9]. The most critical parameters usually considered are those involved in the volumetric energy density (VED)[10], namely, laser power, scan speed, layer thickness, and hatch spacing. Due to the high variability of the process, feedstock powder, and shape of the printed parts, it might be difficult to optimize a set of process parameters of volumetric energy density[5]. For example, Kasperovich et al.[11] defined a VED value of 117 J/mm^3 to obtain fully dense Ti6Al4V parts, whereas Pal et al.[12] reported highest density of bulk parts printed at a VED level of 68 J/mm^3 .

An important consideration is the geometry and temperature of melt pool created by the interaction between the laser and metallic powder. Yang et al.[13] classified the melting mode in SLM into two types: conduction mode and keyhole mode. The conduction mode is defined by a low to moderate VED, whereas the keyhole mode is associated with high VED capable of penetrating previously melted layers. While each mode has its pros and cons, a trade-off between both modes should be reached to ensure the adequate performance of printed parts. The melt pool mode affects the formation of internal porosities, which are crucial to the performance of the printed parts. In this regard, the effect of shielding gas flow velocity on the melt pool size has been studied[14]. It was found that below a certain threshold, the melt pool becomes unstable and its width increases significantly. Pegues et al.[15] investigated the influence of internal defects on the tensile properties of bulk parts and concluded that their effect on the ductility was greater than on the yield and tensile strength. Gong et al.[6] concluded that internal porosity less than 1% has no effect on the mechanical properties; however, a higher percentage (1 – 5%) may significantly affect tensile strength, fatigue, and hardness of the parts.

A major difference between printing lattice structures and bulk parts is that the lattice part contains porosities designed for certain applications. These intended porosities make the laser scan vector relatively shorter, thus resulting in less residual stresses in lattice structures[16]. Some efforts have been made to investigate the effect of SLM process parameters on the dimensional and mechanical properties of CAD-based lattice structures[17]–[19]. It can be concluded that laser power plays a critical role in determining the lattice strut size since it affects the melt pool temperature and size. However, the effect of the SLM process parameters on the quality of complicated structures such as triply periodic minimal surfaces (TPMS) lattices is usually overlooked.

TPMS lattice structures are identified by having a zero-mean curvature at all points. They are known to have bio-mimetic features[20], [21]. They have interconnected porosities, which make them a good candidate to be used as a bone replacement. Much effort is being made to investigate the pore size[22] and functionally graded porosity[23], [24] of TPMS structures on the mechanical properties of these parts. However, very few studies[25] cover how SLM process parameters affect the microstructure, geometry and internal defects. A gap in understanding the effect of the defects on the mechanical properties is present.

The main contribution of this work is to study the effect of VED on the quality of complicated gyroid lattice structures. The microstructure, geometrical and internal defects resulting from different VED values have been analyzed. Furthermore, the effect of these defects on the mechanical properties of lattice structures has been studied and compared to similar Ti6Al4V lattice structures from the literature. Finally, an FEA model was proposed to be used to predict the mechanical properties of those gyroid structures.

4.2 Materials and methods

4.2.1 Design and 3d printing

Triply periodic minimal surfaces (TPMS) lattice structure designs were tested in this work, namely the cellular gyroid unit cells[26]. These designs are biomimetic and well suited for biomedical implants applications for various reasons, including high surface area to volume ratio, interconnected porosity, and adequate mechanical strength[27]. Figure 4-1 represents the cylindrical-shaped gyroid lattice structures possessing a diameter of 15 mm and a length of 23.5 mm. Each unit cell was designed to have a length of 1.5 mm; the design relative density is 0.20%. Plasma atomized Ti6Al4V powder having an average

particle size of 45 μm was used as a feedstock material; the powder composition is given in Table 4-1.

Table 4-1: Chemical composition (wt.%) of the Ti6Al4V powder

Al	V	Fe	O	C	N	H	Y	Ti
5.50– 6.50	3.50– 4.50	≤ 0.25	≤ 0.13	≤ 0.08	≤ 0.05	≤ 0.012	≤ 0.005	Bal.

An AM400 Renishaw machine equipped with Nd:YAG laser with a maximum power of 400 W was used to print the lattice structures. The Renishaw machine works by a pulsed modulated laser, where the laser path is defined by a series of exposures overlapping each other. A pulsed laser is recommended for small components such as laser components since this technique provided more control over the heat input compared to continuous laser [28]. The distance between the exposure points is known as a point distance. In this work, a combination of laser power and exposure time values are used to obtain three levels of volumetric energy densities (VED). The effects of these levels on the microstructure, internal defects, and in turn on the mechanical properties of gyroid lattice structures of SLM-Ti6Al4V, have been studied in detail.

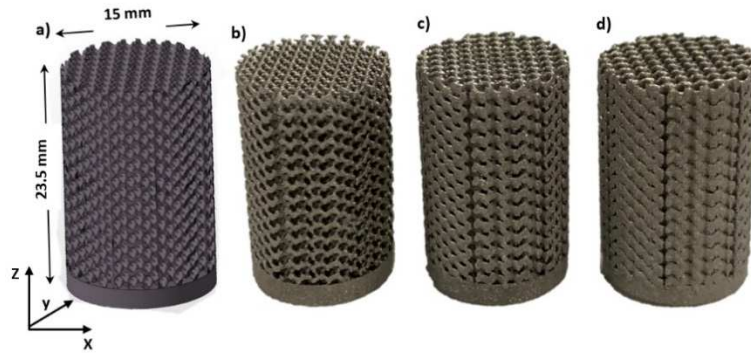


Figure 4-1: (a) Gyroid part design and as-built parts using SLM process at different VED levels: (b) 43 J/mm³, (c) 103 J/mm³, and (d) 192 J/mm³.

The value of point distance is set to 60 μm ; the layer thickness and hatch distance were kept fixed at 30 μm and 65 μm , respectively. According to Karimi et al.[29], VED can be calculated using Equation (1). Table 4-2 shows the calculated VED levels. In this study, a value of 10 μs was added to each exposure time to account for delay time between each exposure and the other.

$$VED = \frac{\text{Laser Power}}{\frac{\text{Point distance}}{\text{Exposure time}} \times \text{hatch distance} \times \text{layer thickness}} \quad \text{Equation 4-1}$$

Table 4-2: Process parameters and calculated volumetric energy density (VED) for each sample.

Samples	Laser Power (W)	Exposure Time (μs)	VED (J/mm ³)
Low VED	100	40	43
Med VED	200	50	103
High VED	300	65	192

4.2.2 Microstructure characterization

According to the metallographic preparation standard, samples were sectioned from the parts built at three VED levels, mounted, ground, mechanically polished, and then etched by Kroll's reagent. For the microstructural characterization, a JOEL SEM microscope and a Nikon optical microscope were used. Moreover, the X-ray diffraction was carried out by a Bruker D8 DISCOVER XRD instrument provided with a cobalt sealed tube source.

4.2.3 Morphology and internal defects characterization

A Skyscan 1172 was used to perform micro-CT scanning for the printed parts. In this work, 100 kV was used, with a 0.5 mm Al and 0.038 Cu filter combination. The size and the position of the printed part relative to the X-ray source and the detector determine the pixel size. Although less pixel size can be obtained by scanning a small bisected part of the sample, difficulties associated with part size, beam hardening, and scattering are some limiting factors. In this study, a pixel size of 8 μm was achieved to scan the whole part. The specimen was rotated around the z-axis in 1600 steps, with 3 s exposure for each orientation. The analysis of the CT scans was performed using CTAn and CTvol software suites.

4.2.4 Mechanical Testing

Uniaxial compression tests were carried out using an MTS testing machine with 50 kN load cell, in accordance with ISO 13314 standard. Crosshead displacement was set to be 2 mm/min (strain rate of 0.001 mm/s). Three samples were tested at each VED level to ensure the accuracy of the collected data. The stresses were calculated by multiplying the forces recorded from the load cell by the cross-section area. The strain was measured using crosshead displacement (taking into consideration compliance correction) and a video

camera for some specimens. The difference between both results was less than 3%. Therefore, all the data collected in this work were obtained by the crosshead displacement after a compliance correction.

4.2.5 Finite element analysis

To understand the effect of microstructure and morphology on the stress-strain relationship of the gyroids structures, FEA was performed using ABAQUS/EXPLICIT-6.14 to simulate the quasi-static compression. In this study, an elastic-plastic model was used in the simulation for the material model based on the experimental results for as-built properties obtained by Cain et al.[30]; future studies would consider the failure criteria. Two rigid plates simulate the compression platens. The displacement of the upper plate was defined to match that of experimental and maintain the same strain rate, whereas the lower plate was fixed. The gyroid models were meshed using voxel meshing techniques. Voxel mesh is usually used to model biomedical parts since the complexity, and highly detailed parts are usually hard to model with conventional mesh shapes[31]. Another advantage of voxel meshing is that it requires less computational time and gives a straightforward solution for modelling highly complex structures[32]. Finite-size models are usually suggested for lattice structures[33], in which instead of modelling the whole part, only a small number of elements are modelled. For example, Gonzalez et al.[34] found that modelling 8×8 unit cells minimize the difference between the whole model and the finite model. In this work, to reduce the model size, only a quarter of the sample height was considered. The model was composed of 3002786 elements, with an element size of 35 μm . The element size chosen was based on a mesh sensitivity analysis that ensured the convergence of the stiffness and peak strength.

4.3 Results and discussion

4.3.1 Microstructure

The optical micrographs of the SLM fabricated Ti6Al4V gyroid parts, printed at three VED levels along the build direction are shown in Figure 4-2 (a, b, and c). Very fine laths representing acicular α' -martensite can be observed within the columnar structures. The formation of these fine laths is due to very high cooling rates of the SLM process. The elongated columnar structures represent the prior β grains formed upon solidification. The optical micrographs for the top surface of the printed gyroid parts are seen in Figure 4-2 (d, e, and f). It can be noted that the microstructures of the top surface and the cross-sectional surface are similar.

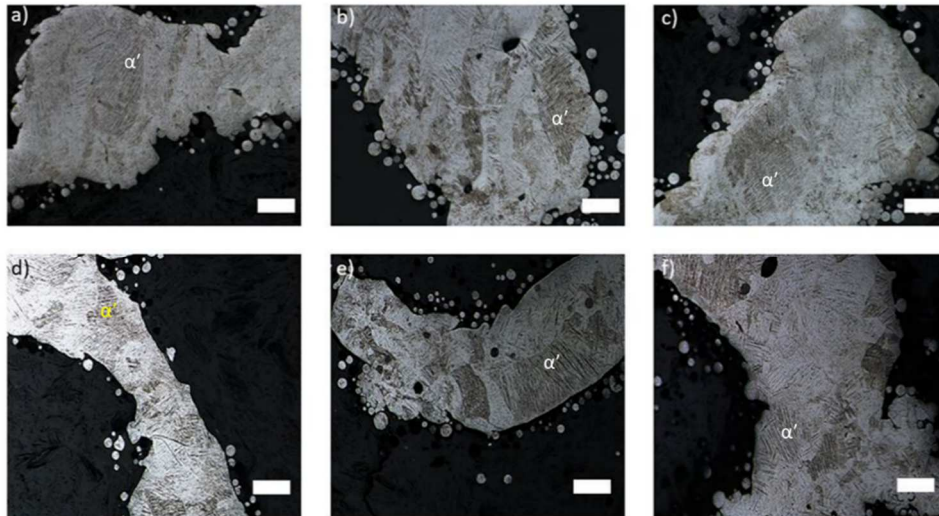


Figure 4-2: Optical micrographs (100x) of the Ti6Al4V gyroids printed at three VED levels: (a), (d) at 43 J/mm^3 ; (b), (e) at 103 J/mm^3 ; and (c), (f) at 192 J/mm^3 . (a), (b), and (c) were taken along the build direction. (d), (e), and (f) were taken from the top side. Scale bars are equal to $100 \mu\text{m}$.

The SEM micrographs of the Ti6Al4V gyroid parts printed at three VED levels are illustrated in Figure 4-3. Generally, the microstructure of as-built parts consists of a lath-type α' -martensite; however, its size slightly increases as the VED increases. This behavior may be attributed to a reduction in the cooling rate as the VED increases[35]. According to its size[36], α' -martensite can be classified into four types: primary, secondary, tertiary, and quaternary. The laths of primary martensite are the biggest, whereas those of the quaternary are the finest, being distributed among the laths of the tertiary martensite. The laths of secondary martensite, comparatively denser and smaller than those of the primary martensite, lie perpendicular or at about 45° to them. All these types of α' -martensite can be seen in Figure 3. The results of this work are in agreement with those obtained by Gong et al.[6], indicating that the VED does not have a significant effect on the microstructure evolution, which is basically governed by the cooling rate.

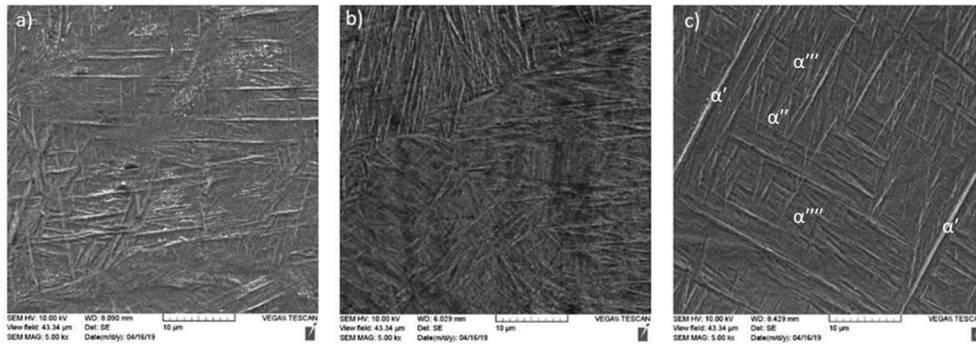


Figure 4-3: SEM images (5000x) of the gyroid parts printed at different VED levels: (a) 43 J/mm^3 , (b) 103 J/mm^3 , and (c) 192 J/mm^3 .

The XRD spectrum of the samples processed at three VED levels is presented in Figure 4-4. Similar diffraction patterns can be seen, in which all the peaks can be identified as α' -martensite having the same crystal structure of hexagonal close-packed (hcp) type. This

may be expected due to extremely fast cooling rates occurring during the solid-state phase transformation, thus leading to a diffusion-less transformation of the high-temperature β -phase into a fully α' -martensite. However, the peaks in the sample processed at VED of 43 J/mm³ are slightly broader relative to the same peaks of the samples processed at 103 and 192 J/mm³. This broadening of the peaks may be related to very fast cooling rates that occur during the SLM process, thus hindering the diffusion of vanadium from α' -martensite. The supersaturation of vanadium leads to a crystal deformation and broadening of the related peaks[37].

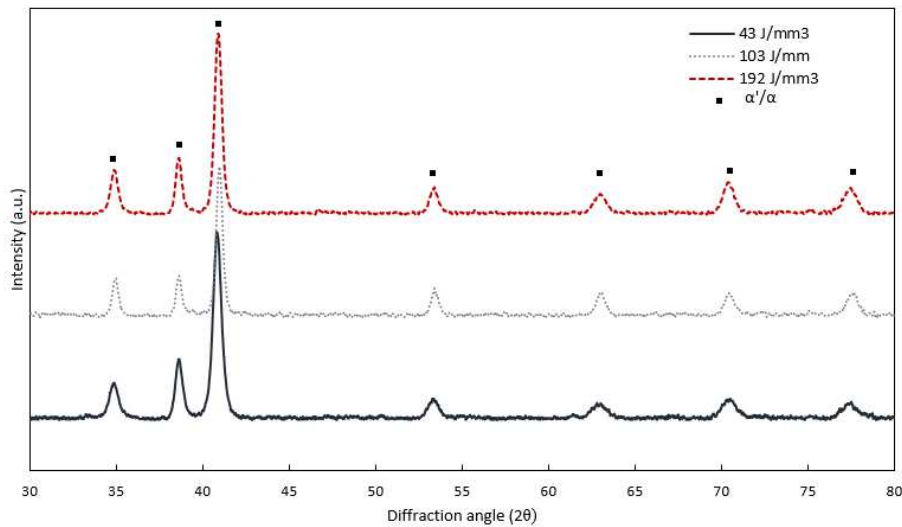


Figure 4-4: XRD analysis for the Ti6Al4V gyroid parts printed at different VED.

Morphology

Micro-CT scanning was used to evaluate the internal porosity of the parts. The parts were cut into smaller lengths (10 mm) to make sure adequate resolution can be obtained. The struts of the gyroid parts were all characterized using micro-CT; the trabecular thickness measurement for each strut was carried out using the 2D analysis tool pack in CTAn®.

Whereas, the bone to tissue ratio was measured using the 3D analysis tool pack to evaluate the relative density of each part. Figure 4-5 shows the design of a cross-section of the gyroid parts along with the micro-CT slices; all the slices are taken at a constant height from the base of the parts (height = 9.5 mm). As the VED level increases, the white area percentage increases. This indicates that the percentage of melted Ti6Al4V increases. This was noted by the increase in relative density and strut size listed in Table 4-3. However, at VED level of 43 J/mm³ some broken and incomplete struts can be seen. This might be attributed to the fact that the energy is insufficient to melt the powder. Therefore, some balling may occur along the melt track, as well as lack of fusion between successive layers that might not be visible in the cross-section but will result in incomplete struts or empty gaps instead of solid struts. As the VED level increases, more energy is provided to the powder, and therefore the melt pool size increases, leading to a thicker strut and higher relative density for the entire part.

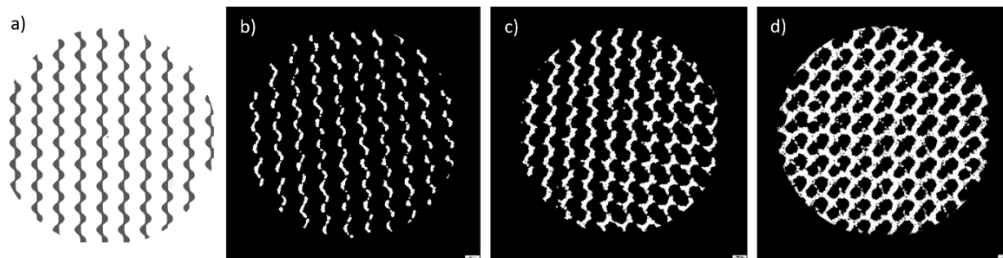


Figure 4-5: Micro-CT slices taken from a constant height = 9.5 mm from base of the gyroid parts at different VED levels (a) design, (b) 43 J/mm³, (c) 103 J/mm³, and (d) 192 J/mm³.

Table 4-3: Apparent density, strut size, and internal defect percentage of Ti6Al4V gyroid parts at three VED levels.

VED (J/mm ³)	Apparent density (%)	Average strut size (μm)	St. dev. (μm)	Internal porosity (%)
43	17	271.3173	8.8607	0.323
103	31	293.7477	11.7801	0.626
193	40	302.1761	1.3431	2.11

4.3.2 Internal porosity

Figure 4-6 represents a reconstructed gyroid unit cell from the different parts printed at different VED levels. The internal porosity was calculated from the whole parts and reported in Table 4-3. 3D object analysis tool pack in the software was used to analyze equivalent pore diameters. A histogram of the pore frequency distribution along the whole part is illustrated in Figure 4-7, a random distribution with no specific pattern was observed.

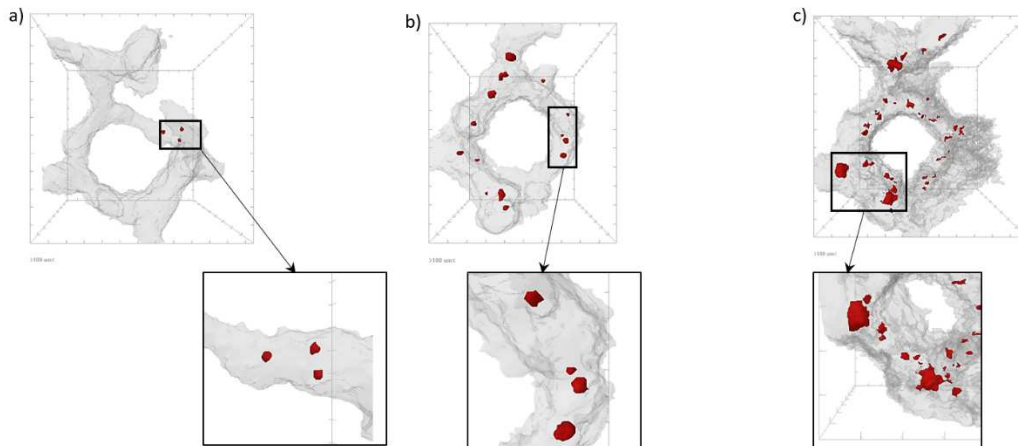


Figure 4-6: Reconstructed gyroid unit cells at different VED levels: (a) 43 J/mm³, (b) 103 J/mm³, and (c) 192 J/mm³.

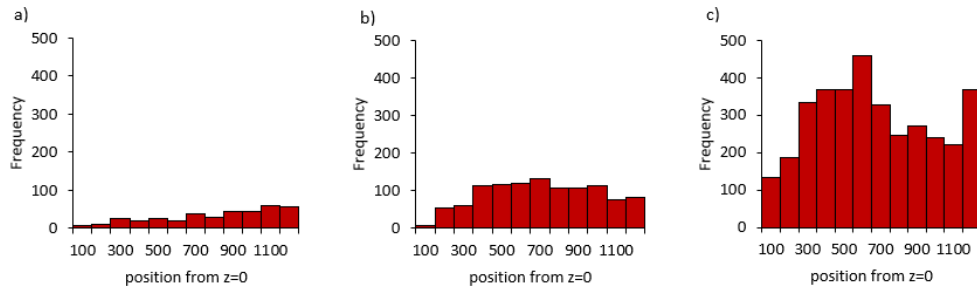


Figure 4-7: Pore frequency distribution along with the build directions of gyroid lattice structures printed at three VED levels: (a) 43 J/mm^3 , (b) 103 J/mm^3 , and (c) 192 J/mm^3 .

Figure 4-8 represents the histogram distribution for the equivalent pore diameter and the frequency in each part along the build direction. Parts printed at VED 43 J/mm^3 were found to have the least frequency of internal porosities. As the VED increases to 103 J/mm^3 , the strut size increases, and internal porosity starts to increase as well. As the VED reaches 192 J/mm^3 , the strut size and the internal porosity become bigger. It should be noted that the resolution of the micro-CT was $8 \mu\text{m}$ for each pixel in this study. Thus, the minimum diameter of internal porosity that can be detected for these parts was limited to 2 times the resolution ($16 \mu\text{m}$), which is the cut-off usually used in literature[38], [39]. The most common repeatable equivalent pore diameter was $40 \mu\text{m}$; the highest frequency was around 7000 in the gyroid parts printed with high VED level. According to Vilaro et al.[40], most pores between ($10 - 50 \mu\text{m}$) may be attributed to entrapped gas during the melting process. These errors can be reduced by increasing the apparent density of the powder bed or by reducing the inert gas pressure while printing.

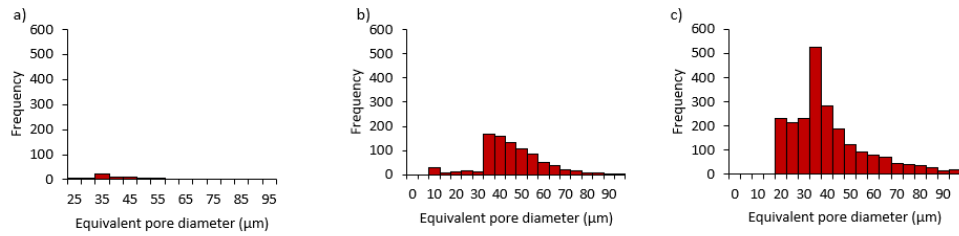


Figure 4-8: Internal pore size distribution for equivalent pore diameter in gyroid lattice structures printed at different VED levels: (a) 43 J/mm^3 , (b) 103 J/mm^3 , and (c) 192 J/mm^3 .

In addition, the aspect ratio of these pores within the three parts was analyzed as well; aspect ratio was defined as the minimum diameter divided by the maximum diameter[41]. Therefore, a perfect spherical porosity would have an aspect ratio of 1. As the shape of the pore becomes distorted, the aspect ratio decreases. For the parts printed at VED of 43 J/mm^3 , the aspect ratio of 0.9 – 1 was noted to be the most common ratio of these porosities, as shown in Figure 4-9. As the level of VED increases, the aspect ratio drops. Parts printed at 192 J/mm^3 were reported to have aspect ratio reaching 0.6. Although melt pool temperature and geometry have not been measured in this study, the change in the frequency and shape of internal porosities is usually attributed to the change in melt pool condition from conduction to keyhole[42]. This is related to the amount of energy delivered to the powder and the laser power; high laser power creates a spatter in the molten metal, causing a pore formation that looks like a keyhole.

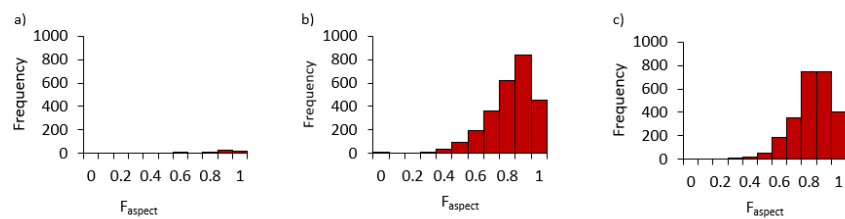


Figure 4-9: Aspect ratio for internal pores of the different gyroid lattice structures printed at different VED: (a) 43 J/mm³, (b) 103 J/mm³, and (c) 192 J/mm³.

4.3.3 Mechanical properties

Figure 4-10 depicts the stress-strain diagrams of the samples of Ti6Al4V gyroid lattice structures printed at different VED levels. The typical stress-strain diagram of lattice structures is divided into three zones: elastic zone, plateau zone, and densification zone. For biomedical applications, four important values are usually considered: the apparent modulus of elasticity, the apparent compressive strength, the elastic strain, and the densification strain.

Parts printed at low VED of 43 J/mm³ had the lowest apparent modulus of elasticity and compressive strength but the highest elastic strain. As the VED level increases, both the apparent modulus of elasticity and compressive strength are seen to increase. On the other hand, elastic strain and densification strain are noted to decrease. In our previous study[43], we investigated the effect of morphology on the mechanical properties. It was noted that as the VED increases, the strut thickness increases, thereby enhancing the strength of the gyroid structure. In this study, we have examined the microstructure and phase analysis of the gyroid parts printed at different VED levels. It can, therefore, be assumed that the internal defects do not affect the apparent modulus of elasticity and compressive strength; however, they do affect the elastic and densification strain.

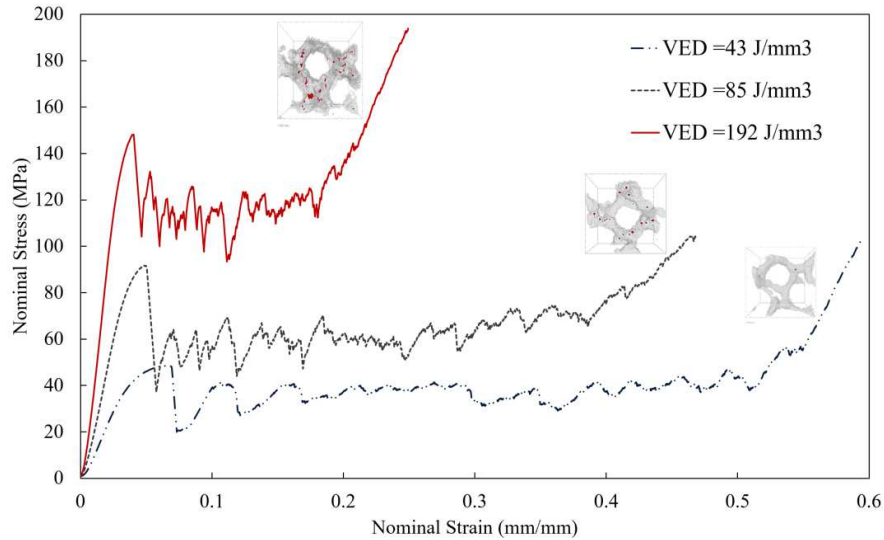


Figure 4-10: Stress-strain diagram of the gyroid parts at different VED levels.

The apparent modulus of elasticity and peak compressive strength of the printed gyroids are listed in Table 4. By comparing other TPMS lattice structures, it was noted that the mechanical properties are highly related to the relative density. For example, Maszybrocka et al.[25] printed TPMS lattice structures (Schwartz diamonds) with a relative density between 34–60%. The printed structures showed an apparent modulus of elasticity between 3.1–12.9 GPa and a compressive strength ranging from 62–200 MPa. Moreover, the effect of using Ti6Al4V gyroid sheets lattice structures was investigated by Yang et al.[44]; they obtained an apparent modulus of elasticity between 0.5–15 GPa and a compressive strength between 21.7–338 MPa. In addition, the electron beam melting (EBM) process was used to print gyroid lattice structures[45] with relative density around 20%; the apparent modulus of elasticity and compressive strength were found to be 1 GPa and 20 MPa, respectively. Depending on the requirements of the implant and its position in the body, the right choice of relative density, apparent modulus of elasticity and compressive strength can be determined. The mechanical properties of as-built SLM parts can be improved

through post-processing operations such as sandblasting[46] and solution heat treatment[47].

Table 4-4: Apparent modulus of elasticity and compressive strength of the gyroid parts at different VED levels.

VED (J/mm ³)	Apparent modulus of elasticity (GPa)	Compressive strength (MPa)
43	1.61±0.17	46.34± 2.34
103	2.63±0.32	73.45±0.67
193	5.34±25	127.54±1.11

The FEA model was developed to predict the mechanical properties of the printed gyroids.

The FEA results were compared to the gyroid parts printed at the VED level of 103 J/mm³ since these parts had the closest relative density to the design value. The results of the numerical analysis are in agreement with the experimental ones and illustrated in

Figure 4-11; an error of 10% is found between the results. The material model might be one of the factors contributing to the difference between the FEA model and the experimental results. Most of the material models used right now in the literature are adopted from materials manufactured by forging or casting. Very limited work focuses on obtaining the material model based on SLM-fabricated Ti6Al4V. Another factor contributing to the difference is that the model size was finite; infinite models would give more accurate results but are computationally expensive. Finally, more studies need to be done on voxel meshing and comparing it to tetrahedral meshes to evaluate which represents the material and lattice geometries in more depth. Moreover, the internal defects were not accounted for in this model. In our future studies, the internal defects and more appropriate

material models representing the printed Ti6Al4V material will be adopted to enhance the accuracy of the developed model.

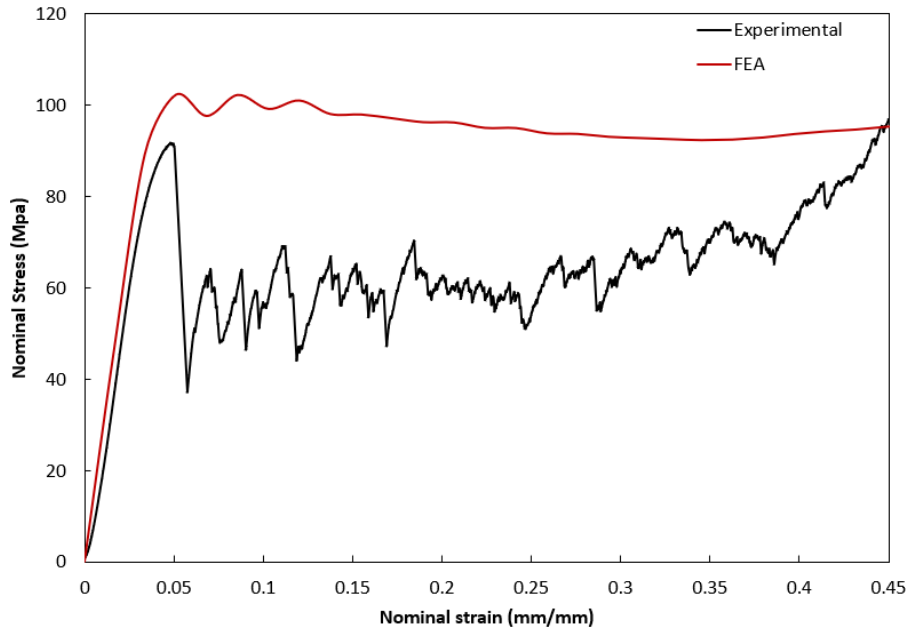


Figure 4-11: Experimental versus FEA stress-strain diagram for gyroid parts.

4.4 Conclusions

In this work, the effects of three VED levels (43, 103, and 192 J/mm³) on the microstructure, internal porosities, and mechanical properties of the SLM fabricated Ti6Al4V gyroid lattice structures have been studied. The energy levels have been chosen carefully from the literature to cover different varieties and widen the research scope. The main conclusions are as follows:

1. The VED levels included in this study had no significant effect on the microstructure of the printed gyroid lattice structures. The expected martensitic structure is related to the fast cooling rate of the SLM process.

2. The relative density and strut size are related to the amount of VED provided to the powder. VED level of 43 J/mm^3 was found to be insufficient, based on the incomplete struts observed. At a VED of 192 J/mm^3 , the measured apparent density was doubled compared to the design value; this is related to the oversized melt pool geometry.

3. The gyroid lattice structures printed at VED of 192 J/mm^3 had the highest internal porosities reaching 2.1% as well as the highest frequency of irregular pores. These irregularly shaped porosities are usually attributed to the keyhole formation due to both the high laser power and VED level.

4. The lattice structures fabricated at VED level of 192 J/mm^3 showed the highest apparent modulus of elasticity and compressive strength, due to the thickest strut size and greatest apparent density of the parts printed at that VED level. These parts also have the least elastic strain, due to the presence of the highest frequency of internal defects. These defects act as stress concentrators and facilitate crack initiation.

Future work would include the update of the material model to mimic the properties of printed Ti6Al4V. Moreover, the inclusion of internal defects in the FEA model would help in obtaining more accurate results and reduce the difference between the numerical and experimental work.

4.5 References

- [1] L.-C. Zhang and L.-Y. Chen, “A Review on Biomedical Titanium Alloys: Recent Progress and Prospect,” *Adv. Eng. Mater.*, vol. 21, pp. 1801215–1801244, 2019.
- [2] M. Z. Harun WS, Kamariah MS, Muhamad N, Ghani SA, Ahmad F, “A review of

- powder additive manufacturing processes for metallic biomaterials,” *Powder Technol.*, vol. 327, pp. 128–151, Mar. 2018.
- [3] L.-C. Zhang and H. Attar, “Selective Laser Melting of Titanium Alloys and Titanium Matrix Composites for Biomedical Applications: A Review,” *Adv. Eng. Mater.*, vol. 18, no. 4, pp. 463–475, Apr. 2016.
- [4] D. Mahmoud and M. Elbestawi, “Lattice Structures and Functionally Graded Materials Applications in Additive Manufacturing of Orthopedic Implants: A Review,” *J. Manuf. Mater. Process.*, vol. 1, no. 2, p. 13, Oct. 2017.
- [5] T. D. Shipley H, McDonnell D, Culleton M, Coull R, Lupoi R, O’Donnell G, “Optimisation of process parameters to address fundamental challenges during selective laser melting of Ti-6Al-4V: A review,” *Int. J. Mach. Tools Manuf.*, vol. 128, no. January, pp. 1–20, 2018.
- [6] H. Gong, K. Rafi, H. Gu, G. D. Janaki Ram, T. Starr, and B. Stucker, “Influence of defects on mechanical properties of Ti-6Al-4V components produced by selective laser melting and electron beam melting,” *Mater. Des.*, vol. 86, pp. 545–554, Dec. 2015.
- [7] X. Zhao *et al.*, “Comparison of the microstructures and mechanical properties of Ti-6Al-4V fabricated by selective laser melting and electron beam melting,” *Jmade*, vol. 95, no. April, pp. 21–31, 2015.
- [8] H. Gong, K. Rafi, H. Gu, T. Starr, and B. Stucker, “Analysis of defect generation in Ti-6Al-4V parts made using powder bed fusion additive manufacturing processes,” *Addit. Manuf.*, vol. 1, pp. 87–98, 2014.
- [9] J. Heang Kuan Tan, S. Leong Sing, and W. Yee Yeong, “Microstructure modelling for metallic additive manufacturing: a review,” 2020.
- [10] J. Ciurana, L. Hernandez, and J. Delgado, “Energy density analysis on single tracks formed by selective laser melting with CoCrMo powder material.”
- [11] G. Kasperovich, J. Haubrich, J. Gussone, and G. Requena, “Correlation between porosity and processing parameters in TiAl6V4 produced by selective laser melting,” *Mater. Des.*, vol. 105, pp. 160–170, 2016.
- [12] S. Pal *et al.*, “Tensile properties of selective laser melting products affected by building orientation and energy density,” *Mater. Sci. Eng. A*, vol. 743, pp. 637–647, Jan. 2019.
- [13] J. Yang *et al.*, “Role of molten pool mode on formability, microstructure and mechanical properties of selective laser melted Ti-6Al-4V alloy,” *Mater. Des.*, vol. 110, pp. 558–570, Nov. 2016.
- [14] J. Reijonen, A. Revuelta, T. Riipinen, K. Ruusuvoori, and P. Puukko, “On the effect of shielding gas flow on porosity and melt pool geometry in laser powder bed fusion additive manufacturing,” *Addit. Manuf.*, vol. 32, Mar. 2020.
- [15] J. Pegues *et al.*, “Effect of Process Parameter Variation on Microstructure and Mechanical Properties of Additively Manufactured Ti-6Al-4V.”

- [16] O. Rehme and C. Emmelmann, “Rapid manufacturing of lattice structures with selective laser melting,” *Laser-based Micropackaging. Int. Soc. Opt. Photonics*, vol. 6107, no. February 2006, p. 61070K, Feb. 2006.
- [17] S. L. Sing, F. E. Wiria, and W. Y. Yeong, “Selective laser melting of lattice structures: A statistical approach to manufacturability and mechanical behavior,” *Robot. Comput. Integr. Manuf.*, vol. 49, no. January 2017, pp. 170–180, 2018.
- [18] Z. A. Ahmadi SM, Hedayati R, Jain RA, Li Y, Leeflang S, “Effects of laser processing parameters on the mechanical properties, topology, and microstructure of additively manufactured porous metallic biomaterials: A vector-based approach,” *Mater. Des.*, vol. 134, pp. 234–243, 2017.
- [19] H. Liang *et al.*, “The size effect on forming quality of Ti–6Al–4V solid struts fabricated via laser powder bed fusion,” *Metals (Basel)*, vol. 9, no. 4, Apr. 2019.
- [20] O. Al-Ketan, D. W. Lee, R. Rowshan, and R. K. Abu Al-Rub, “Functionally graded and multi-morphology sheet TPMS lattices: Design, manufacturing, and mechanical properties,” *J. Mech. Behav. Biomed. Mater.*, vol. 102, Feb. 2020.
- [21] L. Li *et al.*, “Early osteointegration evaluation of porous Ti6Al4V scaffolds designed based on triply periodic minimal surface models,” *J. Orthop. Transl.*, vol. 19, pp. 94–105, Oct. 2019.
- [22] Z. Cai, Z. Liu, X. Hu, H. Kuang, and J. Zhai, “The effect of porosity on the mechanical properties of 3D-printed triply periodic minimal surface (TPMS) bioscaffold,” *Bio-Design Manuf.*, vol. 2, pp. 242–255, 2019.
- [23] C. Peng and P. Tran, “Bioinspired functionally graded gyroid sandwich panel subjected to impulsive loadings,” *Compos. Part B Eng.*, p. 107773, 2020.
- [24] L. Yang *et al.*, “An investigation into the effect of gradients on the manufacturing fidelity of triply periodic minimal surface structures with graded density fabricated by selective laser melting,” *J. Mater. Process. Technol.*, vol. 275, Jan. 2020.
- [25] J. Maszybrocka, B. Gapiński, M. Dworak, G. Skrabalak, and A. Stwora, “The manufacturability and compression properties of the Schwarz Diamond type Ti6Al4V cellular lattice fabricated by selective laser melting.”
- [26] “<http://www.msri.org/publications/sgp/jim/papers/morphbysymmetry/table/index.html>.”
- [27] A. Yáñez, A. Herrera, O. Martel, D. Monopoli, and H. Afonso, “Compressive behaviour of gyroid lattice structures for human cancellous bone implant applications,” *Mater. Sci. Eng. C*, vol. 68, pp. 445–448, 2016.
- [28] A. G. Demir, P. Colombo, and B. Previtali, “From pulsed to continuous wave emission in SLM with contemporary fiber laser sources: effect of temporal and spatial pulse overlap in part quality,” *Int. J. Adv. Manuf. Technol.*, vol. 91, no. 5–8, pp. 2701–2714, 2017.
- [29] S. LE Karimi P, Raza T, Andersson J, “Influence of laser exposure time and point

- distance on 75- μ m-thick layer of selective laser melted Alloy 718,” *Int. J. Adv. Manuf. Technol.*, vol. 94, no. 5–8, pp. 2199–2207, Feb. 2018.
- [30] and R. K. Cain, Victoria, Lore Thijs, Jan Van Humbeeck, Brecht Van Hooreweder, “Crack propagation and fracture toughness of Ti6Al4V alloy produced by selective laser melting,” *Addit. Manuf.*, vol. 5, pp. 68–76, Jan. 2015.
- [31] M. Babich and V. Kublanov, “Voxel Based Finite Element Method Modelling Framework for Electrical Stimulation Applications Using Open Source Software,” in *Proceedings - 2019 Ural Symposium on Biomedical Engineering, Radioelectronics and Information Technology, USBEREIT 2019*, 2019, pp. 127–130.
- [32] Q. Mao, K. Su, Y. Zhou, M. Hossaini-Zadeh, G. S. Lewis, and J. Du, “Voxel-based micro-finite element analysis of dental implants in a human cadaveric mandible: Tissue modulus assignment and sensitivity analyses,” *J. Mech. Behav. Biomed. Mater.*, vol. 94, pp. 229–237, Jun. 2019.
- [33] H. Mehboob, F. Tarlochan, A. Mehboob, and S. H. Chang, “Finite element modelling and characterization of 3D cellular microstructures for the design of a cementless biomimetic porous hip stem,” *Mater. Des.*, vol. 149, pp. 101–112, Jul. 2018.
- [34] F. J. Quevedo González and N. Nuño, “Finite element modelling approaches for well-ordered porous metallic materials for orthopaedic applications: cost effectiveness and geometrical considerations,” *Comput. Methods Biomech. Biomed. Engin.*, vol. 19, no. 8, pp. 845–854, 2016.
- [35] D. K. Do and P. Li, “The effect of laser energy input on the microstructure, physical and mechanical properties of Ti-6Al-4V alloys by selective laser melting,” *Virtual Phys. Prototyp.*, vol. 11, no. 1, pp. 41–47, Jan. 2016.
- [36] J. Yang, H. Yu, J. Yin, M. Gao, Z. Wang, and X. Zeng, “Formation and control of martensite in Ti-6Al-4V alloy produced by selective laser melting,” *Mater. Des.*, vol. 108, pp. 308–318, Oct. 2016.
- [37] E. Sallica-Leva, R. Caram, A. L. Jardini, and J. B. Fogagnolo, “Ductility improvement due to martensite α' decomposition in porous Ti-6Al-4V parts produced by selective laser melting for orthopedic implants,” *J. Mech. Behav. Biomed. Mater.*, vol. 54, pp. 149–158, Feb. 2016.
- [38] S. Tamas-Williams, H. Zhao, F. Léonard, F. Derguti, I. Todd, and P. B. Prangnell, “XCT analysis of the influence of melt strategies on defect population in Ti-6Al-4V components manufactured by Selective Electron Beam Melting,” *Mater. Charact.*, vol. 102, pp. 47–61, 2015.
- [39] G. Ziółkowski, E. Chlebus, P. Szymczyk, and J. Kurzac, “Application of X-ray CT method for discontinuity and porosity detection in 316L stainless steel parts produced with SLM technology,” *Arch. Civ. Mech. Eng.*, vol. 14, no. 4, pp. 608–614, 2014.
- [40] T. Vilaro, C. Colin, and J. D. Bartout, “As-Fabricated and Heat-Treated

- Microstructures of the Ti-6Al-4V Alloy Processed by Selective Laser Melting,” *Metall. Mater. Trans. A*, vol. 42, no. 10, pp. 3190–3199, Oct. 2011.
- [41] I. Maskery *et al.*, “Quantification and characterisation of porosity in selectively laser melted Al-Si10-Mg using X-ray computed tomography,” *Mater. Charact.*, vol. 111, pp. 193–204, 2016.
- [42] R. Cunningham *et al.*, “Keyhole threshold and morphology in laser melting revealed by ultrahigh-speed x-ray imaging,” *Science (80-.)*, vol. 363, no. 6429, pp. 849–852, 2019.
- [43] D. Mahmoud, M. A. Elbestawi, and B. Yu, “Process–Structure–Property Relationships in Selective Laser Melting of Porosity Graded Gyroids,” *J. Med. Device.*, vol. 13, no. 3, p. 31005, Jul. 2019.
- [44] E. Yang *et al.*, “Effect of geometry on the mechanical properties of Ti-6Al-4V Gyroid structures fabricated via SLM: A numerical study,” *Mater. Des.*, vol. 184, Dec. 2019.
- [45] A. Ataei, Y. Li, D. Fraser, G. Song, and C. Wen, “Anisotropic Ti-6Al-4V gyroid scaffolds manufactured by electron beam melting (EBM) for bone implant applications,” *Mater. Des.*, vol. 137, pp. 345–354, Jan. 2018.
- [46] L. Yang *et al.*, “Compression–compression fatigue behaviour of gyroid-type triply periodic minimal surface porous structures fabricated by selective laser melting,” *Acta Mater.*, vol. 181, pp. 49–66, Dec. 2019.
- [47] S. L. Sing, S. Huang, and W. Y. Yeong, “Effect of solution heat treatment on microstructure and mechanical properties of laser powder bed fusion produced cobalt-28chromium-6molybdenum,” *Mater. Sci. Eng. A*, vol. 769, Jan. 2020.

Chapter 5

Process-structure-property relationships in selective laser melting of porosity graded gyroids

Complete Citation:

Mahmoud, Dalia, M. A. Elbestawi, and Bosco Yu. "Process–Structure–Property Relationships in Selective Laser Melting of Porosity Graded Gyroids." *Journal of Medical Devices* 13.3 (2019). doi.org/10.1115/1.4043736

Copyright:

© 2019 ASME Publishing

Relative Contributions:

Dalia Mahmoud: Performed experiments, analysis, and data interpretation. Wrote the first draft of the manuscript.

M. A. Elbestawi: Revised and edited the manuscript.

Bosco Yu: Revised the mechanical analysis and interpretation.

Abstract:

Selective laser melting (SLM) can be used to tailor both the geometry and mechanical properties of lattice structures to match bone properties. In this work, a process-structure-property (PSP) relationship for porosity graded gyroids (PGGs) structures was developed. A design of experiment (DOE) approach was used to test the significance and contribution of different process parameters on microstructure, morphology, and mechanical properties. For the proposed design it was noted that higher volumetric energy density (VED) can be used when printing lattice structures as compared to printing bulk parts. Process maps to predict the morphology errors at specific laser power and scan speed were developed. Moreover, the mechanical properties of radially PGGs with a relative density of 25% are evaluated using different SLM process parameters. The results showed that PGGs with different radial gradation designs have mechanical properties that are compatible with bone implants: apparent compressive modulus of 1.4 - 5.3 GPa, and compressive strength 40 - 154 MPa.

Keywords:

Porosity graded gyroids; selective laser melting; process-structure-properties; volumetric energy density; compressive response; design of experiments; bone implants

NOMENCLATURE

SLM	Selective laser melting
PSP	Process structure property
PGGs	Porosity graded gyroids
DOE	Design of experiments

CAD	Computer aided design
TPMS	Triply periodic minimal surface
SEM	Scanning electron microscope
L-PGGs	Linearly porosity graded gyroids
R-PGGs	Radially porosity graded gyroids
VED	Volumetric energy density
P	Laser power
V	Laser scan speed
h	Hatch spacing
t	Layer thickness
$\bar{\rho}_d$	Design relative density
$\bar{\rho}_m$	Measured relative density
$T_b T_h$	Trabecular thickness
$T_b S_p$	Trabecular Spacing
ANOVA	Analysis of variance
RSM	Response surface methodology
D-O	Dense out
D-I	Dense in
N-G	Non-graded

Acknowledgment:

The authors acknowledge the funding of the Natural Sciences and Engineering Research Council of Canada (NSERC; funding reference number 518494).

5.1 Introduction

The ability of selective laser melting (SLM) process to manufacture complicated metallic lattice structures have gained the attention of biomedical researchers [1]. Lattice structures are formed by intentionally creating porosity in bulk materials, controlled by a repetitive building block often referred to as unit cell. These lattice structures are considered a monolithic material with different mechanical properties than the parent material [2]–[5]. SLM process can control the unit cell shape and size, thus it can be used to tailor the mechanical and biological properties of lattice structures to mimic that of bone [6]. Various unit cell shapes and sizes can be printed to cope with the regenerative medicine needs. Databases correlating each unit cell design with its mechanical and biological properties are being created and updated regularly [7]. Therefore, these structures can be used as substitute for defective bones when needed.

The amount of intended porosity of lattice structures dictate the mechanical and biological properties. Large amount of intended porosity enhances the permeability of fluid within the cells, however, might affect their mechanical integrity [8]. Therefore, porosity graded lattice structures have been proposed. The human bone itself is considered porosity graded structure [9], trabecular bone's porosity is between 50-90%, while cortical bone's porosity is around 10 %. Thus, depending on the application and location of bone tissue implants, a specific porosity gradation might be preferred to match the geometry of the bone to be replaced. The porosity gradation is mainly controlled by adjusting the ratio of materials to space in lattice structures. This can be referred to as relative density, relative porosity, or volume fraction. The unit cell shape and strut size are also key parameters that would affect the mechanical and biological properties of lattice structures.

Significant efforts have been made to study the porosity gradation of lattice structures using computer aided design (CAD)-based unit cells, from mechanical and biological point of view [10]–[12]. Energy absorption has been improved by linearly grading the porosity of cubic and honeycomb unit cells [13], however the yield strength of these graded structures was lower than non graded ones [14]. The porosity gradation using 6 different mathematical functions have been proposed by Zhang et al. [15]. Their experimental work revealed that parts graded using linear sigmoid function has superior permeability and structural integrity compared to linear and exponential functions. Radial gradation of metallic lattice structures was suggested by Surmeneva et al. [16], three sub structures with in the implant were designed and characterized using body centred cube (BCC) unit cells. The multilayered designs have stiffness compared to that of bone, but relatively low yield strength that might be related to the non-continuous grading structure.

Another design of unit cells named triply periodic minimal surfaces (TPMS), are well studied in the field of tissue implant, due to their high surface area to volume ratio and high permeability [17]. Most importantly its ability to form continuously graded lattice structures, without interruption between different volume fractions across the scaffold [18]. A novel method to grade the porosity of TPMS unit cells was proposed by gradually changing the cell size in a linear direction [19]. Another unique method suggested by the same authors is creating heterostructure from two different TPMS unit cell shapes namely diamond and gyroid structures. The proposed design had mechanical properties that mimic bone's properties, however, the pore sizes suggested by the authors were too large for bone cell attachment applications.

Some efforts have been made to optimize the SLM process parameters for CAD based unit cells lattice structures [20]–[23]. However, the effect of SLM process parameters on the

manufacturability of TPMS porosity graded lattice structures is not often considered. The main purpose of this work is to identify the most suitable set of process parameters to use while printing porosity graded gyroids (PGGs). By relating the SLM controllable process parameters with the microstructure/morphology, the mechanical properties can be predicted. This can be referred to as evaluation of the process-property-structure (PSP) relationship for those structures. The main focus of this study is to evaluate the root cause of defects and avoid them while 3D printing lattice structures. Moreover, grading the porosity in radial direction is suggested, the apparent compressive modulus, compressive peak strength and failure modes are studied.

5.1 Experimental procedure

5.1.1 Materials: Alloy powders

Titanium alloys are known for their unmatched biocompatibility, osseointegration and high corrosive resistance, making them favorable for biomedical applications [24]. Figure 5-1 shows a Scanning Electron Microscope (SEM) image for the powder used in this study, the Ti6Al4V powder exhibits a nearly spherical shape and relatively smooth surface. The average particle size according to the manufacturer is 45 μm , the chemical composition is given in Table 5-1.

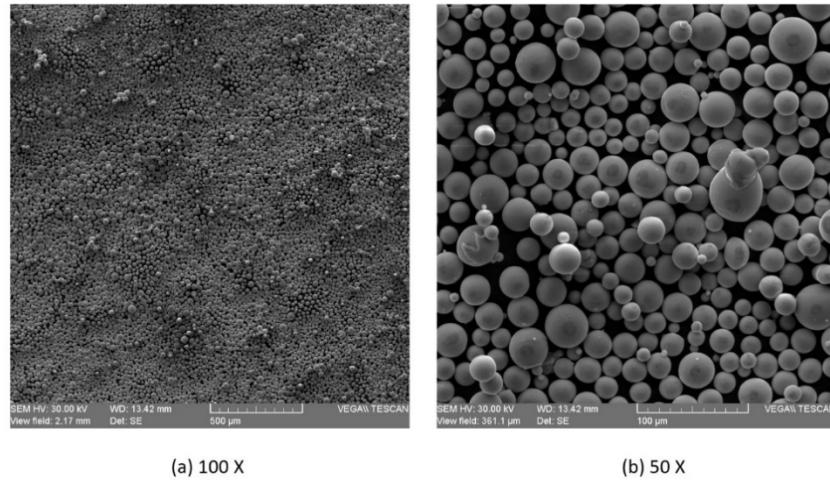


Figure 5-1: SEM images showing the starting Ti6Al4V powder shape and morphology (a) 100 x magnification (b) at 50 x magnification.

Table 5-1: Element composition of used Ti6Al4V powder.

Element	Ti	Al	V	Fe	O	C	N	H	Residuals
Mass %	Balance	5.5- 6.5	3.5- 4.5	≤0.25	≤0.13	≤0.08	≤0.05	≤0.012	≤0.10 each ≤0.40 total

5.1.2 Lattice design

The gyroid unit cells are known for relatively good mechanical and biological properties, compared to other TPMS unit cells [25], [26]. Gyroid surfaces are biomimetic shapes that have no symmetry planes nor straight lines [27]. This makes them appropriate for tissue scaffolding. Their shape allows adequate nutrient supply as well as large surface area for bone cell attachment [28]. In this study, Matlab[®] was used to design the surfaces of PGGs, the surface of gyroids can be defined by the following equation:

$$\sin(x) \cos(y) + \sin(y) \cos(z) + \sin(z) \cos(x) = c \quad \text{Equation}$$

5-1

where x , y and z are the coordinate system illustrated in Figure 5-2 “ c ” is known as the level constant defines the volume fraction of the surface. By adding a linear term to the equation, the porosity can be graded in x , y and z directions, or all three together.

In our previous work [29] a permissible design gyroids map was developed, the appropriate pores and strut size for bone implant applications were identified. Therefore, linearly porosity graded gyroids (L-PGGs) having relative density (ρ_d) gradation from 50-20% were printed as illustrated in Figure 5-2. A base of 3 mm was printed to support the lattice structures, this was used in labeling parts to differentiate between parts printed with different process parameters. Each L-PGGs was designed to have 10 layers, the first layer had a $\bar{\rho}_d$ of 50% (50% intended porosity), while the last layer was designed to have ρ_d of 20% (80% intended porosity). The size of each unit cell was kept constant at 1 mm, while the change in designed porosity was obtained by changing the pore and strut size along the z direction in a continuous manner, as shown in Figure 5-2.

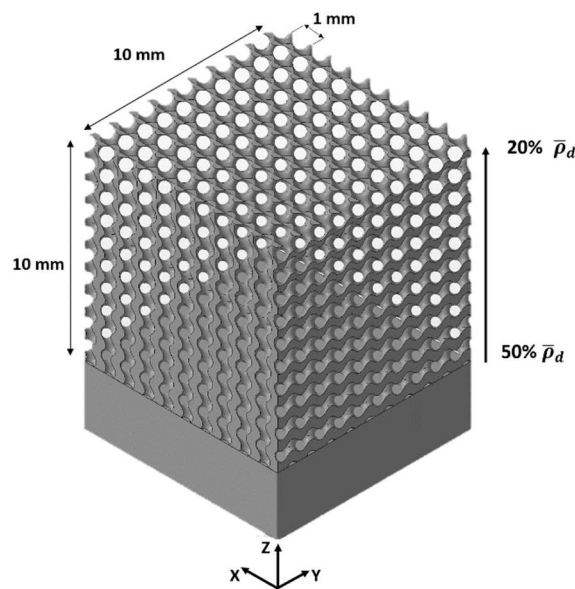


Figure 5-2: Linearly porosity graded gyroids (L-PGGs) samples.

5.1.3 Selective laser melting

The first component of PSP (process-structure-property) relationship would be identified by understanding the SLM process parameters. SLM has more than 50 controllable process parameters [30]. The most significant parameters that affect the defects formation are those involved in defining the volumetric energy density (VED). This is the energy absorbed by a unit volume of the powder. As the powder starts gaining this energy, it reaches the melting temperature and forms what is known as melt pool. The VED can be calculated from the main process parameters: laser power (P), scan speed (V), hatch spacing (h), and layer thickness (t) as given in equation 2. The energy input affects the melt pool geometry, solidification rate, microstructure, and dimensional accuracy of printed parts [31]. Moreover, improper amount of energy would result in internal defects which would affect the mechanical properties as well. One of the challenges of SLM is to find the appropriate process window to print the parts with the highest quality characteristics [32].

$$VED = \frac{P}{v.t.h} \quad \text{Equation 5-2}$$

The PGGs were printed using a Renishaw M400 machine. A design of experiment (DOE) was created to determine a suitable set of process parameters and to test the manufacturability of these structures. The factors considered were P, V and design relative density (ρ_d), 3 levels at each factor. The design illustrated in Figure 5-2 was printed 9 times at different values of P and V. The VED used for each part was calculated and presented in Table 5-2. The layer thickness (t) was kept constant at 30 μm since it is known to mainly affect the stair step error [33]. Hatch spacing (h) is also known to affect internal porosity and was kept constant at 85 μm [20]. To test the manufacturability among different lattice layers, three different layers of the PGGs were also assessed at each experiment

(lower, middle, and upper). The considered levels of the third factor ρ_d are 20, 35, 50 %. Samples were separated from the build plate using a bench-saw, then ultrasonically cleaned using ethyl ethanol for 20 minutes.

Table 5-2: SLM Process parameters with the calculates VED in each case.

L-PGGs	1	2	3	4	5	6	7	8	9
P (W)	100	100	100	200	200	200	300	300	300
V (mm/s)	800	1000	1200	800	1000	1200	800	1000	1200
VED (J/mm ³)	64	51	42	128	102	85	192	153	128

5.1.4 Characterization

5.1.4.1 Microstructure and morphology

Characterizing the microstructure and the morphology of the printed PGGs would cover the second part of the PSP relationship. The measured relative densities (ρ_m) were obtained by Archimedes method, using acetone instead of water for better penetration of the printed parts. Each measurement was repeated three times. The calculations for the printed base were taken into consideration. A micro computed tomography (x-CT) was used to reconstruct the printed L-PGGs, with a voxel size of $8.4 \mu m^3$ obtained at 100 KV using Al/Cu filter. Each layer was reconstructed separately, and the ρ_m and strut sizes were measured using CTAn software (SkyScan software). The ρ_m was obtained by calculating bone volume to total volume (BV/TV). while the strut size ($T_b T_h$) and pore size ($T_b S_p$) were evaluated manually from 2D scanned images of the PGGs similar to morphology analysis done previously by Plessis et al.[25]. Scanning electron microscope (SEM) was used to evaluate the morphology of the PGGs. Samples were sectioned, mounted, mechanically polished, and etched (0.5HF, 5HNO₃, 94.5 H₂O) for optical microscopic evaluation.

5.1.4.2 Mechanical Properties

The third and last part of the PSP relationship is the mechanical properties characterization. Microhardness measurements were carried out using a Clemex Microhardness Tester with a 100 N (10 Kgf) for 10 s. Furthermore, to test the applicability of the porosity graded designs to replicate parts of the trabecular bone a radial porosity gradation design is suggested. Uniaxial compression tests were carried out using a strain rate of 0.001 mm/s on a 50 KN Instron machine according to the ISO 13314 standard [34]. To make sure the displacement measurements were consistent, the machine compliance was subtracted from the crosshead displacement. The apparent compressive modulus E_{app} was calculated from the slope of the elastic part of the nominal stress-strain curve. While the peak strength σ_p was calculated from the highest nominal stress reached before the first load drop. For each test group 3 samples were tested, and the mean value was calculated for accuracy. Additionally, the compression tests were recorded using a video camera to capture failure modes.

5.2 Results and discussion

5.2.1 Microstructure and microhardness

Due to the fast cooling nature and high temperature gradients of the SLM process, the expected microstructure of the printed PGGs is acicular martensitic one. The fast cooling rates (10^3 - 10^8 K/s) results in the transformation of β phase to α' , similar to conventional water quenching mechanism. Figure 5-3 shows the microstructures of the PGGs, it was observed that the majority of the structure is needle shaped α' . It is clear that prior β grains grow perpendicular to the build plate. Some defects such as lack of fusion and entrapped porosities were noticed as indicated in Figure 5-3. Lack of fusion might be attributed to

insufficient amount of VED, thus consecutive layers fail to bond. While the entrapped porosity is usually attributed to the entrapped gas between the powder metal due to low packing density or gas entrapped in the powder particles when they were manufactured. The porosities can also be attributed to gas bubbles generated from high laser energy applied to the powder [35]. No major differences in microstructure features were detected across the length of the printed parts, which agrees with the findings of Murr et al. [36]. According to the ISO 20160 standard [37], metallic implants should have a homogenous equiaxial microstructure to improve the mechanical integrity. Therefore, consecutive heat treatments might be necessary for the graded lattice implants printed by SLM.



Figure 5-3: Microstructural analysis (a) L-PGGs-3- VED = 42.735 J/mm³ lack of fusion indicated by arrow, (b) L-PGGs 6- VED= 85.47 J/mm³, and (c) L-PGGs 7- VED=192.31 J/mm³ internal porosities indicated by arrows , scale bar is 50 μ m.

Microhardness results for the printed samples are illustrated by Figure 5-4. The results are consistent with the microhardness results found in the literature [38]. An average variation of 50 HV was observed, L-PGGs printed with higher VED (192 J/mm³) had relatively higher hardness than the ones printed with lower VED (43 J/mm³). Variation within each sample was in the order of 20 HV, these variations are attributed to the fact that the average area of indentation contains α' within β matrix. The amount of α' and distribution might be different in each indentation. Moreover, parts printed with lower VED may contain

layers that are not fused together, which result in lower hardness due to the internal defects. It was noted that the microhardness variation is not significant within the tested VED window. Further analysis of the α' length and width might give insight on the relationship between the VED and α' content and microhardness.

The variation in morphology is discussed in the next section, which is thought to play a key role in mechanical properties characterization.

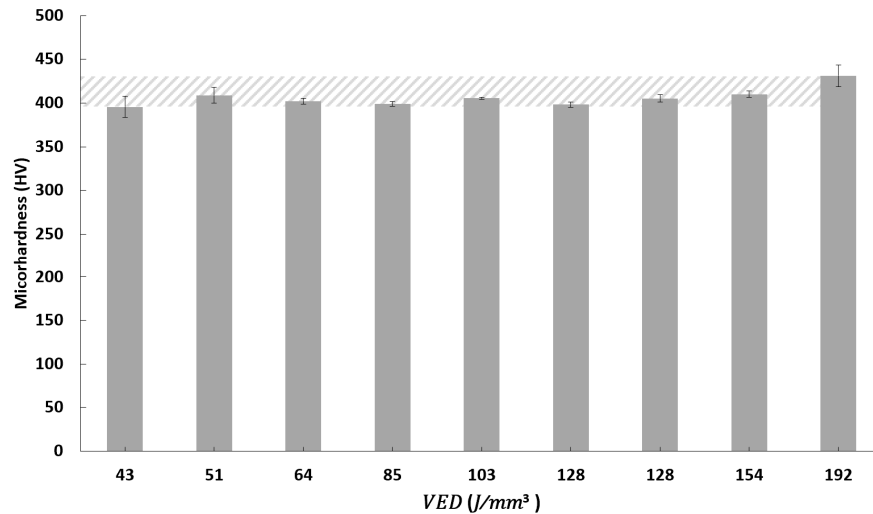


Figure 5-4: Microhardness results for L-PGGs printed with different VED.

5.2.2 Morphology

5.2.2.1 Effect of energy density on part morphology

The increase in VED is accompanied by an increase in the energy delivered to the powder. As the powder starts to absorb this energy, its temperature increases and starts forming a melt pool. The melt pool dimension would affect the dimensional accuracy of the parts printed by SLM [33]. Figure 5-5 illustrates the SEM images of the L-PGGs parts printed with different VED. The part printed using VED of $42 J/mm^3$, has relatively thin struts and

can be characterized with melt pools solidified on top of each other. Sometimes referred to as balling phenomena or melt pool spheroidization due to insufficient amount of VED [39], indicating there is not enough energy to maintain a continuously melted track. On the other hand, parts printed with VED of 192 J/mm^3 , are characterized with excessive amount of partially melted powder. Moreover, due to the high amount of energy, dripping of some of the melt pools occurs that lead to distorting the geometry of the PGGs. The parts printed with VED of 85 J/mm^3 appears to maintain better geometrical accuracy. Quantitative analysis of strut sizes and volume fraction of each layer is therefore necessary to accurately compare between the various VED used in this work.

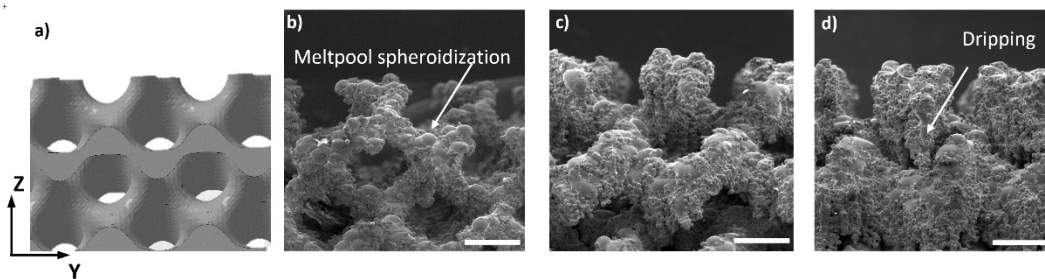


Figure 5-5: SEM images of L-PGGs printed at different VED (a) STL file (b) L-PGGs-3- VED= 42.735 J/mm^3 (c) L-PGGs-6- VED= 85.47 J/mm^3 , (d) L-PGGs-7- VED = 192.31 J/mm^3 , scale bar = $500 \mu\text{m}$.

The errors in $T_b T_h$ were evaluated by subtracting the design value from the $T_b T_h$ measured from x-CT scans. To relate this error with the strut size, the relative errors were evaluated by dividing the error value by the design value. 10 different measurements were obtained at different locations to increase reliability of results. The relative errors in the strut sizes were in the range of $\pm 20 \%$ for the different printed samples. An increase in $T_b T_h$ was observed with the increase in VED, consequently, an increase in the ρ_m was also detected.

The relative errors in $T_b T_h$ and ρ_m are demonstrated in Figure 5-6. These findings agree with the findings of Tsopanos et al [40] and Sing et al.[23].

Part of this work is to define the most suitable VED to be used for printing these type of lattice structures. By plotting the relative errors in both $T_b T_h$ and ρ_m , the most suitable VED window -that minimizes errors- was defined to be between 88 J/mm³ and 103 J/mm³. Compared to the optimized VED for printing solid parts on the same SLM machine, this VED window was found to be higher [41]. The reason for choosing higher VED is that it might be more suitable to print the strut sizes oversized, that could be removed later using post processing treatments, rather than printing them undersized.

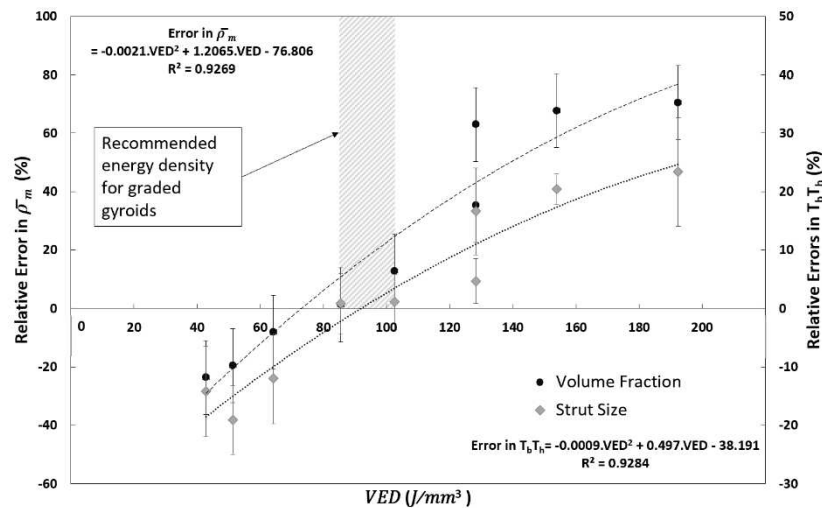


Figure 5-6: Recommended VED for PGGs printed by SLM.

5.2.2.2 Laser Power, Scan Speed, porosity grading effect

Since the VED depends on the P and V, statistical analysis was used to determine the most significant factor affecting the relative error in volume fraction and strut size. Moreover, the ability of SLM process to maintain the same level of accuracy while printing porous graded structures needs to be investigated. Therefore, the change in ρ_d of each layer was

taken into consideration as well as P and V . Figure 5-7 illustrates the main effect of each factor on the relative errors in $T_b T_h$ and ρ_m . The main effect displays the mean of each factor within a specific level. It was noted that the increase in P lead to increase in strut size and relative density. V and ρ_d , had little or almost no effect on relative errors in the studied SLM process window.

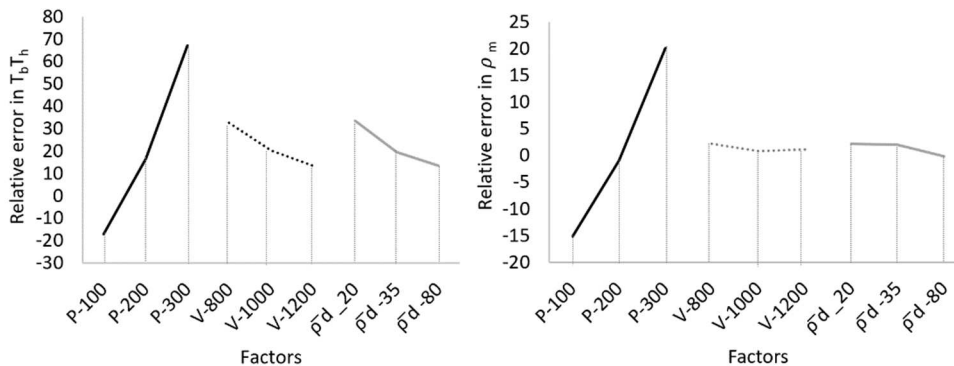


Figure 5-7: Main effects plot for relative error in $T_b T_h$ and ρ_m .

The analysis of variance “ANOVA” is used to clarify which factor is more significant, by comparing the variations between the different factors and within each factor. The ANOVA test results indicates that P is the most significant factor affecting the relative errors in $T_b T_h$ and ρ_m , with a contribution percentage of 75% and 85% respectively. Regression analysis was used to predict the relationship between the errors and the factors, with relatively high co-efficient of determination 87% and 97% respectively. ANOVA results and regression equations are presented in Appendix A . Process maps to predict the relative error percentage in $T_b T_h$ and ρ_m are illustrated in Figure 5-8.

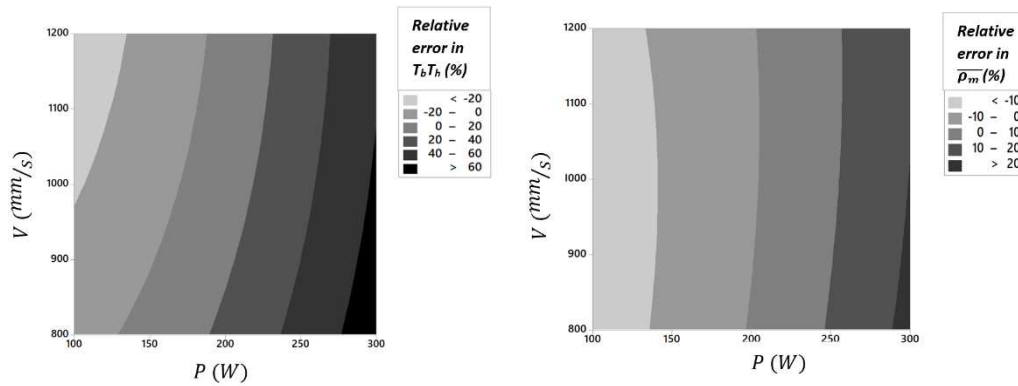


Figure 5-8: Process maps to identify the relative error in strut size and volume fraction.

5.2.3 Mechanical properties

Mechanical behaviour of lattice structures depends on the unit cell shape, relative density, and material properties. The objective is to know what process parameters will result in PGGs with the apparent compressive modulus (E_{app}) and compressive strength σ_p that matches the bone tissue's mechanical properties. Radially porosity graded gyroids (R-PGGs) designs were suggested to match trabecular bone designs, dense-out (D-O) and dense-in (D-I) designs are compared with non-graded (N-G) ones. The length of the compression samples is 21 mm, with a cylindrical cross section of 15 mm diameter. The number of pores and ratio of pores to diameter and length were chosen according to the ISO 13314 standard. Figure 5-9 shows the top view of the three proposed designs, all of them were designed to have ρ_d of 25%. The pore sizes and volume fraction of the continuously graded layers are designed to be between 1000-1300 μm . However due to the nature of the process and the partially sintered powders, it is expected that parts printed with VED more than 85 J/mm³ will have smaller pore sizes than the designed ones.

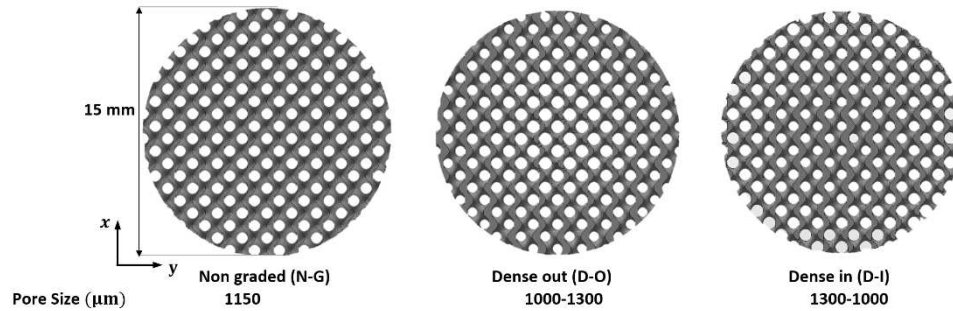


Figure 5-9: Top view of radially PGGs designs.

5.2.3.1 The effect of VED on the mechanical properties

The effect of the SLM process parameters on the mechanical properties of R-PGGs can be investigated using response surface methodology (RSM). An optimal design selection technique was used, 12 samples were printed with different process parameters. The R-PGGs printed at different process parameters along with the estimated E_{app} and σ_p results are listed in Table 5-3. As expected with higher VED, the struts become thicker than the design, therefore the printed parts E_{app} and σ_p increases. The typical stress-strain performance for gyroid lattice structures is shown in Figure 5-10. The graph can be divided into three regions elastic region, plastic/plateau regions and densification region [42], [43].

Table 5-3: Mechanical properties results

Sample	$P(W)$	V (mm/s)	VED (J/mm ³)	Design	$\bar{\rho}_d$ %	$\bar{\rho}_m$ %	E_{app} (GPa)	σ_p (MPa)
1	100	800	43	D-O	0.25	0.17	1.40 ± 0.20	42.90 ± 2.05
2	100	1000	43	D-I	0.25	0.16	1.34 ± 0.01	45.09 ± 0.14
3	100	1200	51	N-G	0.25	0.19	1.58 ± 0.16	45.75 ± 2.86
4	200	800	64	D-O	0.25	0.23	2.00 ± 0.05	63.16 ± 1.13
5	200	1000	85	N-G	0.25	0.28	2.54 ± 0.30	71.23 ± 0.55
6	200	1200	103	D-O	0.25	0.32	3.19 ± 0.22	91.99 ± 0.29
7	300	800	128	D-O	0.25	0.37	3.62 ± 0.35	120.52 ± 8.64
8	300	1000	128	D-I	0.25	0.38	3.69 ± 0.30	97.92 ± 1.62
9	300	1200	128	D-I	0.25	0.37	3.65 ± 0.27	99.89 ± 1.04
10	100	800	128	N-G	0.25	0.39	3.39 ± 0.23	91.01 ± 0.65
11	100	1000	192	D-O	0.25	0.43	5.89 ± 0.18	154.45 ± 6.31
12	100	1200	192	N-G	0.25	0.42	5.14 ± 0.28	128.14 ± 1.00

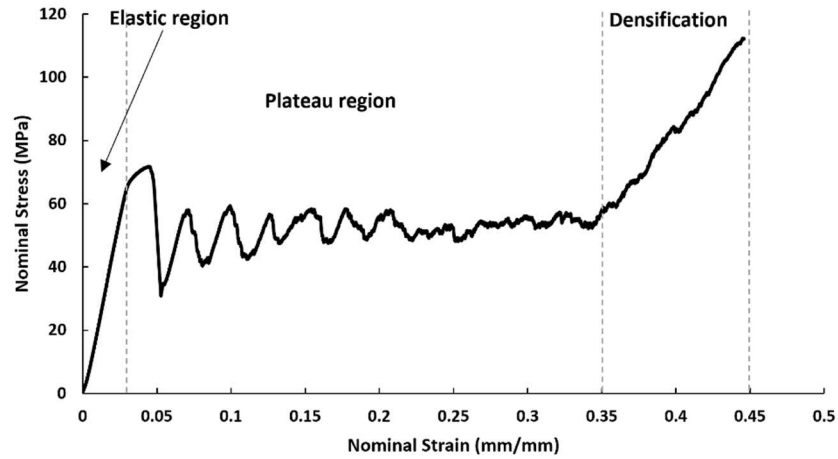


Figure 5-10: Typical stress strain diagram for a 3D printed gyroid lattice

Figure 5-11 compares the mechanical properties of graded and non-graded designs. It should be noted that the three proposed designs as the VED increases the E_{app} and σ_p increases as well. This is attributed mainly to the increase in the $T_b T_h$ and ρ_m . Moreover, as noted earlier the struts printed using the low energy density results in spheroidization of melt pools and lack of fusion cracks, which is expected to have poor bonding and lower strength.

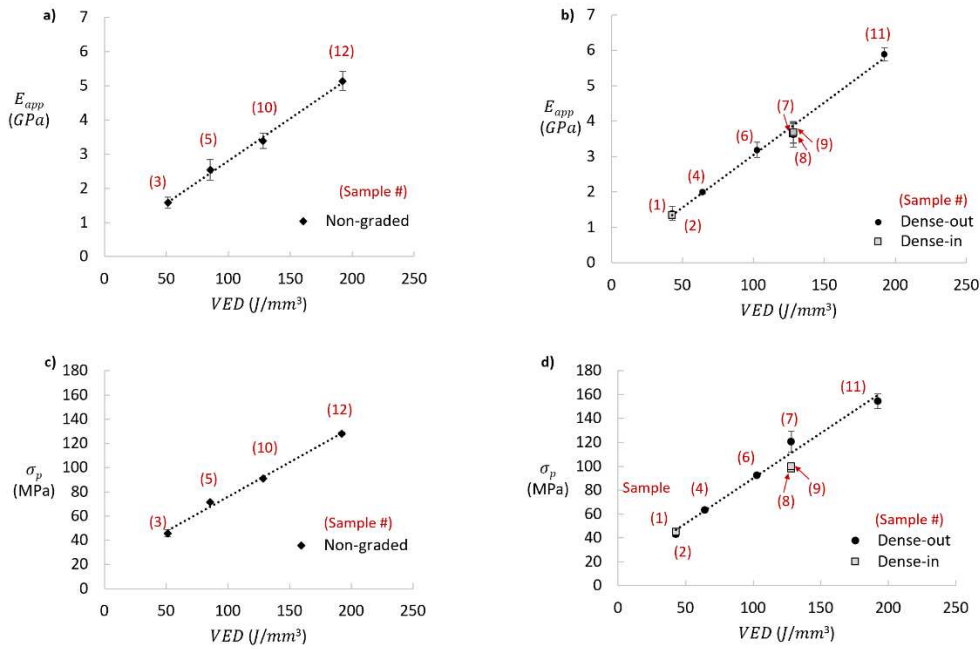


Figure 5-11: E_{app} and σ_p for graded and non-graded PGGs

Figure 5-12 illustrates the difference observed in E_{app} and σ_p among the different designs printed with the same energy density. It was observed that the E_{app} did not change between the three designs. While the σ_p of D-O were significantly higher than the other two designs.

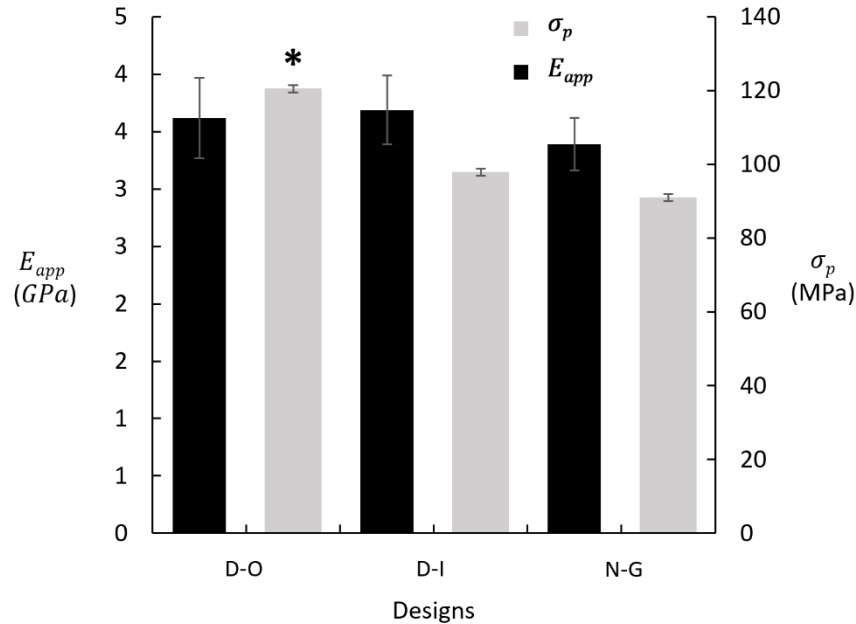


Figure 5-12: Mechanical properties of different R-PGGs designs at same VED.

To understand in more depth the effect of P, V and design on the R-PGGs, the main effects of each factor were calculated. Figure 5-13 illustrates the main effects of each factor, it was noted that E_{app} is highly affected by P and V but not the design. While the σ_p is affected by P and V and the design. The ANOVA test results are attached in Appendix A. The low P values indicate the significance of the factors. The regression equations for each design correlating between E_{app} and σ_p and P and V are illustrated in Appendix A as well. Finally, the process maps that can be used to predict the expected E_{app} and σ_p is plotted in Figure 5-14.

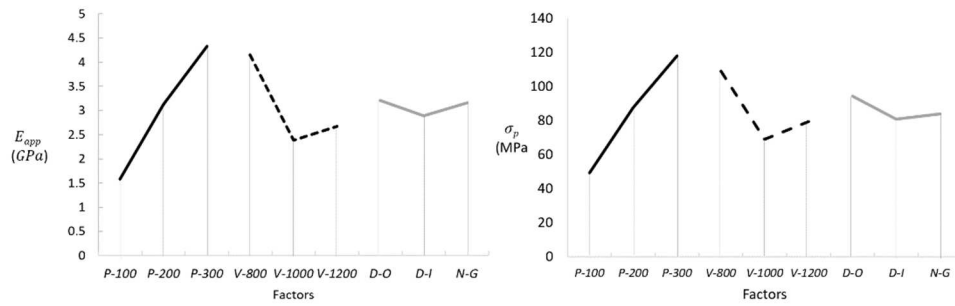


Figure 5-13: Main effect plot for E_{app} and σ_p at different factors

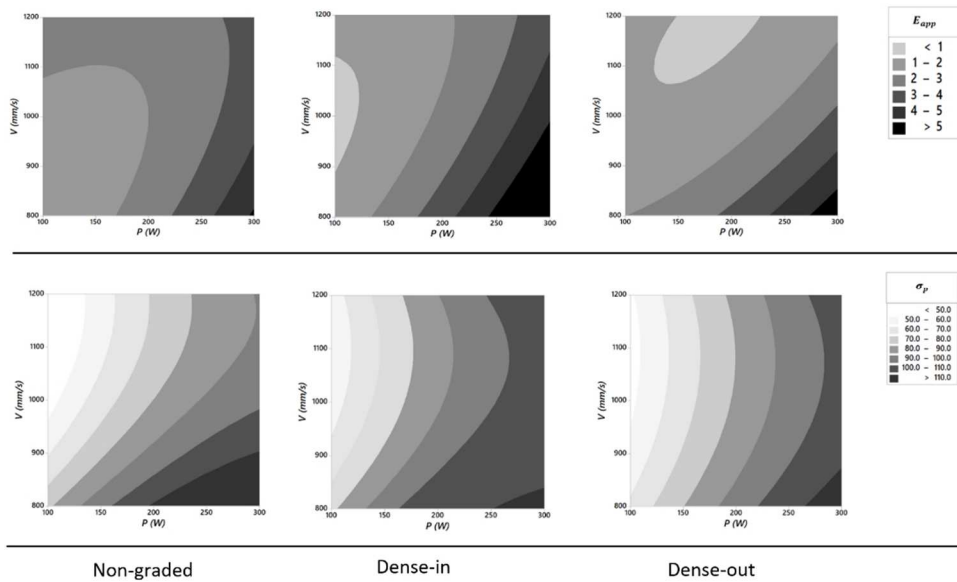


Figure 5-14: Process maps for E_{app} and σ_p of the three R-PGGs designs

5.2.3.2 Failure Mode

Figure 5-15 illustrates the two failure modes observed by the video camera during the uniaxial compression tests. The first mode was layer by layer collapse (crushing) of the PGGs, which was noted for parts printed with $VED = 85 \text{ J/mm}^3$ or lower for the D-O and D-I designs. PGGs having N-G printed with VED below 128 J/mm^3 failed in a layer by layer fashion as well. However, after the above-mentioned values for VED , PGGs failed

by shearing. The crack initiate at the weakest part and a 45-angle crack took place in the PGGs. It was noted that layer by layer failure, results in less struts separation compared to failure by shearing which usually ends up in two or more parts separated from the printed parts.

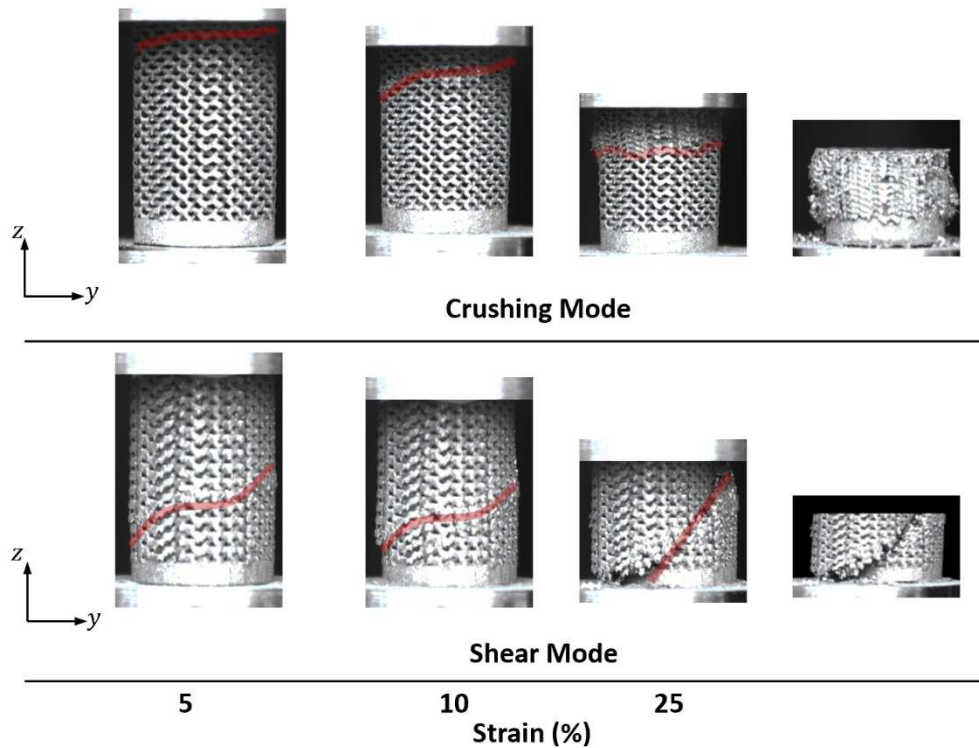


Figure 5-15: Failure modes observed during uniaxial compression tests

From biological point of view, E_{app} of the bone scaffolds should match that of host bone, to avoid the stress shielding phenomena. This phenomenon is associated with the fact that the stiff metal implanted beside the bone will bear most of the load, leaving the bones with decreased load. Bones that are not mechanically stimulated will become thinner or more porous [44]. It is also important to have strength greater than that of the bone to avoid fracture of the metallic scaffolds [45]

5.3 Conclusion

Process-structures-property (PSP) relationship for graded TPMS lattice structures were studied, to assess the manufacturability of those structures for bone implant applications. SLM process was used to successfully print PGGs, with $\bar{\rho}_d$ ranging from 20% to 50% with controlled accuracy. The choice of VED and process parameters window should be selected carefully, to minimize manufacturing errors. Morphology was found to play a critical role in defining the mechanical properties of the graded structures. For the PGGs studied in this work, the following conclusions were made:

1. The strut size increase with the increase in VED, leading to increase in the ρ_m of printed PGGs. This would also increase the E_{app} and σ_p of the PGGs.
2. Although lower VED would result in thinner struts and in some cases lower relative errors in strut size, it might affect the mechanical stability of the structures. That is because the struts printed are a result of multiple spheroidization of melt-pools. These struts are unpreferable since they may contain lack of fused spots and have generally weaker mechanical integrity than struts printed with higher VED.
3. Different radial gradation designs enhance the functionality of bone implants, they have almost the same E_{app} as non-graded structures but can withstand higher strength.
4. Although failure mode is usually associated with the unit cell shape. It was observed that different process parameters would affect the relative density and strut size, which in turn affects the failure mode as well.

With the improved understanding of the influence of SLM process parameters on the manufacturability of PGGs. The next step should be testing the fatigue properties of PGGs

and trying to predict the fatigue life using analytical models. The α' length and width are expected to change with changing the amount of VED used while printing the parts. Therefore, future work will deal with investigating the significance of this change on the mechanical properties of PGGs. Moreover, *in-vitro* and *in-vivo* experiments should be performed to test the biological capabilities of these porosity graded structures.

5.4 References

- [1] X. Wang *et al.*, “Topological design and additive manufacturing of porous metals for bone scaffolds and orthopaedic implants: A review,” *Biomaterials*, vol. 83, no. September, pp. 127–141, 2016.
- [2] M. Ashby, “Designing architected materials,” *Scr. Mater.*, vol. 68, no. 1, pp. 4–7, Jan. 2013.
- [3] A. M. F. Ashby, “The Properties of Foams and Lattices,” *Philos. Trans. R. Soc. A Math. Phys. Eng. Sci.*, vol. 364, no. 1838, pp. 15–30, 2005.
- [4] H. N. G. Wadley, “Multifunctional periodic cellular metals,” in *Philosophical Transactions of the Royal Society A: Mathematical, Physical and Engineering Sciences*, 2005.
- [5] N. A. Fleck, V. S. Deshpande, and M. F. Ashby, “Micro-architected materials: past, present and future,” *Proc. R. Soc. A*, vol. 466, pp. 2495–2516, 2010.
- [6] S. Arabnejad, R. Burnett Johnston, J. A. Pura, B. Singh, M. Tanzer, and D. Pasini, “High-strength porous biomaterials for bone replacement: A strategy to assess the interplay between cell morphology, mechanical properties, bone ingrowth and manufacturing constraints,” *Acta Biomater.*, vol. 30, pp. 345–356, 2016.
- [7] S. M. Giannitelli, D. Accoto, M. Trombetta, and A. Rainer, “Current trends in the design of scaffolds for computer-aided tissue engineering,” *Acta Biomater.*, vol. 10, no. 2, pp. 580–594, 2014.
- [8] H. Montazerian, E. Davoodi, M. Asadi-Eydivand, J. Kadkhodapour, and M. Solati-Hashjin, “Porous scaffold internal architecture design based on minimal surfaces: A compromise between permeability and elastic properties,” *Mater. Des.*, vol. 126, no. April, pp. 98–114, Jul. 2017.
- [9] X. Miao, D. Sun, X. Miao, and D. Sun, “Graded/Gradient Porous Biomaterials,” *Materials (Basel)*, vol. 3, no. 1, pp. 26–47, Dec. 2009.
- [10] L. Wang, J. Kang, C. Sun, D. Li, Y. Cao, and Z. Jin, “Mapping porous microstructures to yield desired mechanical properties for application in 3D printed bone scaffolds and orthopaedic implants,” *Mater. Des.*, vol. 133, pp. 62–68, 2017.

- [11] E. Onal, J. E. Frith, M. Jurg, X. Wu, and A. Molotnikov, “Mechanical properties and in vitro behavior of additively manufactured and functionally graded Ti6Al4V porous scaffolds,” *Metals (Basel)*, vol. 8, no. 4, 2018.
- [12] M. Fousová *et al.*, “Promising characteristics of gradient porosity Ti-6Al-4V alloy prepared by SLM process,” *J. Mech. Behav. Biomed. Mater.*, vol. 69, no. October 2016, pp. 368–376, 2017.
- [13] S. Ying, C. Sun, K. Fai, and J. Wei, “Materials & Design Compressive properties of functionally graded lattice structures manufactured by selective laser melting,” *Mater. Des.*, vol. 131, no. March, pp. 112–120, 2017.
- [14] D. S. J. Al-Saedi, S. H. Masood, M. Faizan-Ur-Rab, A. Alomarah, and P. Ponnusamy, “Mechanical properties and energy absorption capability of functionally graded F2BCC lattice fabricated by SLM,” *Mater. Des.*, vol. 144, pp. 32–44, 2018.
- [15] X.-Y. Zhang, G. Fang, L.-L. Xing, W. Liu, and J. Zhou, “Effect of porosity variation strategy on the performance of functionally graded Ti-6Al-4V scaffolds for bone tissue engineering,” *Mater. Des.*, vol. 157, pp. 523–538, Nov. 2018.
- [16] M. A. Surmeneva *et al.*, “Fabrication of multiple-layered gradient cellular metal scaffold via electron beam melting for segmental bone reconstruction,” *Mater. Des.*, vol. 133, pp. 195–204, Nov. 2017.
- [17] F. S. L. Bobbert *et al.*, “Additively manufactured metallic porous biomaterials based on minimal surfaces : A unique combination of topological , mechanical , and mass transport properties,” *Acta Biomater.*, vol. 53, pp. 572–584, 2017.
- [18] C. Han *et al.*, “Continuous functionally graded porous titanium scaffolds manufactured by selective laser melting for bone implants,” *J. Mech. Behav. Biomed. Mater.*, vol. 80, no. March 2017, pp. 119–127, 2018.
- [19] F. Liu, Z. Mao, P. Zhang, D. Z. Zhang, J. Jiang, and Z. Ma, “Functionally graded porous scaffolds in multiple patterns: New design method, physical and mechanical properties,” *Mater. Des.*, vol. 160, pp. 849–860, Dec. 2018.
- [20] S. L. Sing, W. Y. Yeong, F. E. Wiria, and B. Y. Tay, “Characterization of titanium lattice structures fabricated by selective laser melting using an adapted compressive test method,” *Exp. Mech.*, vol. 56, no. 5, pp. 735–748, 2016.
- [21] S. L. Sing, F. E. Wiria, and W. Y. Yeong, “Selective laser melting of lattice structures: A statistical approach to manufacturability and mechanical behavior,” *Robot. Comput. Integr. Manuf.*, vol. 49, no. January 2017, pp. 170–180, 2018.
- [22] S. Ghouse, S. Babu, K. Nai, P. A. Hooper, and J. R. T. Jeffers, “The influence of laser parameters, scanning strategies and material on the fatigue strength of a stochastic porous structure,” *Addit. Manuf.*, vol. 22, pp. 290–301, Aug. 2018.
- [23] Z. A. Ahmadi SM, Hedayati R, Jain RA, Li Y, LeeFlang S, “Effects of laser processing parameters on the mechanical properties, topology, and microstructure of additively manufactured porous metallic biomaterials: A vector-based

- approach,” *Mater. Des.*, vol. 134, pp. 234–243, 2017.
- [24] A. M. Khorasani, M. Goldberg, E. H. Doeven, and G. Littlefair, “Titanium in Biomedical Applications—Properties and Fabrication: A Review,” *J. Biomater. Tissue Eng.*, vol. 5, no. 8, pp. 593–619, Aug. 2015.
- [25] A. Du Plessis, I. Yadroitsava, I. Yadroitsev, S. le Roux, and D. Blaine, “Numerical comparison of lattice unit cell designs for medical implants by additive manufacturing,” *Virtual Phys. Prototyp.*, vol. 13, no. 4, pp. 266–281, Oct. 2018.
- [26] S. N. Khaderi, V. S. Deshpande, and N. A. Fleck, “The stiffness and strength of the gyroid lattice,” *Int. J. Solids Struct.*, vol. 51, no. 23–24, pp. 3866–3877, Nov. 2014.
- [27] N. Muna and A. E. Patterson, “Simple 3-D Visualization of Some Common Mathematical Minimal Surfaces using MATLAB,” Oct. 2018.
- [28] J. G. Torres-Rendon *et al.*, “Bioactive gyroid scaffolds formed by sacrificial templating of nanocellulose and nanochitin hydrogels as instructive platforms for biomimetic tissue engineering,” *Adv. Mater.*, vol. 27, no. 19, pp. 2989–2995, May 2015.
- [29] D. Mahmoud and M. A. Elbestawi, “Selective laser melting of porosity graded lattice structures for bone implants,” *Int. J. Adv. Manuf. Technol.*, pp. 1–13, Oct. 2018.
- [30] T. G. Spears and S. A. Gold, “In-process sensing in selective laser melting (SLM) additive manufacturing,” *Integr. Mater. Manuf. Innov.*, vol. 5, no. 1, p. 2, 2016.
- [31] U. Scipioni Bertoli, A. J. Wolfer, M. J. Matthews, J.-P. R. Delplanque, and J. M. Schoenung, “On the limitations of Volumetric Energy Density as a design parameter for Selective Laser Melting,” *Mater. Des.*, vol. 113, pp. 331–340, Jan. 2017.
- [32] T. D. Shipley H, McDonnell D, Culleton M, Coull R, Lupoi R, O’Donnell G, “Optimisation of process parameters to address fundamental challenges during selective laser melting of Ti-6Al-4V: A review,” *Int. J. Mach. Tools Manuf.*, vol. 128, no. January, pp. 1–20, 2018.
- [33] F. Calignano *et al.*, “Investigation of accuracy and dimensional limits of part produced in aluminum alloy by selective laser melting,” *Int. J. Adv. Manuf. Technol.*, vol. 88, no. 1–4, pp. 451–458, 2017.
- [34] “ISO 13314:2011(en), Mechanical testing of metals — Ductility testing — Compression test for porous and cellular metals.”
- [35] D. Gu *et al.*, “Densification behavior, microstructure evolution, and wear performance of selective laser melting processed commercially pure titanium,” *Acta Mater.*, vol. 60, no. 9, pp. 3849–3860, 2012.
- [36] L. E. Murr *et al.*, “Next-generation biomedical implants using additive manufacturing of complex, cellular and functional mesh arrays,” *Philos. Trans. R. Soc. A Math. Phys. Eng. Sci.*, vol. 368, no. 1917, pp. 1999–2032, 2010.

- [37] ISO 20160, “Implants for surgery — Metallic materials — Classification of microstructures for alpha+beta titanium alloy bars.”
- [38] J. Han *et al.*, “Microstructure and mechanical property of selective laser melted Ti6Al4V dependence on laser energy density,” *Rapid Prototyp. J.*, vol. 23, no. 2, pp. 217–226, 2017.
- [39] V. Gunenthiram *et al.*, “Analysis of laser-melt pool-powder bed interaction during the selective laser melting of a stainless steel,” *J. Laser Appl.*, vol. 29, no. 2, p. 22303, 2017.
- [40] R. A. W. Mines, Y. Shen, W. J. Cantwell, W. Brooks, and C. J. Sutcliffe, “The influence of processing parameters on the mechanical properties of selectively laser melted stainless steel microlattice structures,” *J. Manuf. Sci. Eng. Copyr.*, vol. 132, pp. 1–12, 2010.
- [41] S. . Yakout, M., Elbestawi, M.A., and Veldhuis, “A study of the relationship between thermal expansion and residual stresses in selective laser melting of Ti-6Al-4V.”
- [42] P. J. Tan, J. J. Harrigan, and & S. R. Reid, “Inertia effects in uniaxial dynamic compression of a closed cell aluminium alloy foam,” *Mater. Sci. Technol.*, vol. 18, no. 5, pp. 480–488, 2002.
- [43] B. Yu, K. H. Chien, K. A. Samk, and G. D. Hibbard, “A Mechanism for Energy Absorption: Sequential Micro-kinking in Ceramic Reinforced Aluminum Alloy Lattices during Out-of-plane Compression,” *Mater. Sci. Eng. A*, vol. 716, pp. 11–22, 2018.
- [44] H. M. Frost, “Skeletal structural adaptations to mechanical usage (SATMU): 1. Redefining Wolff’s law: The bone modelling problem,” *Anat. Rec.*, vol. 226, no. 4, pp. 423–432, 1990.
- [45] K. Alvarez and H. Nakajima, “Metallic scaffolds for bone regeneration,” *Materials (Basel)*, vol. 2, no. 3, pp. 790–832, 2009.

Chapter 6

The Influence of Selective Laser Melting Defects on the Fatigue Properties of Ti6Al4V Porosity Graded Gyroids for Bone Implants

Complete Citation:

Mahmoud, Dalia, M. A. Elbestawi, and Kassim S. Al-Rubaie " The Influence of Selective Laser Melting Defects on the Fatigue Properties of Ti6Al4V Porosity Graded Gyroids for Bone Implants." *Submitted to the Additive Manufacturing Journal* March 2020

Copyright:

Relative Contributions:

Dalia Mahmoud: Performed experiments, analysis, and data interpretation. Wrote the first draft of the manuscript.

M. A. Elbestawi: Revised and edited the manuscript.

Kassim S. Al-Rubaie: Revised the microstructural analysis and fatigue interpretation.

Abstract:

Porosity grading of metallic lattice structures is becoming a favorable design for bone implant applications since these structures mimic the bone mechanical and biological properties. Especially when using bio-mimetic unit cell designs created by triply periodic minimal surfaces (TPMS), such as gyroids, making these types of lattice structures dominant over other CAD-based designs. In this study, the manufacturability of gyroids is tested by studying three different designs: uniform porosity with thin struts (G2), thick struts (G4), and graded porosity (G24). The main aim is to understand the influence of selective laser melting (SLM) defects on the static and fatigue properties of uniformly and porosity graded gyroids. Qualitative and quantitative analysis revealed some dimensional deviation between nominal designs and printed parts. An FEA model based on a single unit cell is developed to predict the mechanical properties of uniformly graded porosity parts. The numerical results give insight into how manufacturing irregularities can affect the mechanical properties of lattice structures. Both G24 and G4 designs showed higher apparent modulus of elasticity (E_{app}) and higher compressive strength (σ_p), whereas they both exhibited less fatigue strength than the G2 designs. It was observed that the E_{app} was significantly affected by geometrical errors in strut shape. At the same time, fatigue strength was dependent on the surface quality and the internal defect percentage.

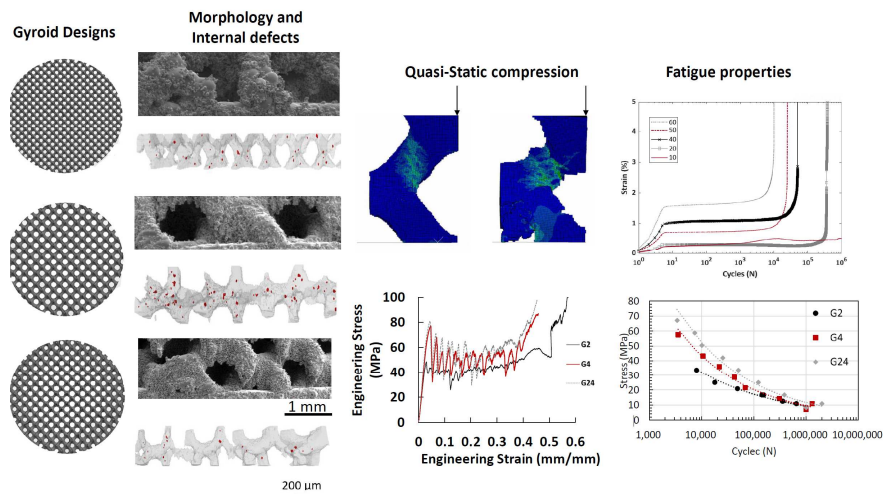
Keywords:

Selective laser melting; Lattice structures; Porosity graded gyroids; Quasi-static compression; Fatigue strength; Ti6Al4V.

Acknowledgment:

The authors would like to acknowledge the support of the Natural Sciences and Engineering Research Council of Canada (NSERC; funding reference number 518494).

Graphical Abstract:



6.1 Introduction

Titanium lattice structures printed by selective laser melting (SLM) are extensively studied for bone implant applications [1,2]. Considering that these porous structures reduce the mismatch between metal and bone stiffness, the stress shielding phenomena can thus be avoided [3]. Moreover, the designed porosities of these structures allow bones to grow within them and help with the fixation of implants [4]. According to the American Society for Testing and Materials (ASTM) definition, SLM is also referred to as laser powder bed fusion (L-PBF) technologies. SLM processes are known for its efficiency in printing complicated structures with fine features. SLM has the capability of manufacturing these porous structures by controlling the shape and size of the unit cells forming those lattice structures [5]. Choosing a lattice structure that mimics bone geometry may help with enhancing cell proliferation, making it more desirable for bone implant applications [6]. Therefore, for the past few years, triply periodic minimal surfaces (TPMS) are preferred to other lattice structures based on traditional CAD designs [7].

The factors affecting the mechanical properties of lattice structures can be categorized into manufacturing and design-related factors. The most concerning SLM parameters are those involved in the volumetric energy density (VED) equation [8], which is the amount of energy delivered to the powder bed to melt the powder. However, the choice of suitable process parameters to print lattice structures depends on the lattice design, material, and the machine used [9]. It was noted that an increase in laser power, would increase the melt pool size, thus increasing the strut size [10]. Statistical analysis has shown that laser power is the most significant factor affecting the dimensional accuracy of lattice structures [11,12]. Most of the studies involved in examining the manufacturability of lattice structures were concerned by CAD-based lattice structures [13-15]. The term

manufacturability here refers to how close the printed parts are from the nominal design, in terms of dimension, geometry, and quality of struts. However, few studies focused on the manufacturability of TPMS lattice structures [16,17].

Some of the design-related factors that affect the mechanical properties of lattice structures are relative density, designed pores morphology, size, and distribution. The relative density can be defined as the ratio of the volume of solid material to the total volume occupied by the lattice [18]. According to Ashby and Gibson's model [18], the relative density is the most significant factor that affects the mechanical properties of lattice structures. Different pore morphology also affects the stiffness of lattice structures, since the failure mode (buckling or bending) changes depending on the unit cell design [19]. Loading direction and strut orientation also contribute to lattice stiffness and mechanical properties [20]. TPMS with gyroid unit cells and relative densities (5-20%) exhibited an elastic modulus of 0.25 to 1,25 GPa [21], which is similar to trabecular bones. TPMS with Schwartz unit cells and relative densities of (35-75%) had a stiffness of 22 GPa, which can be used in hard tissue applications[22].

The fatigue properties of lattice structures depend on the parent material and lattice design (pore morphology and size) as well [23]. Zhao et al. [24] reported that the normalized fatigue strength of Ti6Al4V lattice structures ranges from 0.10-0.25 at 10^6 cycles. This value is lower than 0.4 of its yield strengths, which is the fatigue strength of solid material with the same microstructure. This deterioration in fatigue strength is related to the inherent defects resulting from the SLM process, namely, internal defects and poor surface roughness. Pore design and strut thickness also affect the fatigue strength. Different pore geometries at different relative densities were studied [25,26], fatigue strength increased, and gets closer to that of the solid materials as the relative density increased. It was noted

that the failure mechanism of the lattice shape (buckling or bending) affects the crack propagation rate and, therefore, the fatigue strength.

Permeability of lattice structures is enhanced by using large design but sacrifice the strength and stiffness of the lattice structures since they result in thinner strut sizes [27]. Therefore, a trade-off can be achieved by designing porosity graded lattice structures [28]. Various variations of linear porosity gradation were suggested by Zhang et al. [29], it was observed that the stiffness and failure mechanism would differ according to the rate of porosity change along the length. A mathematical model was developed by Yang et al. [30], to predict and customize the use of porosity graded TPMS lattice structure to fit different applications. In some cases, radially graded TPMS showed higher compressive strength compared to uniformly graded ones [31]. Most of the studies mentioned above focused on the quasi-static compression of the porosity graded TPMS lattice structures; however, the fatigue life of those complicated structures needs further investigation.

From the above literature review, it was noted that more in-depth studies are required to investigate radially graded TPMS lattice structures, especially those made from titanium alloys for bone implants. Therefore, the objective of this study is to investigate 1) the manufacturability of Ti6Al4V TPMS lattice structures with different strut sizes and radially graded porosity, and 2) the influence of SLM process defects on the static and dynamic behavior of uniform and radially graded TPMS lattice structures. Therefore, three different lattice designs for biomedical implants are proposed: two uniform porosity structures (thin and thick struts) and one radially porosity graded structure (struts varying from thick at the border to thin at the center). First, the design and the SLM process conditions are described. Then, the morphologies of the three designs are compared in terms of relative density, errors in strut size, and internal defects. Finally, the results of the quasi-static compression

and fatigue properties are described and co-related to the surface and internal defects resulting from the SLM process.

6.2 Materials and methods

6.2.1 Sample design

The base unit cell of the lattice structures used in this study is gyroids, which is based on TPMS. These designs are known for their adequate mechanical and biological properties for bone implant applications [32]. A code was developed using MATLAB® software to create the uniform and porosity graded gyroid surfaces. The following equation was used to create the gyroid surfaces:

$$\sin\left(\frac{2\pi}{L} \cdot x\right) \cos\left(\frac{2\pi}{L} \cdot y\right) + \sin\left(\frac{2\pi}{L} \cdot y\right) \cos\left(\frac{2\pi}{L} \cdot z\right) + \sin\left(\frac{2\pi}{L} \cdot z\right) \cos\left(\frac{2\pi}{L} \cdot x\right) - t = 0 \quad \text{Equation 6-1}$$

where L is the unit cell size of the gyroid structure, and t is the level constant. Figure 6-1 illustrates the sample design and the unit cell used in this study, the pore size and strut size are defined along the diagonal [1,1,1] as explained in [33]. The values of L and t control the relative density, pore, and strut size of gyroids. A detailed description of the gyroid design and preferred parameter choice for biomedical implants can be found in [34].

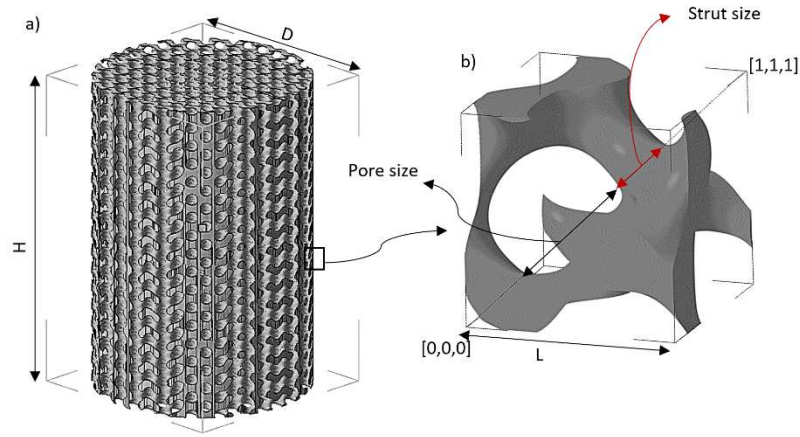


Figure 6-1: a) Gyroid cylindrical sample and b) single unit cell of gyroid showing the unit cell size (L).

In this study, three designs are proposed: G4 designed with a uniform porosity and a strut size of $400\ \mu\text{m}$, G2 designed with uniform porosity and a strut size of $200\ \mu\text{m}$, G24 designed with functionally graded porosity and a strut size of $400\ \mu\text{m}$ at the boundaries reaching $200\ \mu\text{m}$ in the center. The reason for choosing a dense border was to enhance the mechanical strength, which may be beneficial for load-bearing implants. Moreover, gyroids have the capability of continuous functional gradation, which is preferred over other CAD designs [30]. Figure 6-2 represents the top views of the three designs. The printed samples were cylindrical with a diameter of $15\ \text{mm}$ and a height of $22\ \text{mm}$. Twenty replicas were printed and used for morphology characterization, quasi-static, and fatigue testing. The samples were designed to have an equal relative density of 20% , to study the effect of strut thickness on mechanical properties independent of relative density.

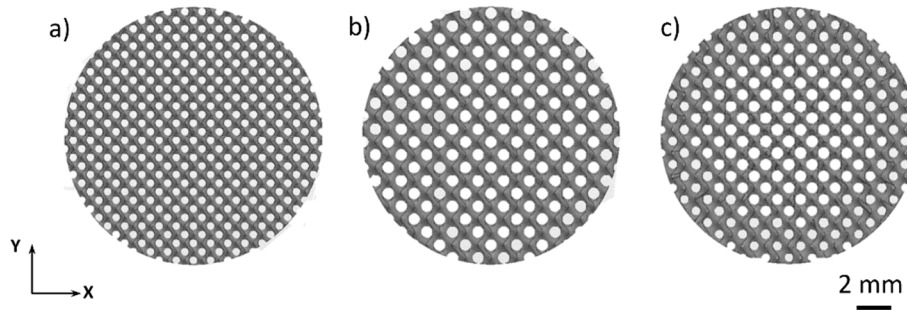


Figure 6-2. Top view of the proposed gyroid designs samples designed at 20% relative density a) G2 having 200 μm struts, b) G4, having 400 μm struts and c) G24 with graded struts in the radial direction (200 μm in the center and 400 μm at the borders).

6.2.2 Powder characterization and SLM process parameters

In this work, gas atomized Ti6Al4V powder was used as a feedstock material. Figure 6-3 depicts the powder characteristics; the powder particles have a spherical form with a diameter ranging from 10 to 45 μm .

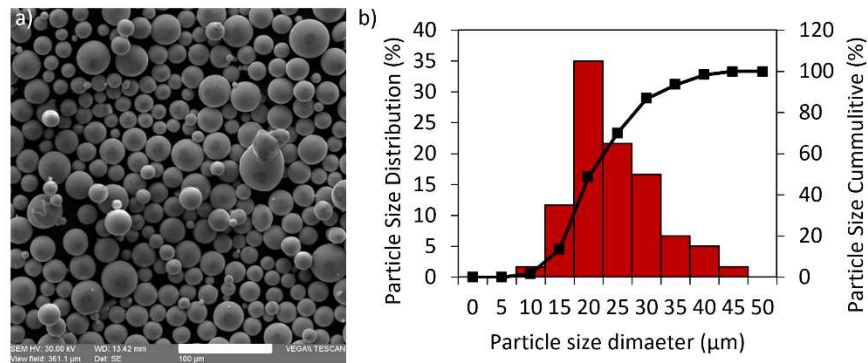


Figure 6-3: Ti6Al4V powder: a) SEM morphology (scale bar=100 μm) and b) size distribution analysis

The gyroid parts were fabricated by a Renishaw machine equipped with a 400 W pulsed fiber laser. The modulated laser works by creating a series of overlapping exposures, having a (10-20 microsecond) pause in between. A pulsed laser is known for less heat

accumulation within the printed parts. Therefore it is more suitable for fine detailed parts as lattice structures [35]. The exposure time, the distance between each exposure point, and the laser power affect the amount of energy delivered to the powder. The higher the amount of energy, the bigger is the melted volume of the metal powder. An attempt to optimize the SLM process parameters have been suggested in a previous study [17]. These parameters resulted in the least error in relative density and strut size. The process parameters used in this study are listed in Table 6-1, and the three proposed designs were printed using the same process parameters.

Table 6-1: The SLM process parameters used for printing the gyroid parts.

Process parameter	Laser power (W)	Exposure time (μ s)	Point distance (μ m)	Layer thickness (μ m)	Hatch distance (μ m)
Value	200	40	60	30	65

It is essential to have a clear understanding of the laser-powder interaction when printing lattice structures. Figure 6-4 presents the scan path in thick struts for G4 and thin struts for G2. The key concept in the SLM process is to direct a laser on a specific path following the part geometry. The laser power, exposure time, as well as the difference between each exposure point and the other (point distance) are all involved in determining the amount of VED fed to the powder. The higher the VED, the bigger the melt pool size created, and vice versa. The melt pool width is estimated to be around 150 μ m, based on the experimental and simulation results in similar settings [36]. In this study, the laser was made to scan a border contour after scanning the strut surface to ensure proper surface quality [34]. The same process parameters were set for the boundary contour, while 75 μ m was left between the contour and the edge of the gyroid parts to compensate for the beam diameter. The melt pool dimension is assumed to be the same in both parts since the same

process parameters were used to print the gyroid parts. The point distance was chosen to give a specific overlapping between the melt pools, thereby ensuring a continuous melting and reducing the internal defects [37]. The volume of the struts was scanned using an alternative 67° scanning strategy that is known to reduce the number of internal defects and enhance the adhesion between successive layers [38].

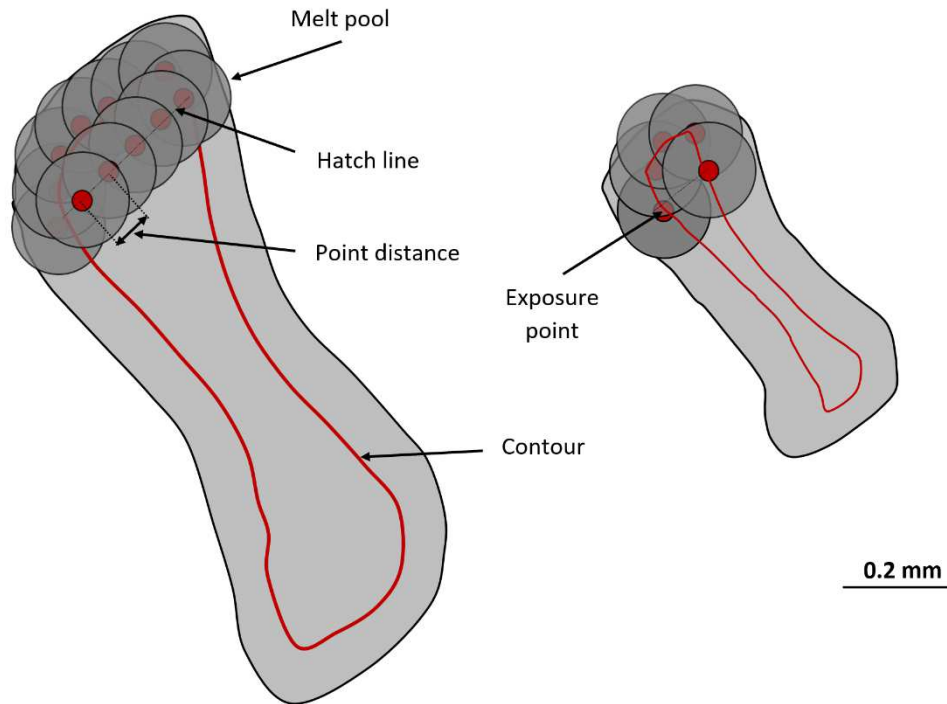


Figure 6-4. The laser scan path in thick struts (G4) versus thin struts (G2), showing the same process parameters used to print the gyroid parts.

6.3 Characterization

6.3.1 Morphology and microstructure

The as-built samples were assessed to understand the effect of the SLM process on the sample density, strut morphology, and microstructure. The samples were ultrasonically cleaned in ethanol for 2 hours, changing the part orientation every 30 minutes. For

metallographic evaluation, samples were sectioned, mounted, mechanically polished, and etched in Kroll's reagent. A scanning electron microscope (SEM) was used to assess the parts morphology, and an optical microscope (OM) was used to evaluate the microstructures of the samples.

The manufacturability of the gyroid lattice can be understood by evaluating the relative density, strut sizes, and internal defects of the printed parts. Archimedes method was used to measure the relative density of the as printed parts; each part was measured in air and acetone. Then the relative density was calculated by dividing the calculated density of the parts by the theoretical density of Ti6Al4V. Micro-computed tomography (microCT) was performed to assess the strut size and internal defects. A Bruker SkyScan 1172 X-ray device was used, applying a 0.5 mm Al and 0.038 mm Cu filter combination. The voltage used was 100 kV, and a pixel size of 8 μm was obtained for this study. The strut sizes were measured from the microCT images using the BoneJ [39], a plugin for image bone analysis that works on ImageJ. For each part, ten different struts were measured from different layers of the reconstructed parts. The internal porosity and defects in each sample were assessed using the 3D analysis tool pack using the CTAn software. Microhardness measurements were carried out on the polished samples under a load of 100 gf for a dwell time of 10 s using a Clemex Microhardness tester. For each gyroid lattice structure, 12 indentations were made, and the average was presented.

6.3.2 Quasi-static compression

Quasi-static compression tests were performed using a 50 KN MTS® machine. The tests were conducted according to the ISO 13314 standard, ensuring a minimum of 10 pores per diameter and height to diameter ratio between 1:1 and 1:2. The samples were compressed at a strain rate of 2 mm/min. Compliance of the machine was measured, and cross-head

displacement measurements were adjusted accordingly. The apparent compressive modulus was calculated from the slope of the elastic part in the stress-strain diagram. The peak strength was considered the highest stress level before the collapse of the part into the plateau region. For each design, three tests were carried out to enhance the accuracy of the results.

6.3.3 Finite element analysis

Finite element analysis (FEA) was used to compare between as designed and as scanned uniform gyroid structures. To help understand the effect of geometric distortion on the gyroid lattice structures mechanical behavior. FEA was performed using ABAQUS/EXPLICIT to simulate the quasi-static compression for as designed and as scanned gyroid unit cells. A single unit cell was used for the model, which is commonly accepted in the literature to reduce the computation time and is in good agreement with experimental analysis [40,41]. MicroCT was used to reconstruct unit cells from G2 and G4 gyroid structures, the reconstructed unit cells were converted into a voxel mesh. The apparent modulus of elasticity (E_{app}) was then numerically evaluates and compare to the analytical solution suggested by Yang et al. [42] and the experimental results from this study.

In this study, linear elastic material properties were assumed. Figure 6-5 illustrates the developed FEA model, two rigid plates simulate the compression platens. The displacement of the upper plate was defined to match that of the experimental test and maintain the same strain rate, whereas the lower plate was fixed. The gyroid

unit cell models were meshed using voxel meshing techniques. The voxel mesh is usually used to model biomedical parts since the complexity, and highly detailed parts are usually hard to model with conventional mesh shapes [43]. Another advantage of the voxel meshing is that it requires less computational time for modeling highly complex structures [44]. Based on a mesh sensitivity analysis, an element size of $7.5\ \mu\text{m}$ was chosen that ensured the convergence of the stiffness for the different unit cells.

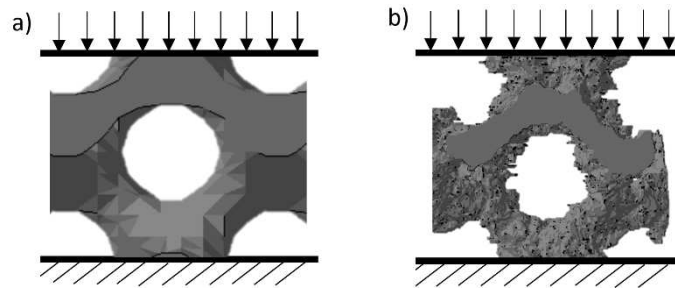


Figure 6-5: FEA model comparing between a) as designed and b) as scanned unit cells

6.3.4 Fatigue testing

The force-controlled fatigue life of the gyroid lattice structures was evaluated via compression-compression fatigue testing at a fixed frequency of 15 Hz and a load ratio of $R = 0.1$. An Instron 8874 servo-hydraulic frame with a load capacity of 50 kN was used. S-N curves were constructed by two phases. In the first phase, four samples were tested at 80, 40, 30, and 20% of the maximum peak strength of the samples. Then, four more samples were tested at 60, 50, 30, 10% of the maximum peak strength of the samples. The test was stopped as the number of cycles reached 10^6 cycles (run-out) or a sudden decrease in the displacement of 2 mm. All the fatigue tests were carried out at room temperature of

about 20 °C. A compliance correction for the machine was applied to account for the deflection of the load frame. The fatigue analysis for lattice structures to be used in bone implants involves studying the strain accumulation, stress-strain cycles, and the S-N curves to understand the crack nucleation, propagation rate, and fatigue ratcheting strain [45].

6.4 Results and discussion

6.4.1 Morphology

6.4.1.1 Qualitative analysis

Figure 6-6 represents the SEM micrographs of the side view of the printed gyroid lattice structures. The presence of satellite powders sintered to the surface of the gyroid parts is related to the nature of the SLM process. The SLM process parameters, heat and powder size affects the quantities of partially sintered powders to the printed parts [46]. They can be easily distinguished from their size that is similar to the starting powder. The excessive energy from the melted parts is conducted to the powder bed, causing the surrounding powder to sinter to the surfaces of the gyroids [47]. The main observation is that G2 struts have discontinuous bulging melt tracks, which can be referred to as balling [48,49]. The balling phenomenon occurs when the molten metal solidifies into spherical beads due to the insufficient wetting of the preceding track and surface tension [9]. Although balling is usually related to using low VED [8], in this work, the reason for balling phenomena is thought to be that short hatch line length does not provide sufficient wetting to successive tracks. As for the thick struts of G4 and G24, heat accumulation is thought to be the main reason for the absence of balling phenomena. Since a greater number of exposures per strut is required to melt G4 thick struts, and more layers are needed, more heat accumulation occurs in thicker struts of G4 than those of G2.

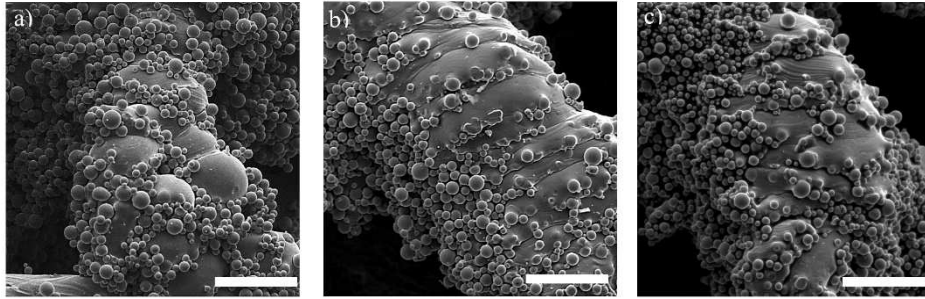


Figure 6-6: SEM side-view images (scale bar =200 μm) of the Ti6Al4V gyroid lattice structures: a) G2, b) G4, and c) G24 (borders).

MicroCT scans were used to reconstruct the gyroid samples, as shown in Figure 6-7; it can be noted that from the top view, the geometrical deviation is minimal. The increase in strut size led to a decrease in the designed pore size, which is usually attributed to the presence of partially melted powder on the melted surfaces. However, in the build direction, relatively larger errors in geometry are noticed. These errors are attributed to unsupported geometry in the gyroids and are referred to as droop effects [50]. These errors increase with the increase in the unsupported material [51], therefore expected to increase with strut size increase, as illustrated in Figure 6-7. Post-processing operations such as sandblasting can be used to remove them and improve the quality of the parts with bigger pore sizes [52]. However, electrochemical polishing might be more suitable for titanium lattice structures with relatively small pore sizes [53].

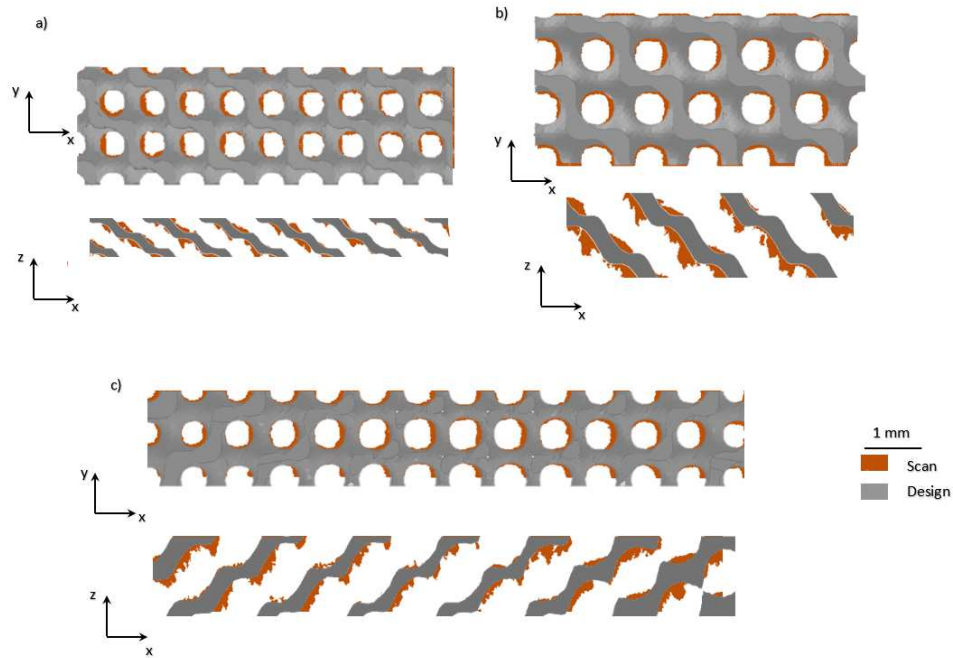


Figure 6-7: Top view (Y-X) and along build direction view (Z-X) of scanned parts vs. designed gyroid lattice structures a) G2 b) G4 and c) G24

6.4.1.2 Quantitative analysis

The measured relative density, strut size, and internal defects results for the three gyroid designs are presented in Table 6-2. The measured relative densities were between 26-29 %, which is higher than the nominal design value (20%). The measured strut sizes indicate an increase in size compared to the design values where an error in the range of 43-47 μm was calculated. The partially sintered powder was considered in the strut size measurements, that is because the powder particles are not loose enough to fall off the gyroid parts while being tested for mechanical properties. Since the pixel size of microCT scanning was limited to 8.4 μm , the smallest internal porosity that was accounted for in this study is two times the pixel size [54]. Although the presence of smaller pores is expected, however, the large size defects are the ones that may deteriorate the mechanical

properties. Internal porosities are between 0.238% and 0.50 %, G2 having the least, and G4 had the highest amounts.

Table 6-2. The quantitative analysis of relative density, strut thickness, and internal defects for the Ti6Al4V gyroid lattice structures

Design	Measured relative density (%) \pm St. dev	Design strut thickness (μm)	Average strut thickness \pm St. dev (μm)	Internal defects \pm St. dev (%)
G2	26.36 \pm 0.11	200	243 \pm 18.734	0.238 \pm 0.101
G4	29.52 \pm 0.18	400	445 \pm 09.74	0.500 \pm 0.140
G24	28.68 \pm 0.17	200 (center) 400 (border)	246 \pm 17.10 (center) 447 \pm 12.84 (border)	0.407 \pm 0.094

6.4.2 Microstructure and microhardness

The microstructure of the Ti6Al4V gyroid designs is shown in Figure 6-8; all the parts show acicular α' martensitic microstructure. Higher magnification images Figure 6-8 (d-f) reveal slight changes in martensite thickness and length appears. However, the cooling rate, which is similar in the three designs, govern those martensitic structures geometry [55]. The microhardness results are shown in Figure 6-9; the means were found to be significantly different with a variation value of 50 HV. The concept of wettability can be used to explain the relatively higher microhardness of thick struts [56]. Thick struts have more exposure points than thin ones, as represented in Figure 6-4. The laser is supposed to melt the struts across hatch lines. Since hatch line length is shorter in thin struts and the modulated laser works by exposure points, only two exposure points are melted compared to four in thick struts. In thin struts, less heat is therefore generated and accumulated; therefore, the melt pool tends to form balls instead. The good metallurgical bonding of adjacent melt pools in thick struts may be thought to increase the microhardness of the gyroid lattice structures.

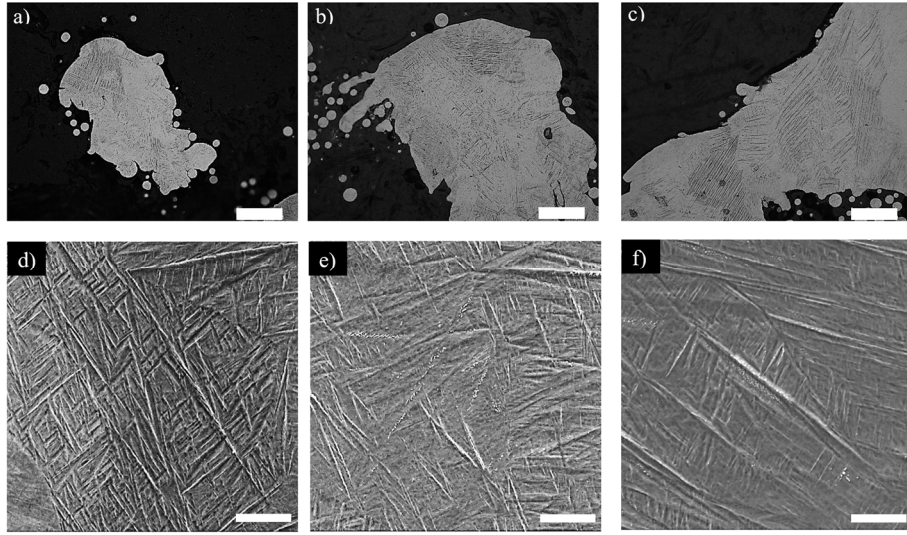


Figure 6-8: Microstructure (scale bar=100 μm) along the build direction of the Ti6Al4V gyroid lattice structures: a) G2, b) G4, and c) G24, and SEM images (scale bar=10 μm, 5000x): e) G2, f) G4 and c) G24.

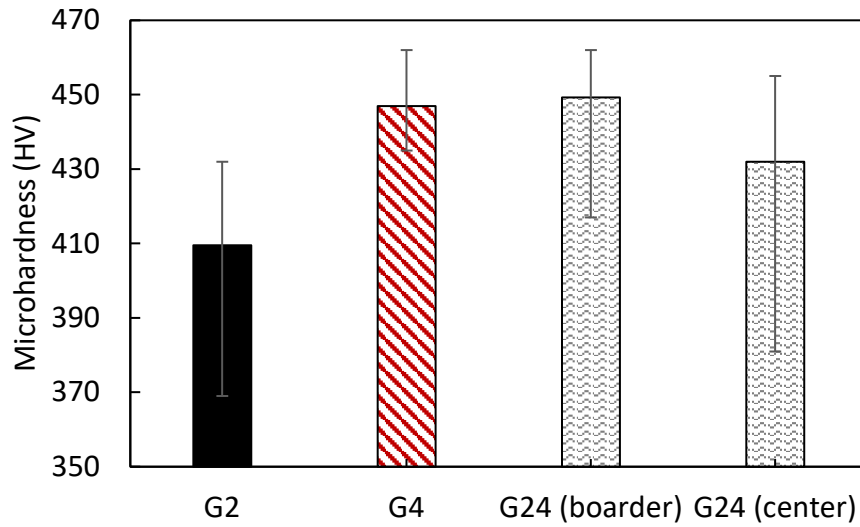


Figure 6-9: Microhardness results for the different designs of Ti6Al4V gyroid lattice structures.

6.4.3 Quasi-static compression

6.4.3.1 Experimental results

Figure 6-10 represents the stress-strain diagram of the three parts. The diagram can be divided into three regions: an elastic, plastic, and densification region. Although the three parts have almost similar relative density, the calculated E_{app} values are different. The relatively low E_{app} values of G2 designs are attributed to the poor melt tracks quality observed in Figure 6-6. Also, the low microhardness of G2 struts indicates that a weaker attachment between melt pools, which might affect the E_{app} and the σ_p . The variation in σ_p is mostly related to strut sizes, and it is expected that thinner struts of G2 would withstand less strength than thicker ones of G4. The relatively higher E_{app} and σ_p values of the G24 design obtained in this work are in line with the results found by Wang et al. [57]. Similar to confined compression, the thicker struts at the borders are restricting the thin inner struts from straining in the radial direction, and this might be the reason for the enhanced mechanical properties. G24 designs may be more suitable for load-bearing implants where high compressive strength and radial graded porosity is required. The improved ductility of G2 designs is related to the fact that these structures had the lowest percentage of internal defects.

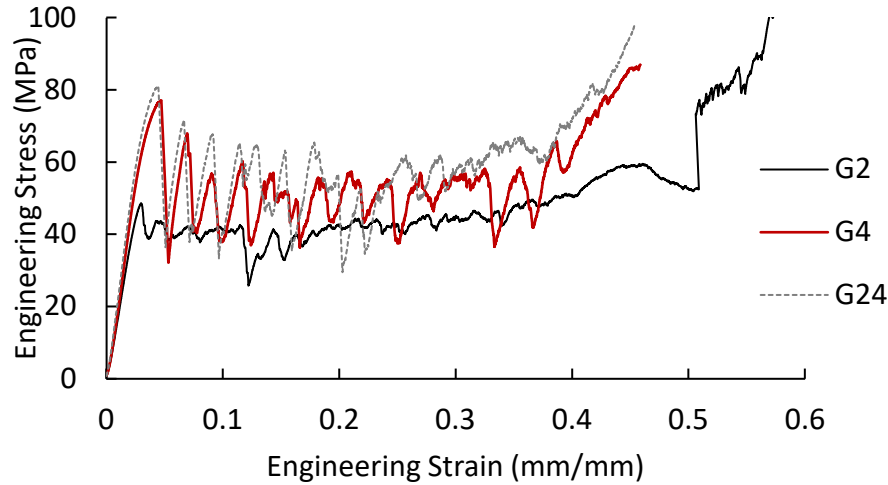


Figure 6-10: Stress-strain diagram for the different Ti6Al4V gyroid lattice structures.

6.4.3.2 Analytical solution

The force per unit cell can be estimated to be equal, assuming an infinite lattice structure formed of multiple gyroid unit cells. Therefore, it is assumed that all the struts will deform in the same way when loaded vertically [58]. In Figure 6-11, an approach to calculate the young's modulus depending on Bernoulli and Timoshenko beam theory was suggested by Yang et al. [42]. The total deflection in the one-fourth of the unit cell was calculated, assuming a simplified beam structure, as illustrated in Figure 6-11 (b). The ratio between the apparent analytical modulus of elasticity of the gyroid lattice structures (E_c) and the parent material modulus of elasticity (E) can be given by the following equation [42]:

$$\frac{E_c}{E} = 0.21 \times \left(\frac{D}{L}\right)^4 \times \frac{1}{1+2.95\left(\frac{D}{L}\right)^2} \quad (6-2)$$

where D is the strut thickness, L is the strut length, and θ is equal to 45° . A detailed description of the analytical model can be found in [42]. The ratio of D/L was kept constant as well. Therefore, the analytical values for both G2 and G4 were calculated based on

equation 2, and both were equal to 2.744 GPa. However, the experimental E_{app} values found for G2 (1.97 GPa), and G4 (2.40 GPa) were lower than the analytical values. Geometrical errors are thought to be the reason for the deterioration in E_{app} .

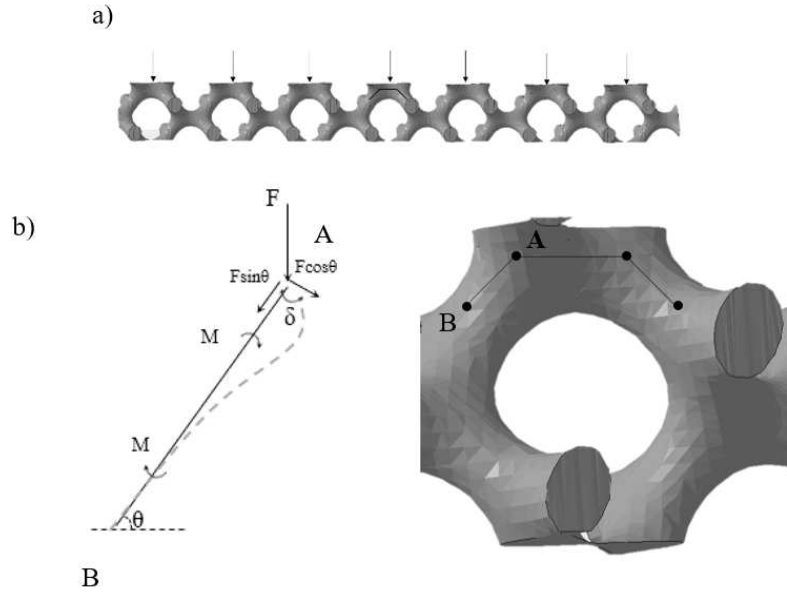


Figure 6-11: Force distribution on a) a single layer, and b) single unit cell of the gyroid lattice structure.

6.4.3.3 Finite Element Analysis

To understand the effect of geometrical deviations in gyroid structures on the modulus of elasticity, an FEA model was developed to compare the designed gyroid lattice structures with scanned ones. Since scanned unit cells are expected to have variations between one and the other, three scanned unit cells from G2 and G4 were tested in the model, and the average values of E_{app} were calculated. The results of the analytical and numerical models are compared with the experimental and shown in Figure 6-12. Comparing the analytical and FEA design results, it was noted that the higher estimated values for E_{app} are related to

the geometrical simplification assumptions in the analytical model. The variation between the FEA design and FEA scan can be attributed to the geometrical variations and errors in strut size. The stair step effect on the surface act as stress concentration points, which are expected to facilitate the crack propagation resulting from the bending stresses on the struts. Finally, the difference between the FEA scan and experimental results is attributed to the fact that satellite powders are modeled as fully melted material. However, these powders are assumed to have a weak attachment to the gyroid structures. Overall, the developed FEA model gives good agreement to experimental results, when scanned unit cells are used. Thus, can be used to predict the E_{app} of printed gyroids and reduce the need for experimental procedures.

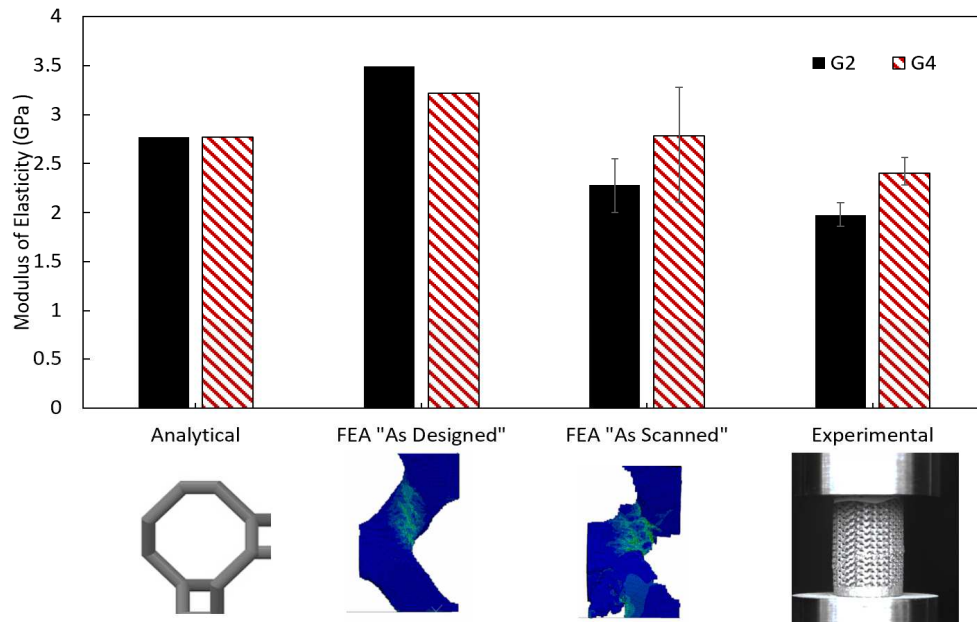


Figure 6-12: Analytical, FEA, and experimental results for E_{app} .

6.4.4 Fatigue testing

6.4.4.1 Strain accumulation

The strain measurement in the cellular structure is often studied to understand crack initiation and crack propagation rate [45]. A typical stain versus cycle for a lattice specimen subjected to compression-compression fatigue loading can be divided into three stages. In stage I, the crack initiates with a relatively small value of plastic strain. As the crack starts to propagate across the struts, stage II appears and is usually defined by the combination of plastic strain accumulation and fatigue crack propagation. Finally, as the crack propagation rate increases significantly, stage III occurs in which the part fails.

The strain accumulation curves for the three designs are presented in Figure 6-13. It can be noted that the three stages are present for the three designs. As expected, the number of cycles to failure (N) increases as the loading stress decreases for the three designs. The crack propagates at $N < 10$ for G4 and G24, and after $N > 10$ for G2. Thus, the crack initiation is faster in G4 and G24 designs, which may be attributed to the fact that surface area per strut is larger in G4 and G24. These results go in line with the findings by Pegues et al. [59]; larger surface areas increase the likelihood of multiple cracks initiation in the same strut.

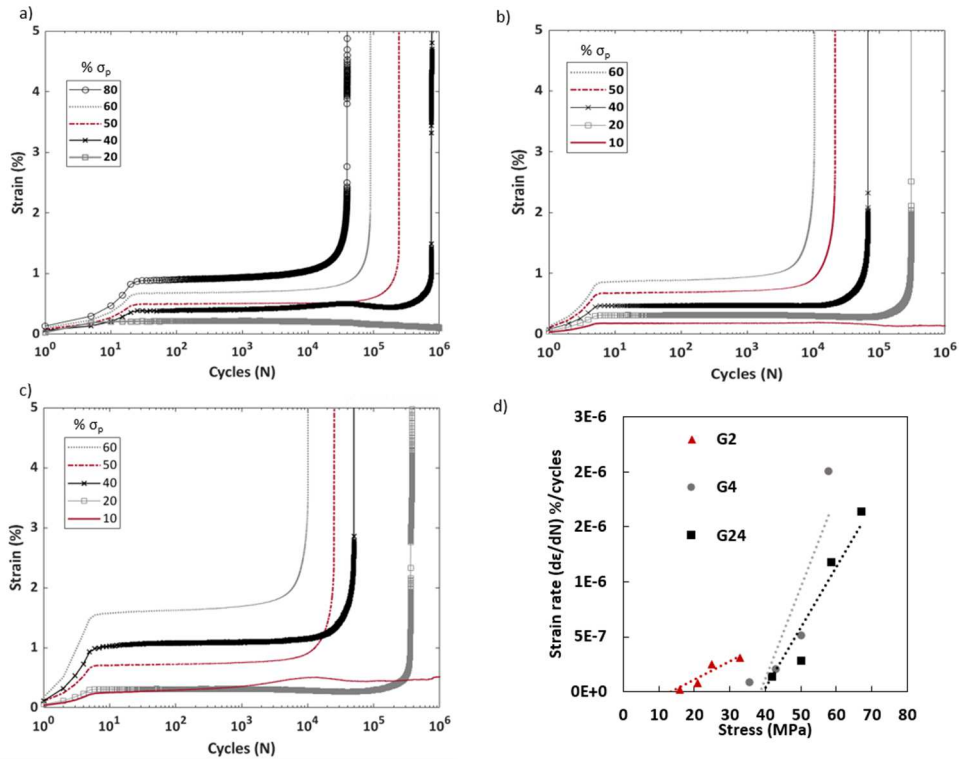


Figure 6-13. Strain accumulation curves: a) G2, b) G4, and c) G24. d) Crack propagation rate for the three designs.

Figure 6-13d compares crack propagation rates by plotting the strain rate versus stress for the three designs. It can be clearly distinguished that the crack propagation rate and plastic strain accumulation are dependent on the value of stress. The G2 structure shows a lower strain rate than G4 and G24, which means that the crack propagation rate in these struts was slower than in G4 and G24. In this case, analyzing the internal porosity within the struts had to be revisited.

Figure 6-14a represents the pore size distribution of the internal defects in the reconstructed parts. The results were obtained from the average of three layers in each design group. It can be noted that G4 and G24 have a higher frequency of internal defects. Also, by analyzing the internal defect distribution along the X-axis, G2 and G4 have a somewhat

random distribution, as shown in Figure 6-14b and Figure 6-14c. Figure 6-14d shows that the thin struts in G24 (center) had fewer internal defects than the thicker ones (border). The reason that thin struts have fewer internal defects than thicker ones may be related to the fact that they need fewer exposure points and fewer overlapping melt pools. Therefore, the slower crack propagation rate in G2 might be related to the relatively low internal defect percentage.

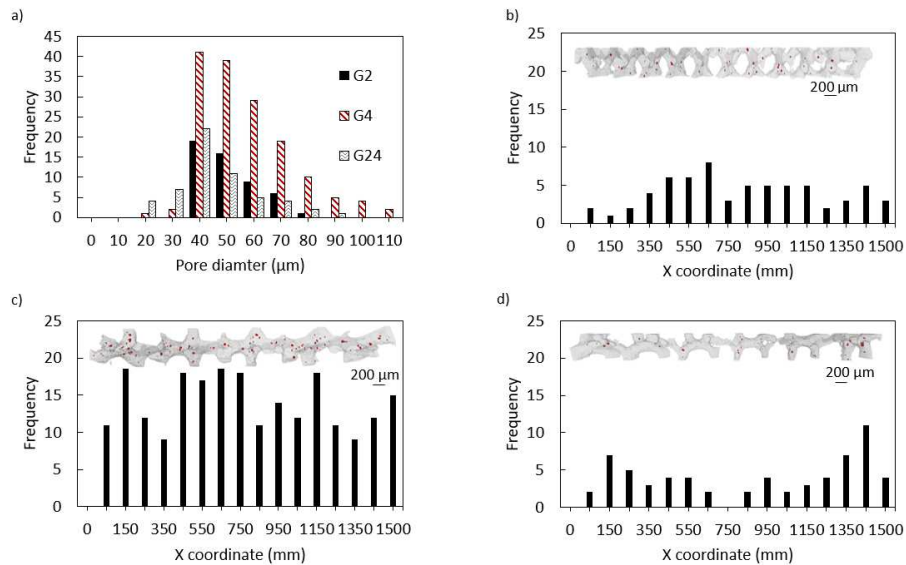


Figure 6-14: a) Internal porosity distribution in three gyroid lattice structures. Frequency of internal porosity along the x-direction in b) G2, c) G4, and d) G24.

6.4.4.2 Cyclic stress-strain

The effect of fatigue cycles on the stress-strain loops of the lattice structures can be used to understand the cyclic ratcheting mechanism for fatigue failure [60,61]. Two main characteristics are defined from this relationship, the creep-fatigue strain (ϵ_c), which is the component of strain related to time, and recently referred to as cyclic ratcheting [45]. The ϵ_c can be calculated from the translation of the K^{th} hysteresis loop. The second important

feature is the fatigue strain (ϵ_f), which can be defined as the difference in the strain value between the k^{th} hysteresis loop and the first hysteresis loop. The slope of each hysteresis loop represents the change in the modulus of elasticity in each cycle. The fatigue strain is the component of the total strain directly related to fatigue failure. Figure 6-15a illustrates the relationship between ϵ_c and ϵ_f . Figure 6-15 b, c, and d illustrate the difference between the stress-strain hysteresis cycles for the three gyroid designs. G2 designs do not show much translation in between one loop and the other, while the slope of the hysteresis changes gradually. Whereas a gradual translation is evident in both G4 and G24, accompanied by a slight change in the slope of the hysteresis loops.

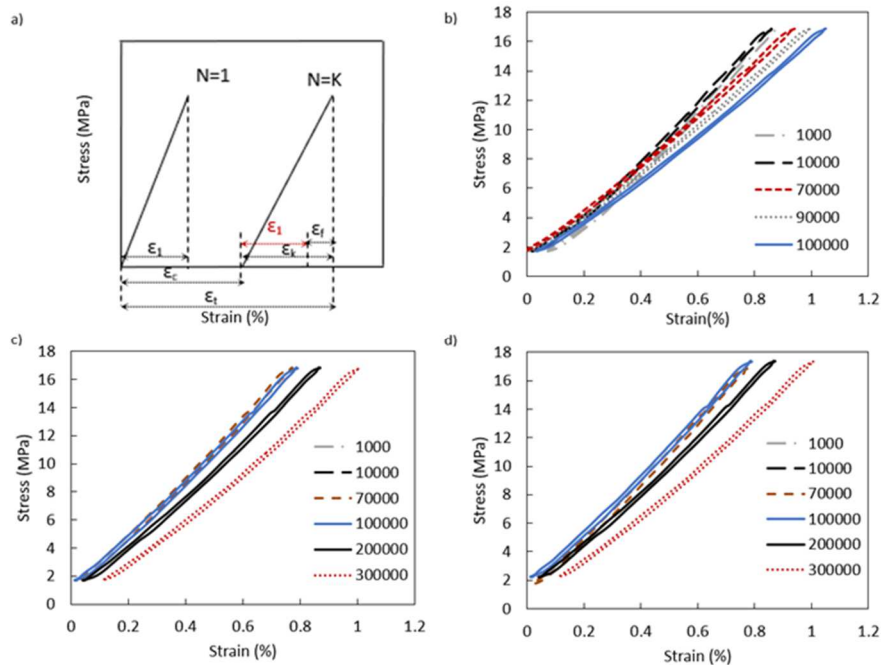


Figure 6-15: a) Calculation of ϵ_c and ϵ_f . Cyclic stress-strain for b) G2, c) G4, and d) G24.

The ϵ_c and ϵ_f values were plotted against the number of cycles and presented in Figure 6-16. For the G2 designs, the observed fatigue strain is much higher than the ratcheting strain

from almost the beginning of the loading. As for G4 and G24 designs, the ratcheting strain becomes responsible for failure up to a certain level. For G4 designs, this level is around 100000 cycles, as for the G24 designs, the level is higher (200000 cycles). According to Zhao [24], bending deformation is thought to contribute more to the fatigue crack growth.

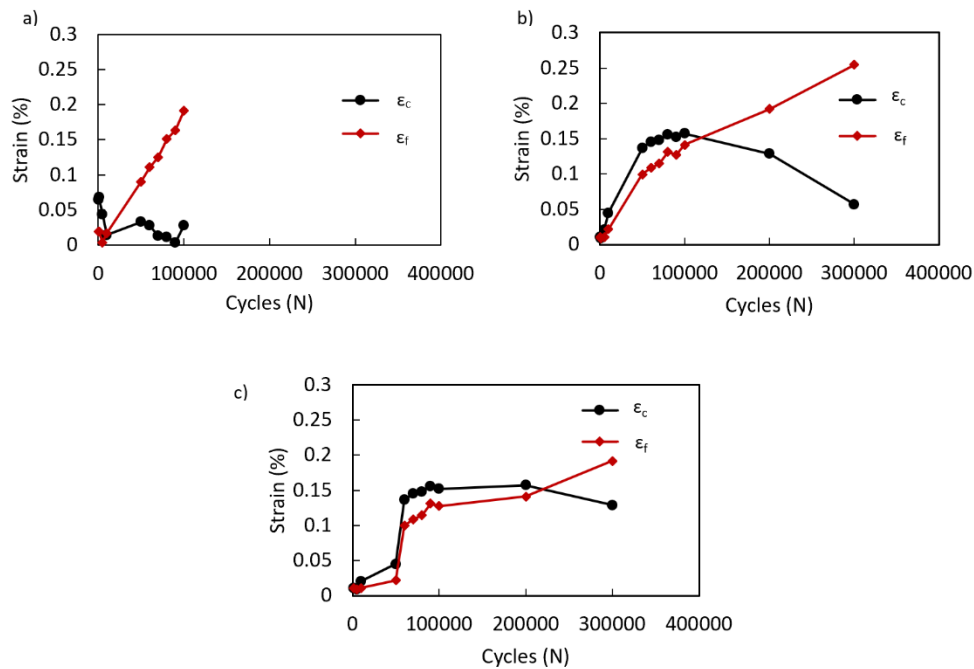


Figure 6-16: Creep strain and fatigue damage strain for the three different designs: a) G2, b) G4, and c) G24.

6.4.4.3 *S-N curves*

The fatigue life of the sample was determined at the onset of the sudden change in strain. In this study, a displacement of 2 mm was set to be the failure point. Any sample that survived 10^6 cycles was considered as run-out. The S-N curves of the G2, G4, and G24 lattice structures are presented in Figure 6-17a, in which the maximum applied stress is plotted as a function of the number of cycles to failure (N). Normalized stress concept (maximum applied stress/yield strength) was used to isolate the variation in yield strength

of the structures, and the results are shown in Figure 6-17b. In Figure 6-17, fatigue life increased gradually by decreasing the maximum applied stress or normalized stress, as expected. For 10^6 cycles, the normalized fatigue strength of the studied lattice structures ranged from 0.1-0.2. These findings are in line with those cited in the literature [62,63].

Three reasons are attributed to the higher fatigue performance of the G2 design compared to G4 or G24 designs. The first reason is related to the higher ductility of G2 designs observed in Figure 6-10. The stress-strain curve of the G2 structure is much more damped than those of the other structures, indicating that the G2 design features more plastic deformation as compared to G4 or G24. More plastic deformation (high ductility) can reflect in better fatigue performance, as seen in Figure 6-17. The second reason could be the lower percentage of internal defects recorded in Table 6-2, thus slowing the crack propagation rate in G2 designs compared to G4 and G24 designs. Finally, features like partially melted powder, rough surface, internal, and staircase effect generated during the layers building give rise to stress concentrations, thus facilitating the crack initiation in the three designs. However, these features might facilitate faster crack initiation in thicker struts, since they have a larger surface area per strut compared to thinner ones.

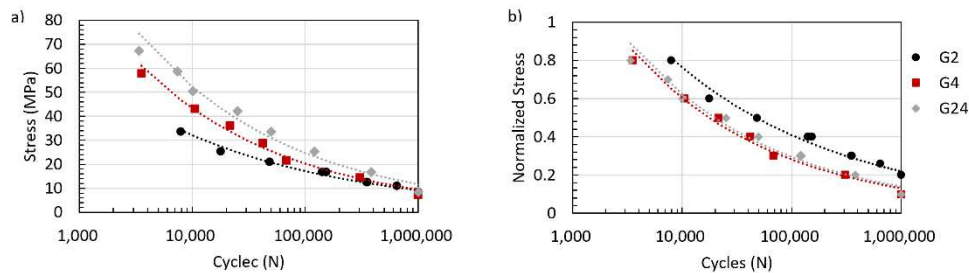


Figure 6-17: S-N curves of the G2, G4, and G24 gyroid lattice structures: a) global stress method and b) normalized global stresses method.

6.4.4.4 *Fracture surface*

Fatigue cracks can mostly be initiated by bending tensile stresses during compression-compression testing, as illustrated in Figure 6-18 (a, b). The crack locations are in the middle of the struts, which was expected from the numerical results. The crack may start due to stress concentrators and then propagates until a brittle fracture occurred by the collapse of unit cell layers of the structure [64]. A typical fracture mode of the gyroid designs was studied by SEM and is presented in Figure 6-18c. Fatigue striations were evident in the rough fracture surface; a possible crack initiation site is shown in figure 18d. The presence of internal pores on the fracture surface is expected to reduce the fatigue strength. However, no signs of crack initiation at pores were found in the studied designs. Similar fatigue fracture mechanisms were identified in [65].

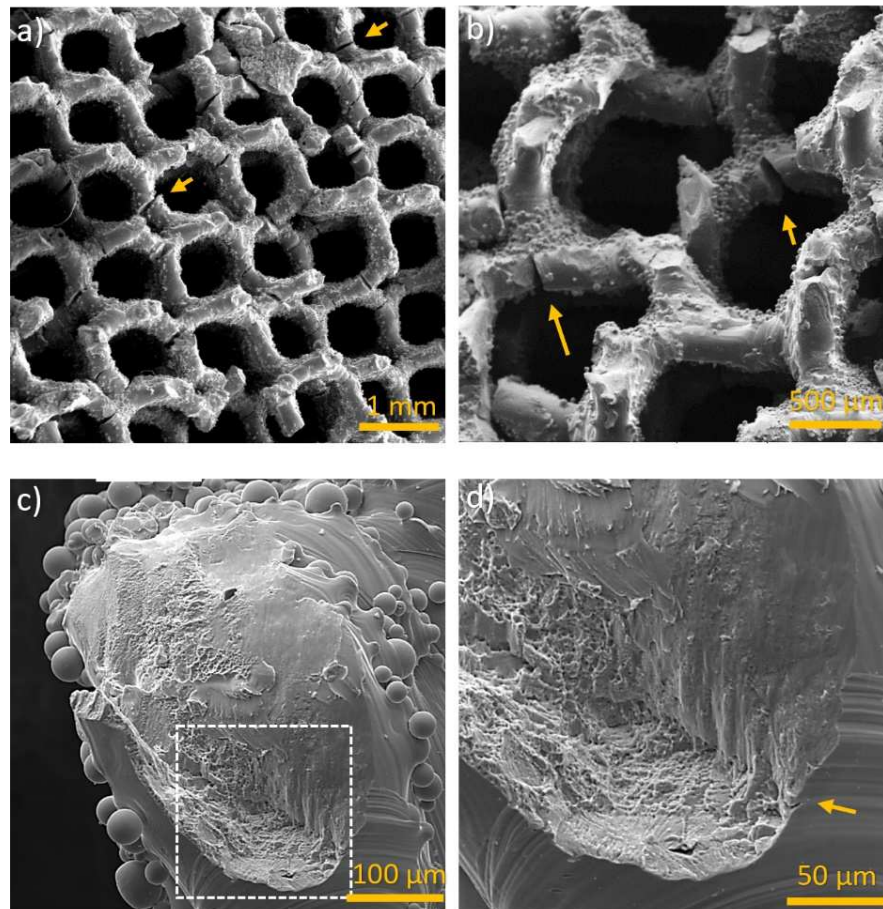


Figure 6-18: SEM micrographs of the fatigue fracture surfaces of the gyroid lattice structures, (a, b) multiple strut fracture surfaces, (c) possible initiation sites at the strut surface, d) higher magnification of striations.

6.5 Conclusions

Three gyroid designs were proposed in this work, thin struts (G2), thick struts (G4), and porosity graded struts (G24). The morphology, microstructure, quasi-static, and fatigue properties of the three designs were assessed. The requirement for bone implants changes according to the place of the implant within the human body. Therefore, it is hard to choose an optimum design among the proposed lattice structures in this study. The need

to understand the effect of the SLM process defects on the static and dynamic strength of the lattice structures is crucial. The outcome of this study may help designers understanding which design to choose for different bone implant applications. The main conclusions are as follows:

- 1- Different gyroid strut sizes were printed using optimized SLM process parameters. There is no significant difference between the measured relative density and error in strut sizes among the three gyroid lattice structures.
- 2- Thicker struts require more laser exposure in general; this leads to more heat accumulation per surface area of the gyroid struts. On the one hand, it ensures good bonding between successive layers, but on the other hand, it may lead to higher internal porosities and defects.
- 3- The compressive strength σ_p of radially graded gyroids (G24) was higher than uniformly graded gyroids (G4 and G2). Therefore, they can be more beneficial for load-bearing implants.
- 4- The results from the numerical model suggest that the manufacturing irregularities affect the mechanical properties of the gyroid structures. Stair case effect errors resulting in irregular geometry facilitates crack propagation during quasistatic compression.
- 5- The G2 designs had the highest fatigue properties compared to G4 and G24 gyroid parts. High fatigue strength can be related to G2 designs higher ductility, lower internal defects, and small surface area per strut. All this contributes to later crack initiation and slower crack propagation compared to the other designs.

Future work to improve fatigue life by post-processes such as chemical etching, HIP, and stress relief will be studied. Moreover, different functionally graded designs (i.e.,

large pores on the surface and smaller pores in the core) will be compared to the current design. Finally, the numerical simulation will be developed to predict the fatigue life of the gyroid lattice structures and reduce the need for experimental work.

6.6 References

- [1] L.E. Murr, S.M. Gaytan, F. Medina, H. Lopez, E. Martinez, B.I. Machado, D.H. Hernandez, L. Martinez, M.I. Lopez, R.B. Wicker, J. Bracke, Next-generation biomedical implants using additive manufacturing of complex, cellular and functional mesh arrays, *Philos. Trans. R. Soc. A Math. Phys. Eng. Sci.* 368 (2010) 1999–2032. <https://doi.org/368/1917/1999> [pii]r10.1098/rsta.2010.0010 [doi].
- [2] M. Dallago, F. Zanini, S. Carmignato, D. Pasini, M. Benedetti, Effect of the geometrical defectiveness on the mechanical properties of SLM biomedical Ti6Al4V lattices, in: *Procedia Struct. Integr.*, Elsevier B.V., 2018: pp. 161–167. <https://doi.org/10.1016/j.prostr.2018.12.027>.
- [3] H.M. Frost, Skeletal structural adaptations to mechanical usage (SATMU): 1. Redefining Wolff's law: The bone modelling problem, *Anat. Rec.* 226 (1990) 423–432. <https://doi.org/10.1002/ar.1092260404>.
- [4] J. Van Der Stok, M.K.E. Koolen, M.P.M. De Maat, S. Amin Yavari, J. Alblas, P. Patka, J.A.N. Verhaar, E.M.M. Van Lieshout, A.A. Zadpoor, H. Weinans, H. Jahr, Full regeneration of segmental bone defects using porous titanium implants loaded with BMP-2 containing fibrin gels, *Eur. Cells Mater.* 29 (2015) 141–154. <https://doi.org/10.22203/eCM.v029a11>.
- [5] X.P. Tan, Y.J. Tan, C.S.L. Chow, S.B. Tor, W.Y. Yeong, Metallic powder-bed based 3D printing of cellular scaffolds for orthopaedic implants : A state-of-the-art review on manufacturing , topological design , mechanical properties and biocompatibility, *Mater. Sci. Eng. C.* 76 (2017) 1328–1343. <https://doi.org/10.1016/j.msec.2017.02.094>.
- [6] Z. Wang, C. Huang, J. Wang, P. Wang, S. Bi, C.A. Abbas, Design and Simulation of Flow Field for Bone Tissue Engineering Scaffold Based on Triply Periodic Minimal Surface, *Chinese J. Mech. Eng. (English Ed.)* 32 (2019) 19. <https://doi.org/10.1186/s10033-019-0329-7>.
- [7] L.-Y. Zhu, L. Li, J.-P. Shi, Z.-A. Li, J.-Q. Yang, Mechanical characterization of 3D printed multi-morphology porous Ti6Al4V scaffolds based on triply periodic minimal surface architectures., *Am. J. Transl. Res.* 10 (2018) 3443–3454. <http://www.ncbi.nlm.nih.gov/pubmed/30662598> (accessed March 16, 2020).
- [8] J. Ciurana, L. Hernandez, J. Delgado, Energy density analysis on single tracks formed by selective laser melting with CoCrMo powder material, (n.d.). <https://doi.org/10.1007/s00170-013-4902-4>.

- [9] T. Maconachie, M. Leary, B. Lozanovski, X. Zhang, M. Qian, O. Faruque, M. Brandt, SLM lattice structures: Properties, performance, applications and challenges, *Mater. Des.* 183 (2019) 108137. <https://doi.org/10.1016/j.matdes.2019.108137>.
- [10] C. Qiu, S. Yue, N.J.E. Adkins, M. Ward, H. Hassanin, P.D. Lee, P.J. Withers, M.M. Attallah, Influence of processing conditions on strut structure and compressive properties of cellular lattice structures fabricated by selective laser melting, *Mater. Sci. Eng. A.* 628 (2015) 188–197. <https://doi.org/10.1016/j.msea.2015.01.031>.
- [11] S.L. Sing, W.Y. Yeong, F.E. Wiria, B.Y. Tay, Characterization of titanium lattice structures fabricated by selective laser melting using an adapted compressive test method, *Exp. Mech.* 56 (2016) 735–748. <https://doi.org/10.1007/s11340-015-0117-y>.
- [12] S.L. Sing, F.E. Wiria, W.Y. Yeong, Selective laser melting of lattice structures: A statistical approach to manufacturability and mechanical behavior, *Robot. Comput. Integr. Manuf.* 49 (2018) 170–180. <https://doi.org/10.1016/j.rcim.2017.06.006>.
- [13] H. Salem, L.N. Carter, M.M. Attallah, H.G. Salem, Influence of processing parameters on internal porosity and types of defects formed in Ti6Al4V lattice structure fabricated by selective laser melting, *Mater. Sci. Eng. A.* 767 (2019) 138387. <https://doi.org/10.1016/j.msea.2019.138387>.
- [14] K. Kadirgama, W.S.W. Harun, F. Tarlochan, M. Samykano, D. Ramasamy, M.Z. Azir, H. Mehboob, Statistical and optimize of lattice structures with selective laser melting (SLM) of Ti6Al4V material, *Int. J. Adv. Manuf. Technol.* (2018) 1–16. <https://doi.org/10.1007/s00170-018-1913-1>.
- [15] R.A.W. Mines, Y. Shen, W.J. Cantwell, W. Brooks, C.J. Sutcliffe, S. Tsopanos, R.A.W. Mines, S. McKown, Y. Shen, W.J. Cantwell, W. Brooks, C.J. Sutcliffe, The Influence of Processing Parameters on the Mechanical Properties of Selectively Laser Melted Stainless Steel Microlattice Structures, *J. Manuf. Sci. Eng.* 132 (2010) 041011. <https://doi.org/10.1115/1.4001743>.
- [16] J. Maszybrocka, B. Gapiński, M. Dworak, G. Skrabalak, A. Stwora, The manufacturability and compression properties of the Schwarz Diamond type Ti6Al4V cellular lattice fabricated by selective laser melting, (n.d.). <https://doi.org/10.1007/s00170-019-04422-6>.
- [17] D. Mahmoud, M.A. Elbestawi, B. Yu, Process–Structure–Property Relationships in Selective Laser Melting of Porosity Graded Gyroids, *J. Med. Device.* 13 (2019) 031005. <https://doi.org/10.1115/1.4043736>.
- [18] L.J. Gibson, *Cellular Solids: Structure, Properties and Applications*, 1999.
- [19] A. Du Plessis, I. Yadroitsava, I. Yadroitsev, S. le Roux, D. Blaine, Numerical comparison of lattice unit cell designs for medical implants by additive manufacturing, *Virtual Phys. Prototyp.* 13 (2018) 266–281. <https://doi.org/10.1080/17452759.2018.1491713>.
- [20] M. Mazur, M. Leary, S. Sun, M. Vcelka, D. Shidid, M. Brandt, Deformation and failure behaviour of Ti-6Al-4V lattice structures manufactured by selective laser melting

(SLM), *Int J Adv Manuf Technol.* 84 (2016) 1391–1411. <https://doi.org/10.1007/s00170-015-7655-4>.

[21] C. Yan, L. Hao, A. Hussein, P. Young, Ti – 6Al – 4V triply periodic minimal surface structures for bone implants fabricated via selective laser melting, *J. Mech. Behav. Biomed. Mater.* 51 (2015) 61–73. <https://doi.org/10.1016/j.jmbbm.2015.06.024>.

[22] N. Soro, H. Attar, X. Wu, M.S. Dargusch, Investigation of the structure and mechanical properties of additively manufactured Ti-6Al-4V biomedical scaffolds designed with a Schwartz primitive unit-cell, *Mater. Sci. Eng. A.* 745 (2019) 195–202. <https://doi.org/10.1016/j.msea.2018.12.104>.

[23] S. Ghouse, S. Babu, K. Nai, P.A. Hooper, J.R.T. Jeffers, The influence of laser parameters, scanning strategies and material on the fatigue strength of a stochastic porous structure, *Addit. Manuf.* 22 (2018) 290–301. <https://doi.org/10.1016/J.ADDMA.2018.05.024>.

[24] S. Zhao, S.J. Li, W.T. Hou, Y.L. Hao, R. Yang, R.D.K.K. Misra, The influence of cell morphology on the compressive fatigue behavior of Ti-6Al-4V meshes fabricated by electron beam melting, *J. Mech. Behav. Biomed. Mater.* 59 (2016) 251–264. <https://doi.org/10.1016/j.jmbbm.2016.01.034>.

[25] Y. Wu, L. Yang, An Investigation of The Fatigue Strength of Multiple Cellular Structures Fabricated by Electron Beam Powder Bed Fusion Additive Manufacturing Process, in: *Proc. 29th Annu. Int. Solid Free. Fabr. Symp.*, 2018: pp. 726–737. <https://www.researchgate.net/publication/329000766> (accessed November 29, 2019).

[26] S.M. Ahmadi, R. Hedayati, Y. Li, K. Lietaert, N. Tümer, A. Fatemi, C.D. Rans, B. Pouran, H. Weinans, A.A. Zadpoor, Fatigue performance of additively manufactured meta-biomaterials: The effects of topology and material type, *Acta Biomater.* 65 (2018) 292–304. <https://doi.org/10.1016/j.actbio.2017.11.014>.

[27] H. Montazerian, E. Davoodi, M. Asadi-Eydivand, J. Kadkhodapour, M. Solati-Hashjin, Porous scaffold internal architecture design based on minimal surfaces: A compromise between permeability and elastic properties, *Mater. Des.* 126 (2017) 98–114. <https://doi.org/10.1016/j.matdes.2017.04.009>.

[28] X. Miao, D. Sun, X. Miao, D. Sun, Graded/Gradient Porous Biomaterials, *Materials (Basel)*. 3 (2009) 26–47. <https://doi.org/10.3390/ma3010026>.

[29] X.-Y. Zhang, G. Fang, L.-L. Xing, W. Liu, J. Zhou, Effect of porosity variation strategy on the performance of functionally graded Ti-6Al-4V scaffolds for bone tissue engineering, *Mater. Des.* 157 (2018) 523–538. <https://doi.org/10.1016/J.MATDES.2018.07.064>.

[30] L. Yang, R. Mertens, M. Ferrucci, C. Yan, Y. Shi, S. Yang, Continuous graded Gyroid cellular structures fabricated by selective laser melting: Design, manufacturing and mechanical properties, *Mater. Des.* 162 (2019) 394–404. <https://doi.org/10.1016/j.matdes.2018.12.007>.

[31] J. Maszybrocka, B. Gapiński, M. Dworak, G. Skrabalak, A. Stwora, Modelling, manufacturability and compression properties of the CpTi grade 2 cellular lattice with

radial gradient TPMS architecture, *Bull. POLISH Acad. Sci. Tech. Sci.* 67 (2019). <https://doi.org/10.24425/bpasts.2019.130181>.

[32] S.C. Kapfer, S.T. Hyde, K. Mecke, C.H. Arns, G.E. Schröder-Turk, Minimal surface scaffold designs for tissue engineering, *Biomaterials.* 32 (2011) 6875–6882. <https://doi.org/10.1016/j.biomaterials.2011.06.012>.

[33] J.M. Walker, Additive Manufacturing towards the Realization of Porous and Stiffness-tailored NiTi Implants, (2014). <https://doi.org/10.1017/CBO9781107415324.004>.

[34] D. Mahmoud, M.A. Elbestawi, Selective laser melting of porosity graded lattice structures for bone implants, *Int. J. Adv. Manuf. Technol.* (2018) 1–13. <https://doi.org/10.1007/s00170-018-2886-9>.

[35] A.G. Demir, P. Colombo, B. Previtali, From pulsed to continuous wave emission in SLM with contemporary fiber laser sources: effect of temporal and spatial pulse overlap in part quality, *Int. J. Adv. Manuf. Technol.* 91 (2017) 2701–2714. <https://doi.org/10.1007/s00170-016-9948-7>.

[36] P. Tang, S. Wang, M. Long, H. Duan, S. Yu, D. Chen, S. Fan, Thermal Behavior During the Selective Laser Melting Process of Ti-6Al-4V Powder in the Point Exposure Scan Pattern, *Metall. Mater. Trans. B Process Metall. Mater. Process. Sci.* 50 (2019) 2804–2814. <https://doi.org/10.1007/s11663-019-01670-5>.

[37] P. Bajaj, J. Wright, I. Todd, E.A. Jägle, Predictive process parameter selection for Selective Laser Melting Manufacturing: Applications to high thermal conductivity alloys, *Addit. Manuf.* 27 (2019) 246–258. <https://doi.org/10.1016/j.addma.2018.12.003>.

[38] H. Meier, C. Haberland, Experimental studies on selective laser melting of metallic parts, *Materwiss. Werksttech.* 39 (2008) 665–670. <https://doi.org/10.1002/mawe.200800327>.

[39] M. Doube, M.M. Klosowski, I. Arganda-Carreras, F.P. Cordelières, R.P. Dougherty, J.S. Jackson, B. Schmid, J.R. Hutchinson, S.J. Shefelbine, BoneJ: Free and extensible bone image analysis in ImageJ, *Bone.* 47 (2010) 1076–1079. <https://doi.org/10.1016/j.bone.2010.08.023>.

[40] H.-H. Cho, Y. Cho, N. Han, Finite element analysis for mechanical response of Ti foams with regular structure obtained by selective laser melting, (2015). <https://doi.org/10.1016/j.actamat.2015.07.003>.

[41] T.B. Sercombe, X. Xu, V.J. Challis, R. Green, S. Yue, Z. Zhang, P.D. Lee, Failure modes in high strength and stiffness to weight scaffolds produced by Selective Laser Melting, *Mater. Des.* 67 (2015) 501–508. <https://doi.org/10.1016/j.matdes.2014.10.063>.

[42] L. Yang, C. Yan, H. Fan, Z. Li, C. Cai, P. Chen, Y. Shi, S. Yang, Investigation on the orientation dependence of elastic response in Gyroid cellular structures, *J. Mech. Behav. Biomed. Mater.* 90 (2019) 73–85. <https://doi.org/10.1016/J.JMBBM.2018.09.042>.

[43] M. Babich, V. Kublanov, Voxel Based Finite Element Method Modelling Framework for Electrical Stimulation Applications Using Open Source Software, in: *Proc.*

- 2019 Ural Symp. Biomed. Eng. Radioelectron. Inf. Technol. USBEREIT 2019, Institute of Electrical and Electronics Engineers Inc., 2019: pp. 127–130. <https://doi.org/10.1109/USBEREIT.2019.8736569>.

[44] Q. Mao, K. Su, Y. Zhou, M. Hossaini-Zadeh, G.S. Lewis, J. Du, Voxel-based micro-finite element analysis of dental implants in a human cadaveric mandible: Tissue modulus assignment and sensitivity analyses, *J. Mech. Behav. Biomed. Mater.* 94 (2019) 229–237. <https://doi.org/10.1016/j.jmbbm.2019.03.008>.

[45] D. Ren, S. Li, H. Wang, W. Hou, Y. Hao, W. Jin, R. Yang, R.D.K. Misra, L.E. Murr, Fatigue behavior of Ti-6Al-4V cellular structures fabricated by additive manufacturing technique, *J. Mater. Sci. Technol.* 35 (2019) 285–294. <https://doi.org/10.1016/j.jmst.2018.09.066>.

[46] M.H. Nasab, D. Gastaldi, N.F. Lecis, M. Vedani, On morphological surface features of the parts printed by selective laser melting (SLM), *Addit. Manuf.* 24 (2018) 373–377. <https://doi.org/10.1016/j.addma.2018.10.011>.

[47] J. Pakkanen, F. Calignano, F. Trevisan, M. Lorusso, E.P. Ambrosio, D. Manfredi, P. Fino, Study of Internal Channel Surface Roughnesses Manufactured by Selective Laser Melting in Aluminum and Titanium Alloys, *Metall. Mater. Trans. A Phys. Metall. Mater. Sci.* 47 (2016) 3837–3844. <https://doi.org/10.1007/s11661-016-3478-7>.

[48] G. Kasperovich, J. Haubrich, J. Gussone, G. Requena, Correlation between porosity and processing parameters in TiAl6V4 produced by selective laser melting, *Mater. Des.* 105 (2016) 160–170. <https://doi.org/10.1016/j.matdes.2016.05.070>.

[49] C.Y. Yap, C.K. Chua, Z.L. Dong, Z.H. Liu, D.Q. Zhang, L.E. Loh, S.L. Sing, Review of selective laser melting: Materials and applications, *Appl. Phys. Rev.* 2 (2015). <https://doi.org/10.1063/1.4935926>.

[50] O. Andreau, P. Peyre, J.D. Penot, I. Koutiri, C. Dupuy, E. Pessard, N. Saintier, Deterministic defect generation in selective laser melting: parametric optimization and control, 2017.

[51] Q. Han, H. Gu, S. Soe, R. Setchi, F. Lacan, J. Hill, Manufacturability of AlSi10Mg overhang structures fabricated by laser powder bed fusion, *Mater. Des.* 160 (2018) 1080–1095. <https://doi.org/10.1016/j.matdes.2018.10.043>.

[52] L. Yang, C. Yan, W. Cao, Z. Liu, B. Song, S. Wen, C. Zhang, Y. Shi, S. Yang, Compression–compression fatigue behaviour of gyroid-type triply periodic minimal surface porous structures fabricated by selective laser melting, *Acta Mater.* 181 (2019) 49–66. <https://doi.org/10.1016/j.actamat.2019.09.042>.

[53] G. Dong, J. Marleau-Finley, Y.F. Zhao, Investigation of electrochemical post-processing procedure for Ti-6Al-4V lattice structure manufactured by direct metal laser sintering (DMLS), *Int. J. Adv. Manuf. Technol.* 104 (2019) 3401–3417. <https://doi.org/10.1007/s00170-019-03996-5>.

[54] S. Tammas-Williams, H. Zhao, F. Léonard, F. Derguti, I. Todd, P.B. Prangnell, XCT analysis of the influence of melt strategies on defect population in Ti-6Al-4V

components manufactured by Selective Electron Beam Melting, *Mater. Charact.* 102 (2015) 47–61. <https://doi.org/10.1016/j.matchar.2015.02.008>.

[55] D.K. Do, P. Li, The effect of laser energy input on the microstructure, physical and mechanical properties of Ti-6Al-4V alloys by selective laser melting, *Virtual Phys. Prototyp.* 11 (2016) 41–47. <https://doi.org/10.1080/17452759.2016.1142215>.

[56] A.M. Khorasani, I. Gibson, U.S. Awan, A. Ghaderi, The effect of SLM process parameters on density, hardness, tensile strength and surface quality of Ti-6Al-4V, *Addit. Manuf.* 25 (2019) 176–186. <https://doi.org/10.1016/j.addma.2018.09.002>.

[57] Q. Wang, Q. Wang, C. Wan, Preparation and evaluation of a biomimetic scaffold with porosity gradients in vitro, *An. Acad. Bras. Cienc.* 84 (2012) 9–16. <https://doi.org/10.1590/S0001-37652012005000003>.

[58] Q. Feng, Q. Tang, Z. Liu, Y. Liu, R. Setchi, An investigation of the mechanical properties of metallic lattice structures fabricated using selective laser melting, *Proc. Inst. Mech. Eng. Part B J. Eng. Manuf.* 232 (2018) 1719–1730. <https://doi.org/10.1177/0954405416668924>.

[59] J. Pegues, M. Roach, R.S. Williamson, N. Shamsaei, Effect of Specimen Surface Area Size on Fatigue Strength of Additively Manufactured Ti6Al4V Parts, *Solid Free. Fabr. Symp.* (2017) 122–133.

[60] S.M. Bowman, X.E. Guo, D.W. Cheng, T.M. Keaveny, L.J. Gibson, W.C. Hayes, T.A. McMahon, Creep Contributes to the Fatigue Behavior of Bovine Trabecular Bone, *J. Biomech. Eng.* 120 (1998) 647–654. https://asmedigitalcollection.asme.org/biomechanical/article-pdf/120/5/647/5535957/647_1.pdf (accessed November 22, 2019).

[61] W.E. Caler, D.R. Carter, Bone creep-fatigue damage accumulation, *J. Biomech.* 22 (1989) 625–635. [https://doi.org/10.1016/0021-9290\(89\)90013-4](https://doi.org/10.1016/0021-9290(89)90013-4).

[62] N.W. Hrabe, P. Heintl, B. Flinn, C. Ko, R.K. Bordia, Compression-compression fatigue of selective electron beam melted cellular titanium (Ti-6Al-4V), *J. Biomed. Mater. Res. Part B Appl. Biomater.* 99 (2011) 313–320. <https://doi.org/10.1002/jbm.b.31901>.

[63] S.J. Li, L.E. Murr, X.Y. Cheng, Z.B. Zhang, Y.L. Hao, R. Yang, F. Medina, R.B. Wicker, Compression fatigue behavior of Ti-6Al-4V mesh arrays fabricated by electron beam melting, *Acta Mater.* 60 (2012) 793–802. <https://doi.org/10.1016/j.actamat.2011.10.051>.

[64] B. Van Hooreweder, Y. Apers, K. Lietaert, J.-P.P. Kruth, Improving the fatigue performance of porous metallic biomaterials produced by Selective Laser Melting, *Acta Biomater.* 47 (2017) 193–202. <https://doi.org/10.1016/j.actbio.2016.10.005>.

[65] K. Lietaert, A. Cutolo, D. Boey, B. Van Hooreweder, Fatigue life of additively manufactured Ti6Al4V scaffolds under tension-tension, tension-compression and compression-compression fatigue load., *Sci. Rep.* 8 (2018) 4957. <https://doi.org/10.1038/s41598-018-23414-2>.

Chapter 7

Summary and Conclusions

7.1 Summary and conclusive remarks

The selective laser melting (SLM) of lattice structure has been studied in the past decade extensively. Most of the studies concentrated on how different designs can affect the mechanical properties of lattice structures for bone implant applications. Very limited research studies the manufacturability of lattice structures especially complicated TPMS designs such as gyroids. This thesis focuses on the integration of gyroid design aspects, SLM manufacturability, and mechanical characterization of Ti6Al4V gyroid lattice structures used for bone implants.

The output parameters of gyroid unit cells that affect the implants' mechanical and biological properties are the pore size, strut size, and the relative density. Since the gyroid surfaces can be represented by implicit equations, therefore a MATLAB® code was developed to control the design of gyroid unit cells. By understanding the relationship between implicit equation parameters and the gyroid's design, a permissible design map was developed to aid the choice of different gyroid designs for bone implants. The code was also used to design novel porosity graded gyroids, the porosity was designed to change across the radius of the samples to mimic bone geometry.

The Process-Structure-Property (PSP) relationship of the gyroid lattice structure printed using SLM was investigated. The gyroid lattice structures were printed at different scanning strategies, and different volumetric energy densities (VED). Hatching strategy with a boarder has been found to give the best dimensional accuracy. The VED levels found to give the least relative density were between 85-103 J/mm³. Process maps were designed to investigate the relationship among laser power, scan speed, and the errors in the relative density of lattice structures. These maps can help predict the errors in the relative density of gyroid lattice structures printed at different SLM process parameters.

Moreover, the manufacturability of uniformly graded gyroids and porosity graded gyroids were studied. It was found that the melt quality of gyroid lattice structures with thicker struts is more uniform than those of thinner ones. However, thinner struts had fewer internal defects than thicker struts. The stepcase effect on the struts' surface acts as stress concentration and facilitates crack initiation, while the internal defects had a greater impact on the crack propagation rate.

Analytical models and finite element analysis (FEA) models were compared to experimental results. The variation of the results gives a better understanding of the effect of manufacturing defects. A better understanding of gyroids manufacturability has been obtained by integrating the permissible design space with the process-structure-property relationship, and the defect analysis of porosity graded gyroids.

7.2 Strength and limitations

The MATLAB® code developed in this work can be used to construct different gyroid designs, that are not available in most of the commercial software tools. The exact pore size, strut size, and relative density can be programed by identifying the exact equation

parameters from constructed lookup tables. The porosity can be graded in both linear and radial manner, to mimic the bone geometry. Moreover, the code can be programmed to design other TPMS designs.

Moreover, the process-structure-property relationship developed in this thesis helps to predict the errors in relative density before printing the lattice structures. This map can be used for predicting and reducing the experimental cost of gyroid structures. In addition, by applying defect analysis in the different gyroid designs, the mechanical properties of these structures can be expected either using analytical or numerical models suggested in this work.

Two numerical models were suggested in this thesis. The first dealt with the whole geometry of the lattice structure while the second dealt with single-unit cells. The first model results were larger than the experimental results, which is attributed to the fact that the least mesh size that can be used for the model to converge was 30 μm . The second model was based on a single unit cell; it was possible to use 7.5 μm mesh size, ensuring that the errors are not related to mesh size. However, material models that included the internal defects could enhance the results. The models were developed to calculate the stiffness of the lattice structure; while the failure criteria were out of the thesis scope.

The compression and fatigue tests were performed on conventional compression machines. Video monitoring was performed to determine the failure time and mode. However, the crack location could not be identified using these methods. Whereas using in situ monitoring for compression and fatigue tests can be used to capture damage initiation and monitor failure. Which would require custom made setups and may result in

interrupting the compression and fatigue tests to obtain more information on the crack initiation spots.

7.3 Future work

The study investigated the manufacturability of Ti6Al4V porosity graded gyroids, investigating the influence of the SLM process defects on the quasi-static and fatigue properties of these structures. In order to overcome the limitations mentioned above, the following studies are suggested for future work:

An in-depth study of crack initiation in the lattice structure can be performed by compressing or fatigue testing the samples while using microCT setup for in situ monitoring. This could help understand the exact location of crack initiation and whether the crack starts from the surface or the internal defects

The FEA model proposed used material properties that are obtained from the literature. More accurate results can be obtained by using a multi-scale microstructure-informed model for the printed Ti6Al4V material. Moreover, by considering the effect of voids on in the FEA model, a more accurate fracture location can be predicted.

The effect of printing the gyroid lattice structures from the functionally graded composition can be studied. The use of a powder mixture of 5 % Hydroxyapatite (HA) and 95 % Ti6Al4V powder has been suggested before in CAD-based lattice structures. However, the functional gradation manner was longitudinal; it is proposed to use SLM machines with two hopper or selective laser dispersing mechanism to print radially graded composition lattice structures. The addition of HA is known to be superior to tissue regeneration compared to titanium alloys on its own.

7.4 Contribution

This thesis gives an overall procedure on identifying the relationship among Ti6Al4V gyroid lattice design, manufacturing, and mechanical characterization. The findings of this study have contributed to understanding the SLM process and correlating between the expected manufacturing defects and the mechanical properties of these structures. Thus a better choice of gyroid designs can be chosen for bone implant applications.

Appendices

Appendix A: Process-Structure property relationship ANOVA tables

A.1 Introduction

The following ANOVA tables represent the mean sources of variation in the data, along with the degrees of freedom (F) in each source. The sequential and adjusted sum of squares (SS) due to the source and the mean sum of squares (MS) are reported. The contribution percentage % given in boldface in the tables, also the low p-value is boldfaced. A low p-value indicates that the factor is significant.

A.2 ANOVA test results for relative errors in $T_b T_h$ and ρ_m

Table A- 1: ANOVA test results for relative errors in $T_b T_h$

Source	DF	Seq SS	Contribution	Adj SS	Adj MS	F-Value	P-Value
Model	9	40960.2	97.19%	40960.2	4551.1	65.32	0.000
Linear	3	35326.5	83.82%	35326.5	11775.5	169.01	0.000
P	1	31892.4	75.67%	31892.4	31892.4	457.75	0.000
V	1	1628.1	3.86%	1628.1	1628.1	23.37	0.000
ρ_d	1	1806.0	4.29%	1806.0	1806.0	25.92	0.000
Square	3	574.9	1.36%	574.9	191.6	2.75	0.075
P*P	1	433.4	1.03%	433.4	433.4	6.22	0.023
V*V	1	45.8	0.11%	45.8	45.8	0.66	0.429
ρ_d* ρ_d	1	95.7	0.23%	95.7	95.7	1.37	0.257
2-Way	3	5058.7	12.00%	5058.7	1686.2	24.20	0.000
P*V	1	49.1	0.12%	49.1	49.1	0.70	0.413
P* ρ_d	1	4833.3	11.47%	4833.3	4833.3	69.37	0.000
V* ρ_d	1	176.4	0.42%	176.4	176.4	2.53	0.130
Error	17	1184.4	2.81%	1184.4	69.7		
Total	26	42144.6	100.00%				

Table A- 2: ANOVA test results for relative errors in ρ_m

Source	DF	Seq SS	Contribution	Adj SS	Adj MS	F-Value	P-Value
Model	9	5777.55	87.57%	5777.55	641.95	13.31	0.000
Linear	3	5615.34	85.11%	5615.34	1871.78	38.80	0.000
P	1	5585.80	84.66%	5585.80	5585.80	115.78	0.000
V	1	5.98	0.09%	5.98	5.98	0.12	0.729
ρ_d	1	23.55	0.36%	23.55	23.55	0.49	0.494
Square	3	80.40	1.22%	80.40	26.80	0.56	0.651
P*P	1	69.94	1.06%	69.94	69.94	1.45	0.245
V*V	1	4.38	0.07%	4.38	4.38	0.09	0.767
ρ_d* ρ_d	1	6.07	0.09%	6.07	6.07	0.13	0.727
2-Way	3	81.82	1.24%	81.82	27.27	0.57	0.645
P*V	1	15.50	0.23%	15.50	15.50	0.32	0.578
P* ρ_d	1	64.29	0.97%	64.29	64.29	1.33	0.264
V* ρ_d	1	2.03	0.03%	2.03	2.03	0.04	0.840
Error	17	820.19	12.43%	820.19	48.25		
Total	26	6597.74	100.00%				

Table A- 3: Regression equations for estimation of relative error in $T_b T_h$ and ρ_m

Regression Equations		R^2	$R^2_{(adj)}$
Relative error in $\bar{\rho}_d$	$= -27.9 + 0.150 P - 0.029 V + 0.68 \bar{\rho}_m$	97.19%	95.70%
Relative error in $T_b T_h$	$= 94.8 + 0.448 P - 0.251 V - 0.51 \bar{\rho}_m$	87.57%	80.99%

A.2 ANOVA test results for relative errors in E_{app} and σ_p

Table A- 4: ANOVA test results for E_{app}

Source	DF	Seq SS	Contribution	Adj SS	Adj MS	F-Value	P-Value
Model	11	50.709	83.43%	50.7086	4.6099	5.49	0.003
Linear	4	40.563	66.74%	36.5508	9.1377	10.89	0.001
<i>P</i>	1	25.180	41.43%	18.7315	18.7315	22.32	0.000
<i>V</i>	1	13.009	21.40%	7.4210	7.4210	8.84	0.012
Design	2	2.374	3.91%	1.6790	0.8395	1.00	0.396
Square	2	2.891	4.76%	2.4166	1.2083	1.44	0.275
<i>P*P</i>	1	1.011	1.66%	0.7848	0.7848	0.94	0.353
<i>V*V</i>	1	1.881	3.09%	0.3913	0.3913	0.47	0.508
2-Way	5	7.254	11.94%	7.2541	1.4508	1.73	0.202
<i>P*P</i>	1	2.687	4.42%	6.0730	6.0730	7.24	0.020
<i>P*Design</i>	2	1.663	2.74%	2.2716	1.1358	1.35	0.295
<i>P*Design</i>	2	2.904	4.78%	2.9043	1.4522	1.73	0.219
Error	12	10.069	16.57%	10.0686	0.8390		
Total	23	60.777	100.00%				

Table A- 5: ANOVA test results for σ_p

Source	DF	Seq SS	Contribution	Adj SS	Adj MS	F-Value	P-Value
Model	11	24755.5	98.40%	24755.5	2250.50	67.15	0.000
Linear	4	24078.2	95.71%	18329.5	4582.37	136.72	0.000
<i>P</i>	1	19373.3	77.01%	9942.3	9942.28	296.65	0.000
<i>V</i>	1	4002.0	15.91%	2731.1	2731.10	81.49	0.000
Design	2	702.9	2.79%	553.0	276.52	8.25	0.006
Square	2	45.9	0.18%	103.1	51.55	1.54	0.254
<i>P*P</i>	1	44.2	0.18%	92.6	92.62	2.76	0.122
<i>V*V</i>	1	1.7	0.01%	60.7	60.73	1.81	0.203
2-Way	5	631.4	2.51%	631.4	126.28	3.77	0.028
<i>P*P</i>	1	306.6	1.22%	31.7	31.67	0.95	0.350
<i>P*Design</i>	2	276.4	1.10%	323.6	161.80	4.83	0.029
<i>P*Design</i>	2	48.3	0.19%	48.3	24.17	0.72	0.506
Error	12	402.2	1.60%	402.2	33.52		
Total	23	25157.6	100.00%				

Table A- 6: Regression equations for E_{app}

Design	Regression equation for σ_p	R^2	$R^2_{(adj)}$
DI	$= 199 + 0.667 P - 0.371 V$	98.40%	96.94%
DO	$= 196 + 0.769 P - 0.378 V$		
NG	$= 229 + 0.667 P - 0.401 V$		

Table A- 7: Regression equations for σ_p

Design	Regression equation for E_{app}	R^2	$R^2_{(adj)}$
DI	$= 10.0 + 0.0379 P - 0.0228 V$	83.43%	68.24%
DO	$= 12.8 + 0.0278 P - 0.0242 V$		
NG	$= 7.3 + 0.0282 P - 0.0184 V$		

Appendix B

B.1 Evaluation of fatigue life of uniform porous structures

The fatigue life for porous structure can be divided into three stages, the crack initiation, crack propagation, and crack coalescence. The ratcheting strain rate is thought to be the main factor determining the fatigue life of porous structures. The ratcheting strain rate $\frac{d\varepsilon}{dN}$ can be described by Equation B 1[1]:

$$\frac{d\varepsilon}{dN} = C(1 - R)^p \frac{0.6}{k+2} \left[\frac{1.7(2k+1)\sigma_{max}}{K \sigma_0} \right]^k \bar{\rho}^{(3k+1)/2} \quad \text{Equation B-1}$$

Where C, p, K, and σ_0 are material parameters in the ratcheting model. R is the load ratio applied in the fatigue testing, and σ_{max} is the maximum fatigue stress, and ρ is the relative density of the porous material. The fatigue life N_f can be determined at a certain stress level by integrating at yield strain of the maximum stress at the monotonic yield strain ε_y (Equation B-2)

$$\frac{1}{N_f} = C \frac{(1-R)^p}{\varepsilon_y} \frac{0.6}{k+2} \left[\frac{1.7(2k+1)\sigma_{max}}{K \sigma_0} \right]^k \bar{\rho}^{(3k+1)/2} \quad \text{Equation B-2}$$

Therefore, for the same material and it can be concluded that ((Equation B-3)

$$N_f = C \frac{\varepsilon_y}{\sigma_{max}^n} \quad \text{Equation B-3}$$

Where C and n are constants related to the material properties of struts and stress ratio and relative density.

For a functionally graded part, the analytical model suggested by Zhao et al. [182] was applied to our functionally graded gyroid G24. We assumed the part consists of two layers for simplicity. The border layer denoted by “*b*” and the center denoted by “*c*.”

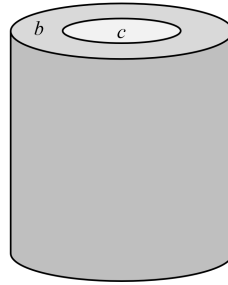


Figure B - 1: Schematic illustration of the radially graded gyroid

The apparent modulus of the border and the center denoted by E_b and E_c , where $E_b > E_c$ as indicated by our experimental results and analytical model in chapter 6. The volume fraction of each layer is denoted by f_c and f_b . The effective modulus of the graded gyroid at the borders can be expressed by Equation B-4:

$$E_{effb} = f_b E_b + f_c E_c \quad \text{Equation B-4}$$

The cyclic deformation strain ε_b , can be expressed by Equation B-5:

$$\varepsilon_b = \frac{\sigma}{E_{effb}} \quad \text{Equation B-5}$$

The instant stress at the *b* and *c* can be expressed by Equation B-6 and Equation B-7 :

$$\sigma_b = E_b \cdot \frac{\sigma}{E_{effb}} = E_b \cdot \frac{\sigma}{f_b E_b + f_c E_c} \quad \text{Equation B-6}$$

$$\sigma_c = E_c \cdot \frac{\sigma}{E_{effb}} = E_c \cdot \frac{\sigma}{f_b E_b + f_c E_c} \quad \text{Equation B-7}$$

Since $\sigma_b > \sigma_c$ crack is expected to initiate at borders first; thus fatigue life can be expressed by σ_b and is calculated as (Equation B-8)

$$N_b = C_b \frac{\varepsilon_{rb}}{\sigma_b^{m_b}} = C_b \frac{\varepsilon_{rb}}{\left(\frac{E_c \cdot \sigma}{f_b E_b + f_c E_c}\right)^{m_b}} = \frac{C_b \cdot \varepsilon_{rb}}{\sigma_b^{m_b}} \cdot \left(f_b + \frac{E_c}{E_b} \cdot f_c\right)^{m_b} \quad \text{Equation B-8}$$

As the crack initiates at the center, the effective modulus can now be expressed as

(Equation B-9)

$$E_{effc} = f_b E'_b + f_c E_c \quad E_c < E'_b < E_b \quad \text{Equation B-9}$$

The cyclic deformation strain is expressed by (Equation B- 10)

$$\varepsilon_c = \frac{\sigma}{f_b E'_b + f_c E_c} \quad \text{Equation B-10}$$

The instant stresses in the mesh are now equal to Equation B-11 and Equation B-12

$$\sigma'_b = E'_b \cdot \frac{\sigma}{f_b E'_b + f_c E_c} \quad \text{Equation B-11}$$

$$\sigma'_c = E'_c \cdot \frac{\sigma}{f_b E'_b + f_c E_c} \quad \text{Equation B-12}$$

At this instant, the stress at the border is lower than σ_b since $\sigma'_b < \sigma_b$, thus the crack propagation stops. However, the stress at the center increases, $\sigma'_c > \sigma_c$. Thus the fatigue life of the graded gyroids can be determined by σ'_c . The cycles to failure N_c is expressed by

$$N_c = C_c \frac{\varepsilon_{rc} - \varepsilon_{rb}}{\sigma_c^{m_c}} = C_c \frac{\varepsilon_{rc} - \varepsilon_{rb}}{\left(\frac{E_c \cdot \sigma}{f_b E'_b + f_c E_c}\right)^{m_c}} = \frac{C_c \cdot (\varepsilon_{rc} - \varepsilon_{rb})}{\sigma_c^{m_c}} \cdot \left(f_c + \frac{E'_b}{E_c} \cdot f_b\right)^{m_c} \quad \text{Equation B-13}$$

$$N = N_b + N_c = \frac{C_b \cdot \varepsilon_{rb}}{\sigma_b^{m_b}} \cdot \left(f_b + \frac{E_c}{E_b} \cdot f_c\right)^{m_b} + \frac{C_c \cdot (\varepsilon_{rc} - \varepsilon_{rb})}{\sigma_c^{m_c}} \cdot \left(f_c + \frac{E'_b}{E_c} \cdot f_b\right)^{m_c} \quad \text{Equation B-14}$$

B.2 Prediction of the fatigue life of G24

The above equations were applied for the three gyroids G2, G4, and G24, and the constants C and n were estimated using Table B-1 and Table B-2

Table B - 1: The stress levels, experimental fatigue lives, and crack initiation strains for G2 and G4

G2	Stress, MPa	33	25	20	16		
	Number of cycles to failure	2437	7245	15650	62960		
	Crack initiation strain %	1.07	0.8422	0.576	0.479		
G4	Stress, MPa	58	43	33	29	20	16
	Number of cycles to failure	822	2923	5987	10750	10750	88500
	Crack initiation strain %	1.48	1.014	0.7925	0.6142	0.6142	0.238

Table B - 2: Calculated material constants for G2 and G4

	G2	G4
C	1.00E+09	3.00E+10
m	3.7	4.28

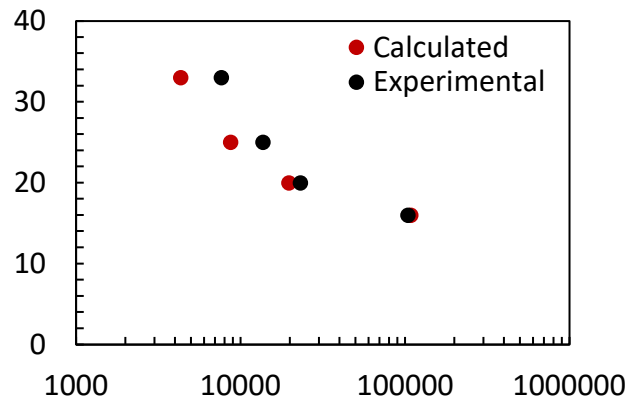


Figure B - 2: The comparison of predicted and experimental fatigue life of G24

The results appeared to be close at low stresses, but the difference increased as the stress level increases. This difference can be attributed to two main factors. The first is that the model assumes the functionally graded lattice to be composed of only two layers, while the graded gyroids were designed to have more layers. The other reason is that the inner layer of the graded gyroid does have the same strut size, but not the same unit cell size. The third reason is that ratcheting strain was found to be high at high stresses, but fatigue strain was higher in high stresses

References

- [1] X.-Y. Zhang, G. Fang, L.-L. Xing, W. Liu, J. Zhou, Effect of porosity variation strategy on the performance of functionally graded Ti-6Al-4V scaffolds for bone tissue engineering, *Mater. Des.* 157 (2018) 523–538.
<https://doi.org/10.1016/J.MATDES.2018.07.064>.